Antenna Elements for Sparse-Regular Aperture Arrays

by

Brandt Klopper

Dissertation presented for the degree of Doctor of Philosophy in Electronic Engineering in the Faculty of Engineering at Stellenbosch University

Supervisor: Prof. D.I.L. de Villiers

April 2019

Declaration

By submitting this dissertation electronically, I declare that the entirety of the work contained therein is my own, original work, that I am the sole author thereof (save to the extent explicitly otherwise stated), that reproduction and publication thereof by Stellenbosch University will not infringe any third party rights and that I have not previously in its entirety or in part submitted it for obtaining any qualification.

Date: ..... April 2019 .....

Abstract

The central theme of this dissertation regards the design and analysis of antenna elements in sparse-regular aperture arrays (AAs) for radio astronomy applications. Throughout this work, a set of modelling techniques are presented to efficiently analyse the impedance and radiation responses of sparse-regular AA elements, which are required to obtain key AA radiometric figures-of-merit. These modelling techniques are applied to a range of narrowband and broadband AA elements, including a novel sparse-regular candidate AA element for the Square Kilometre Array's Mid-Frequency Aperture Array (SKA MFAA).

A thorough study of response models for sparse-regular AA elements is presented, considering several options for the radiometric and full-wave electromagnetic modelling of the antenna elements, as well as global surrogate models for multivariate AA element responses. A design study is presented in which global surrogate modelling techniques are applied for the first time to the design of broadband AA elements, with results that improve upon the per-element receiving sensitivity performance of prior work across a 4.5:1 bandwidth and multiple scan angles.

To improve upon the limited scan and frequency coverage occurring in contemporary AA element design, a global modelling framework is proposed to efficiently estimate sparse-regular AA element impedance responses over a continuous and broad range of frequencies and scan angles. Special attention is paid to the incursion of grating lobes into visible space, which causes rapid response variation and can significantly degrade the elements' active impedance matching. A pre-sampling method is proposed to support the construction of adaptively sampled impedance response models, based on standard array theory and requiring no *a priori* information of the full-wave electromagnetic behaviour of the AA element under analysis. Global models built with the proposed method are shown to obtain significantly more accurate estimates of the global worst-case active reflection coefficient than models built with standard space-filling sampling and pure adaptive sampling techniques.

The global impedance response modelling framework is extended to include the simultaneous modelling of the AA unit cell far-fields, thereby adding radiation responses to the modelling framework and allowing the subsequent determination of figures-of-merit such as receiving sensitivity and intrinsic cross-polarisation ratio. For efficient far-field modelling, two contemporary or-

thogonal basis function decomposition techniques are considered, namely the Spherical Wave Expansion (SWE) and Characteristic Basis Function Pattern (CBFP) method. The two methods are tested for a variety of isolated antenna elements as well as elements in regular AAs, in the first formal comparison of SWE versus CBFP for parametric modelling of antenna far-fields. Following consistent and clear evidence of higher modelling accuracy and computational efficiency, the CBFP method is chosen over SWE to be incorporated into the global modelling framework.

A sparse-regular candidate AA element is proposed for use in SKA MFAA, in the form of a pyramidal sinuous AA element. The element geometry exhibits stable impedance behaviour over frequency and scan angle relative to other possible candidate elements, and is presented in dual-polarised form for MFAA. The element design is well-parametrised to allow further optimisation towards meeting all MFAA requirements.

Finally, as part of realising an optimisation framework for antenna elements in sparse-regular AAs, an expedited performance modelling technique is proposed to rapidly estimate the sensitivity performance of sparse-regular AA elements. Instead of focusing on accurate global response model accuracy, this technique efficiently quantifies the multivariate response performance in a single scalar figure-of-merit incorporating response features such as the sensitivity minimum and overall response smoothness over its operating parameters. Narrowband and broadband examples yield accurate model results with few high-fidelity response samples, with reasonably accurate values provided for the MFAA pyramidal sinuous element within 350 samples.

Uittreksel

Die sentrale tema van hierdie proefskrif behels die ontwerp en analise van antenna elemente in yl, reëlmatige samestellings vir radio sterrekunde toepassings. 'n Stel modelleringstegnieke vir die effektiewe analise van impedansie en stralingspatrone van yl reëlmatige samestellings, wat benodig word vir die berekening van belangrike radio sterrekunde werkverrigtingsmaatstawwe, word deurgaans in die proefskrif aangebied. Hierdie modelleringstegnieke word toegepas op 'n reeks nou- en wyeband antenna elemente, wat onder andere 'n kandidaat element insluit vir 'n yl, reëlmatige implementering van die SKA se middelfrekwensie samestelling (SKA MFAA). 'n Sorgvuldige studie van modelle van die weergawes vir yl reëlmatige samestelling elemente word aangebied, waar verskeie opsies vir die radiometriese en vol-golf elektromagnetiese modellering, sowel as globale surrogaat modellering, oorweeg word. 'n Ontwerpstudie word aangebied waarin globale surrogaat modelleringstegnieke vir die eerste keer toegepas word op die ontwerp van wyeband samestelling elemente, met resultate wat verbeter op die per-element ontvangs sensitiwiteit van vorige werk oor 'n 4.5:1 bandwydte en verskeie stuurhoeke.

Om te verbeter op die beperkte diskrete frekwensie- en stuurhoekdekking wat voorkom in moderne samestelling element ontwerp, word 'n globale surrogaat modellerings raamwerk voorgestel om op 'n effektiewe wyse die impedansie weergawes van yl reëlmatige samestelling elemente oor 'n kontinue en breë gebied van frekwensie en stuurhoeke af te skat. Spesiale aandag word gegee aan die inval van roosterlobbe in die sigbare gebied, wat vinnige verandering in die weergawe tot gevolg het, en wat die aktiewe impedansieaanpassing van die element beduidend kan beïnvloed. 'n Vooraf monstering metode word voorgestel om die konstruksie van aanpassingsvaardig gemonsterde impedansieweergawe modelle te ondersteun. Die metode is gebaseer op standaard antenna samestelling teorie, en benodig geen vooraf kennis van die vol-golf elektromagnetiese gedrag van die spesifieke element nie. Globale modelle wat met die voorgestelde metode gebou was lewer beduidend meer akkurate afskattings van die globale slegste geval aktiewe weerkaatskoëffisiënt as modelle wat met standaard ruimte-vul en suiwer aanpassingsvaardige monsteringstegnieke gebou was.

Die globale impedansieweergawe modelleringsraamwerk word uitgebrei om die gelyktydige modellering van samestelling eenheidselement vervelde te inko-

rporeer. Dit voeg stralingspatroon modellering by die raamwerk, wat die bepaling van werkverrigtingsmaatstawwe soos ontvangs sensitiwiteit en intrinsieke kruispolarisasie verhouding insluit. Vir effektiewe verveld modellering word twee moderne ortogonale basisfunksie tegnieke ondersoek, naamlik sferiese golf uitbreidings (SWE) en die karakteristieke basisfunksie patroon metode (CBFP). Die twee metodes word getoets vir 'n verskeidenheid antenna elemente in isolasie, sowel as in samestellings, in die eerste formele vergelyking van die SWE en CBFP vir parametriese modellering van antenna stralingspatrone. Na konsekwente en duidelike bewyse van beter akkuraatheid, sowel as berekeningseffektiwiteit, word die CBFP bo die SWE gekies om verder in die modelleringsraamwerk geïnkorporeer te word.

'n Yl reëlmatige samestelling antenna element word voorgestel vir gebruik in die SKA MFAA, in die vorm van 'n piramidiese sinus-kronkelende antenna. Die element geometrie toon stabiele impedansie gedrag oor frekwensie en stuurhoek relatief tot ander moontlike kandidaat elemente, en word in die dubbel gepolariseerde vorm vir die MFAA aangebied. Die element ontwerp is goed geparametriseer om verdere optimering toe te laat ten einde al die MFAA behoeftes te bevredig.

Ten slotte, as deel van die realisering van 'n optimeringsraamwerk vir antenna elemente in yl reëlmatige samestellings, word 'n versnelde werkverrigtings modelleringstegniek voorgestel om vinnig die sensitiwiteit van die elemente af te skat. In stede daarvan om te fokus op 'n akkurate globale model, kwantifiseer hierdie tegniek die meervuldige veranderlike skalaar werkverrigting weergawes, soos die minimum van die sensitiwiteit en die algehele gladheid van die weergawe, op 'n effektiewe manier. Nou- en wyeband voorbeelde lewer akkurate model resultate met min simulasie model monsters, met redelik akkurate waardes gelewer vir die MFAA piramidiese sinus-kronkelende element met minder as 350 monsters oor frekwensie en stuurhoek.

Acknowledgements

I would like to express my sincere and deep gratitude towards the following people, all of whom have made this research possible:

- My supervisor, Prof. Dirk de Villiers, for his expertise, guidance and consistent support throughout this project. I am deeply thankful for every suggestion, insight, challenging question and word of encouragement provided over the last three years, and for facilitating my gradual development as a researcher in more ways than could practically be listed here. It is indeed fortunate to have a supervisor of such a high calibre.
- Jan Geralt bij de Vaate for graciously hosting me at ASTRON, as well as for our many insightful discussions regarding aperture arrays and the SKA.
- My mother and father, for their support, love and belief in me. You are the role models who allowed me to aspire to this work.
- My brother, Rijn, for his encouragement, friendship and interest in my research.
- The South African Radio Astronomy Observatory and the National Research Foundation, for their financial support of this project (Grant Number: 75322).
- Raven, Fahmi, Keshav, Anneke, Nicol, Geomarr and everyone I've shared lab space with throughout the past three years, for their advice, insight and friendship.
- Lastly my fiancé and best friend, Jen, for walking this long road with me every step of the way. Your boundless love, kindness, patience and belief in me over the years has been nothing short of incredible — thank you.

Contents

List of Figures

List of Tables

Chapter 1

Introduction

Phased arrays have seen extensive use in radio astronomy, since Martin Ryle's development of the first radio interferometer in 1946 [1]. The principles of phased array technology form the basis of radio interferometry and aperture synthesis, driving the design of long-baseline reflector arrays such as the Very Large Array (VLA) [2] and MeerKAT telescope [3]. The highly sparse layout of these arrays achieve a collecting area many times larger than that of a single antenna, greatly increasing angular resolution and detectability of astronomical sources.

In more recent years, phased array technology has been applied to the development of aperture arrays (AAs) for radio astronomy [4]. The radiating elements of AAs are laid flat on the ground with a direct view of the sky and, unlike mechanically steered reflector dishes, are static structures. The electronic beamforming capabilities of AAs enable them to swiftly scan large sectors of the radio sky, as well as form multiple beams and conduct simultaneous observations on different sectors of the sky [5].

This introductory section provides a brief contextual background of AA systems in the Square Kilometre Array project, considers the current state of AA research and development, and outlines the research opportunities which are thereby presented.

1.1 Aperture Arrays in the SKA

The Square Kilometre Array (SKA) project is an international endeavour to build the world's largest radio telescope [6]. The project is co-hosted by South African and Australian sites with involvement from numerous universities and research institutions worldwide, and aims to vastly improve on the sensitivity and survey speed of any radio telescope currently in existence.

Aperture arrays have been extensively studied and implemented for use in SKA Phase 1's low frequency band (50–350 MHz) as the *Low Frequency Aperture array* (LFAA) system [5], supported by precursor projects such as

the *LOw Frequency Acquisition and Ranging* (LOFAR) system [7] and the *Murchison Widefield Array* (MWA) [8]. As of 2018, a prototype station has been constructed in Australia, named the *Aperture Array Verification System* (AAVS1), as a demonstrator for the final stations to be built for LFAA [9].

In the mid-frequency range (around 0.4–1.5 GHz), aperture arrays are considered a key technology in the realisation of the SKA project's second phase (SKA2-MID) [10]. In the interest of characterising AA systems for high-sensitivity applications such as radio astronomy, a substantial body of research has been developed over the past decade [11]. A major driver of this research effort is the SKA's Mid-Frequency Aperture Array (MFAA) consortium.

1.1.1 SKADS and the MFAA Consortium

The SKA Design Study (SKADS) was conducted from mid-2005 to 2011, and provided a system architecture and feasibility study for SKA2-MID [12]. Results from an SKA precursor project, the Thousand Element Array (THEA) [13], as well as developments from SKA1-LOW AA sytems such as LOFAR, formed a foundation on which SKADS was conducted. A number of concept demonstrators were designed and implemented to verify the concept of dense-regular AAs, including the EMBRACE [14] and 2-PAD systems [15].

The MFAA consortium was formed to further verify the usability of mid-frequency AA technology in SKA Phase 2, as well as investigate various proposed front-end designs [16]. The consortium consists of various research institutes involved in the field of aperture arrays, including the Netherlands Institute for Radio Astronomy (ASTRON), SKA South Africa and a host of universities across the world (including Stellenbosch University). The efforts of the consortium continue the work of SKADS, and are grounded in experience gained from demonstrators such as EMBRACE and THEA.

Since 2016, the *Mid-Frequency Aperture Array Transient and Intensity-Mapping System* (MANTIS) demonstrator project is under consideration for construction in South Africa, which aims to implement an AA system comparable to that of an MFAA station [17]. At the time of writing this dissertation (late 2018), a definite antenna element for MFAA is yet to be selected.

1.1.2 MFAA Design Concepts

At present, most research efforts for mid-frequency AAs are directed at *dense-regular* and *sparse-random* array configurations. Notable mid-frequency AA design concepts proposed for SKA2 are [12]:

- Dense-regular Vivaldi Antena Array [18],
- Octagonal Ring Array (ORA) [19],
- Dense Dipole Array (DDA) [20], and

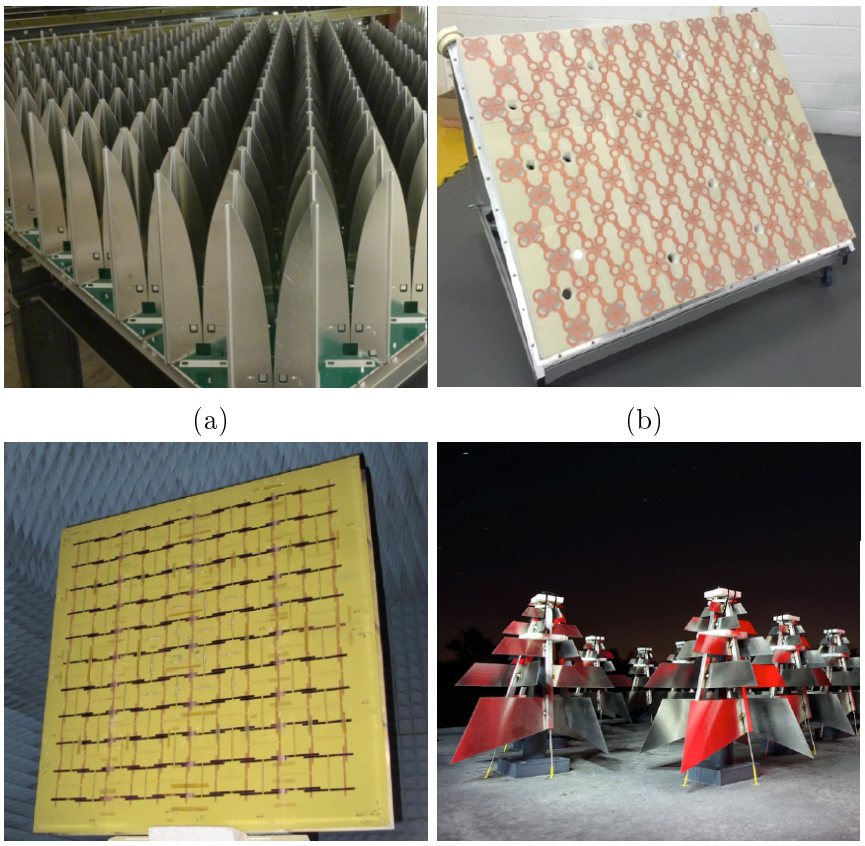

(a) (b)

(c) (d)

Figure 1.1: Various existing SKA2-MID AA design concepts: a) Dense Vivaldi array, b) ORA, c) DDA, d) Sparse-random LPDA array.

- Sparse-random LPDA Array [21].

Prototypes for these existing designs are shown in Figure 1.1. Dense-regular AAs are typically spaced by a half-wavelength at their highest operating frequency to spatially oversample received radiation fields at lower frequencies. This avoids grating lobes in their radiation patterns across the operating bandwidth, and grants them high sensitivity and calibration capability [22]. The close spacing between elements can also cause strong mutual coupling between array antenna elements, worsening system noise performance and incurring unwanted effects such as scan blindness [23]. Sparse-random AAs avoid mutual coupling and mitigate grating lobes through random element placement, but are more difficult to build than regular layouts.

Recently, it has also been proposed that a *sparse-regular* AA can achieve desirable performance at a reduced expense and infrastructural requirement [24]. Sparse-regular aperture arrays possess many attractive qualities, such as lower cost and power consumption due to a lowered element count, lowered inter-element mutual coupling and the ability to use efficient Fast Fourier Transform

(FFT) signal processing techniques [25].

While the sparse-regular AA concept is often disregarded in practice due to a prevalence of grating lobes and lowered sensitivity compared to dense-regular AAs, [24] proposes a number of techniques at system level to mitigate the associated detrimental effects. These techniques, however, do not protect the individual antenna element responses from mutual coupling in the array environment, which can rapidly vary around frequencies and scan angles where grating lobes cross the boundary of visible space [26, 27]. A sparse-regular antenna element for MFAA therefore warrants careful consideration and design to operate satisfactorily in the required scan and frequency range. The opportunities and challenges presented by such a design concept are the focus of this project's research, as part of the endeavour towards designing the SKA's next generation of radio telescopes.

1.2 Contributions

The primary contributions put forth in this dissertation are listed as follows:

- The first application of surrogate modelling to the design of AA antenna elements for response modelling and element geometry optimisation, demonstrating the effectiveness of global surrogate models in design problems of this type.
- A global modelling framework for the scan- and frequency-dependent impedance and radiation responses of antenna elements in sparse-regular AAs, including special considerations for the effects of grating lobes and strategies to obtain accurate and efficient response models in extremely sparse regular array regimes.
- The first quantitative comparison of the Spherical Wave Expansion and Characteristic Basis Function Pattern methods for parametrised multivariate modelling of antenna radiation responses, including comparisons specific to sparse-regular AA elements.
- The proposal of a pyramidal sinuous antenna as a candidate element for a sparse-regular aperture array in MFAA. The proposed element is simple in its construction and exhibits notable stability in its impedance response when placed in the sparse-regular AA environment, warranting further consideration and optimisation of the element to meet the full set of MFAA requirements.
- An expedited optimisation-driven technique to assess the per-element receiving sensitivity performance of antenna elements in sparse-regular AAs, to be used in the attainment of objective function scores as part of a larger AA element optimisation process.

The work of this dissertation has been published (or accepted) in [28–31], demonstrating the novelty and extent of the above contributions.

1.3 Dissertation Layout

This dissertation is composed of six chapters, arranged to gradually develop the global response modelling framework for antenna elements in sparse-regular AAs. Aside from this introductory first chapter, the subsequent chapters are outlined in this section.

Chapter 2 provides a theoretical basis for the analysis of antenna elements in sparse-regular AAs, considering relevant literature from the fields of antenna engineering, radio astronomy, numerical analysis and surrogate modelling to devise a general strategy of efficiently finding the desired array element responses. An initial design study is also provided where the modelling strategy is tested to design a broadband antenna element over a multidimensional parameter space.

Chapter 3 considers global surrogate models for the impedance responses of antenna elements in sparse-regular AAs, focusing on developing accurate and efficient adaptively sampled response models over the array operational parameters (scan angle and frequency). Particular attention is paid towards developing an optimal response model in the sparse-regular array regime, where grating lobes can degrade the impedance response at numerous scan angles that are not usually considered in the design of AA antenna elements. A set of numerical experiments on narrowband and broadband elements are conducted to determine the efficacy of the proposed modelling technique.

Chapter 4 comprises a study of efficient global surrogate models for sparse-regular AA element far-fields, extending the modelling framework of Chapter 3 such that impedance and radiation responses are globally modelled across scan angle and frequency. A study of two contemporary far-field orthogonal basis function decomposition techniques, namely the Spherical Wave Expansion (SWE) and Characteristic Basis Function Pattern (CBFP) methods, are applied to this end and compared for isolated antenna examples as well as sparse-regular AA elements.

Chapter 5 applies the developed response modelling framework to the design problem of broadband antenna elements for MFAA, for which a novel pyramidal sinuous AA element is proposed. A study of the pyramidal sinuous element's scan responses (including pertinent radiometric figures-of-merit) are quantified, after which a global response model is constructed with the techniques of Chapter 3 and 4. In the interest of accelerating the modelling process for use in large iterative antenna optimisation procedures, an optimisation-driven modelling technique is further proposed for the single-objective optimisation of the AA per-element receiving sensitivity. The technique is verified

for narrowband AA elements as well as for the broadband pyramidal sinuous element.

Chapter 6 concludes the work of this dissertation, summarising the results and contributions of the work, and discussing some recommendations for further study in the research topics considered.

Chapter 2

Surrogate Models for Aperture Array Receiving Sensitivity

In the SKA's Mid-Frequency Aperture Array program, there exists an ongoing need to develop optimally designed antenna elements for regularly spaced aperture arrays. Although element designs for most dense-regular AA concepts already exist, several of these elements are still affected by performance issues that could be lessened or removed with a design process that is more advanced than brute-force optimisation or design by parameter sweep. Even for element designs that appear to meet the MFAA performance requirements, many have been validated at a discrete set of scan angles throughout their design, and could yet be improved by a procedure that analyses antenna performance over the whole scanning range at once. In the case of the novel sparse-regular AA concept, an element design has yet to be determined [32].

The purpose of this chapter is to appropriately introduce surrogate modelling techniques to the design of antenna elements in regularly spaced AAs, as well as to provide a foundation for the modelling and design procedures considered throughout future chapters of this dissertation. Section 2.1 reviews contemporary design techniques for antenna elements in aperture arrays and identifies their inherent shortcomings, which are to be addressed by the work of this dissertation. Section 2.2 considers different methods of electromagnetically modelling antenna elements in the regularly spaced AA environment. Section 2.3 discusses noise and mutual coupling in AAs, including the calculation of receiving sensitivity — arguably, the primary figure-of-merit in radiometric receiving systems. Section 2.4 defines surrogate modelling and its techniques as pertinent to this dissertation's design problem, focusing on global surrogate models in the pursuit of a globally optimal AA antenna element design. A selection of these techniques are then applied to an initial design study in Section 2.5, and Section 2.6 concludes.

2.1 Contemporary AA Antenna Element Design

The ultimate design goal of a radio telescope's antenna elements is to satisfy one or more radiometric figures-of-merit across some required frequency and scanning range. In the SKA, one such key figure-of-merit is the *survey speed* [10], defined as

$$\text{SS} = (\text{Sensitivity})^2 \times \text{FoV}, \tag{2.1}$$

where FoV denotes the *processed field-of-view*. For aperture arrays, the processed field-of-view is limited by the digital processing capability of the system backend as well as the half-power beamwidth (HPBW) of the antennas' embedded element patterns [33].

While the processed field-of-view is an important factor of the survey speed, the *receiving sensitivity* (or simply the *sensitivity*) is a requirement more directly related to the antenna design,

$$\text{Sensitivity} = \frac{A_e}{T_{sys}}, \tag{2.2}$$

where A_e is the effective area and T_{sys} is the system noise temperature. The exact definitions of these two terms vary between different types of radiometric receivers as well as the way in which the receiver is electromagnetically modelled, although they are generally functions of the antenna element impedance and radiation responses as well as the input impedance and noise figure of the first-stage low-noise amplifiers (LNAs) connected to the antenna input terminals. These expressions are developed in greater detail in Section 2.3.1.

2.1.1 Design Objectives

A number of regularly spaced AA concepts have been proposed for the MFAA project in recent years, including the Vivaldi antenna array [5], the Dense Dipole Array (DDA) [34] and the Octagonal Ring Array (ORA) [19]. Published documentation for these AA concepts indicate that the design of their antenna elements focused on attaining optimal impedance and radiation responses. For instance, the detailed design procedure of the DDA antenna element aimed to achieve an active reflection coefficient magnitude $|\Gamma_{act}| < -10$ dB across its frequency and scanning range.

This is certainly a valid design technique, given that sensitivity is strongly dependent on the antenna element impedance and radiation responses, especially for the 400-1500 MHz frequency range where receiver noise dominates the system noise temperature [11]. However, it is worth considering a design procedure that directly quantifies the sensitivity and pertinently uses it as the primary design objective, considering that these figures-of-merit will ultimately be used to assess the AA's radiometric performance. An example of

such a design process is given in [35], where the Bowtie Low-frequency Ultra-wideband (BLU) antenna aperture array was designed in parameter sweeps for the 100-450 MHz frequency range.

2.1.2 Frequency and Scan Coverage

Some AA antenna element design procedures have made use of adaptive sampling to calculate antenna responses over a continuous frequency range, with a minimal number of strategically located samples. The design of the DDA, for example, made use of the full-wave electromagnetic (EM) solver FEKO's adaptive frequency solver [36] to obtain accurate frequency responses of the active reflection coefficient, and was able to discern undesired resonances that would likely have been missed by a uniform sampling scheme [34].

In contrast, AA antenna responses are rarely evaluated over the entire scanning range, opting instead for a few cardinal scanning directions [14, 19] or scanning cuts across the antenna E- and H-planes [34]. The former may be a good rough indicator of antenna performance across the whole scan range, but does not account for scanning anomalies related to various forms of scan blindness [26, 27]; the latter is more comprehensive but still gives no information at scan angles between the sampled planes.

In this dissertation, a modelling framework is proposed that applies an adaptive sampling and global modelling scheme to attain a more complete picture of the antenna element response over frequency *and* scan angle. These techniques are further discussed in Section 2.4, and are investigated in Chapters 3–5 for general modelling as well as optimisation-driven models.

2.1.3 Antenna Geometry Optimisation

In the design of AA antenna elements, and for antenna elements in general, it is common to make use of parameter sweeps, brute-force parameter searches and direct local or global iterative optimisation to find a suitable geometric configuration. Pertinent examples include the design of the LOFAR High Band Antenna (HBA) element [37], which was designed with parameter sweeps, and the DDA element, which was designed with a two-stage combination of parameter sweeps and local optimisation [34].

These techniques may well be suitable to find designs that perform sufficiently, but they make little use of the underlying behaviour of the antenna element with respect to its design parameters and can sometimes fail to identify an optimal antenna geometry. Parameter sweeps only cover small regions of a full parameter space, while the computational cost of grid-based parameter searches become unacceptably high as the number of design parameters increase. Direct local and global optimisation may yield better results, but they are often computationally costly and only use response information obtained at evaluated design sites.

An advancement of the above would be to further integrate engineering insight into the modelling and optimisation process, allowing the designer's knowledge of the problem to influence the design beyond the first iteration. The methodology known as *surrogate modelling* is employed to realise such a process in this dissertation, and is expanded upon in Section 2.4. Adaptive sampling combined with global response surface modelling has seen prior success in the design of high-frequency passive microwave circuits [38] and isolated antenna elements [39], but to date has not seen use in the design of wideband, high-sensitivity phased antenna arrays.

2.2 Electromagnetic Modelling of Aperture Arrays

The characterisation of any antenna system, as well as the determination of its radiometric figures-of-merit, requires knowledge of its impedance and radiation responses [23]. During an antenna design process, these responses are typically obtained by simulating the antenna in an electromagnetic solver software package. This section considers the options available to the designer with which a regularly spaced AA can be electromagnetically modelled, and the extents to which each modelling choice would provide accurate and efficient results.

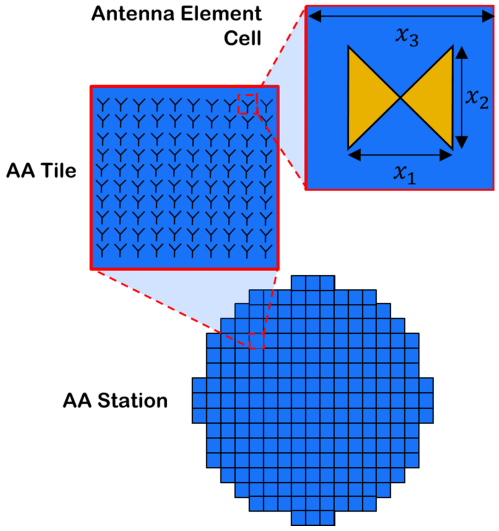

Figure 2.1: Aperture array station, tile and antenna element cell diagram.

At the highest system level, an aperture array is composed of an arrangement of AA stations. Each station is formed of an array of tiles, and in turn each tile is a subarray of antenna elements; it is not uncommon for an AA

station to contain several thousand antenna elements [40]. If the antenna element cells are assumed to be physically identical, then the uniform geometry of the elements is characterised by the design parameter vector $[x_1, x_2 \cdots x_{N_x}]^T$, whose entries are scalar values that parametrise the geometric and material characteristics of the antenna element cell, and where the subscript $\{\cdot\}^T$ denotes the matrix transpose.

Ideally, a direct optimisation of an entire station would grant the designer the most accurate results, as well as complete freedom to simultaneously optimise the elements' responses over a full and continuous range of scan angles. However, the simulation of such a large structure with current full-wave EM solver technology is computationally intractable, especially for techniques such as the standard Method of Moments, whose computational cost increases by $\mathcal{O}(N^3)$ for N mesh elements. Indeed, it is expected that the iterative optimisation of just one AA tile would be computationally exorbitant, as indicated by a single simulation of an existing SKA dense-regular AA tile [34]. It is therefore clear that some compromise must be found for which the AA elements can be designed, based on the modelling of a smaller subsection of the total structure.

Two methods are presented to model the antenna responses of a single element in a large phased array environment. The first is to simulate a physically truncated version of the large array and to accept its behaviour as a reasonable approximation of each individual element in the full array. The second method is to define a regular *unit cell* that contains one or more elements in the array, and to impose periodic boundary conditions that model the infinite array environment. The following two subsections consider both of these methods and weigh up their advantages and drawbacks, as well as the availability of different antenna responses. In general, it is assumed that the antenna structures are passive, and that by reciprocity they may be modelled in transmit or receive mode.

2.2.1 Truncated Array Model

The truncated array model consists of a central antenna element surrounded by a regular finite array of identical elements, with the intent of determining the central element's behaviour in the presence of a truncated approximation of the full array. Each antenna element is modelled with a feed port, which can either be actively excited or passively terminated. In a phased array environment, antenna element responses differ from those obtained with the antenna in isolation; This is attributed to mutual coupling between the antenna and its neighbouring elements as well as the voltage or current excitations applied to the elements, leading to the definition of special impedance and radiation response expressions unique to phased arrays.

Consider a finite planar (in the xy-plane) antenna array comprised of $N_A = (2P+1) \times (2Q+1)$ elements arranged along a grid defined by the parameters

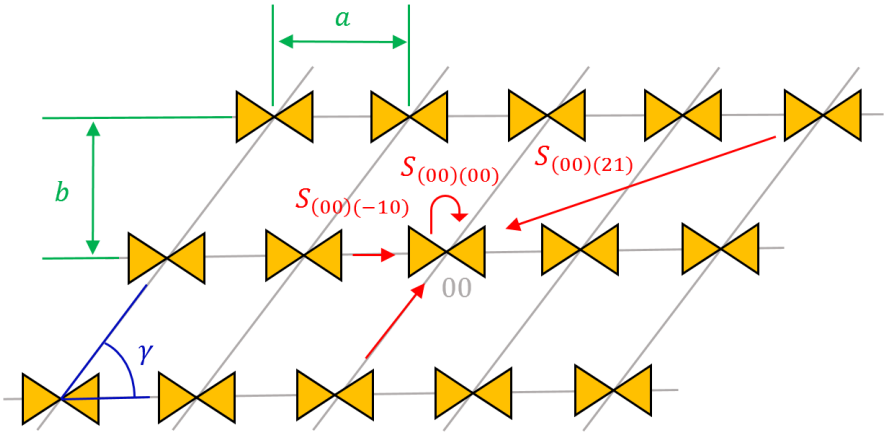

Figure 2.2: Top view of a finite planar antenna array with $P = 2$ and $Q = 1$, showing examples of scattering interactions that contribute towards $\Gamma_{act,(00)}$.

a, b and γ. An example of such an array is depicted in Figure 2.2. P and Q are chosen such that this array is a truncated subset of the full array to be modelled (with the full array assumed too large to efficiently simulate in a full-wave EM solver). Each antenna element is assigned an integer array position index (p, q) with $p \in [-P, P]$ and $q \in [-Q, Q]$, according to the x- and y- coordinates at which it is centred,

$$x_{pq} = pa + \frac{qb}{\tan\gamma}, \quad y_{pq} = qb. \tag{2.3}$$

It is then clear that the antenna element with grid index (00) is the central element at the origin in the xy-plane. The input reflection coefficient at the input port of the central element is labelled its *active reflection coefficient* [27], and is defined as

$$\Gamma_{act,(00)} = \frac{1}{V_{00}^{+}} \sum_{p=-P}^{P} \sum_{q=-Q}^{Q} V_{pq}^{+} S_{(00)(pq)}, \tag{2.4}$$

where V_{pq}^{+} is the forward voltage wave excitation injected at antenna element (pq)'s input terminals and $S_{(00)(pq)}$ is the array scattering interaction observed at the central element due to element (pq). For an aperture array, it is standardly assumed that the array forward excitation voltages are of equal magnitude, and phased to steer the array main beam to a spherical scan angle $\Omega_0 = (\theta_0, \phi_0)$,

$$V_{pq}^{+} = V_0 e^{-jk_{x0}x_{pq} - jk_{y0}y_{pq}}, \tag{2.5}$$

where V_0 is the voltage amplitude constant. The constant inter-element phase shifts along the x- and y-axes, which are functions of Ω_0, are respectively

defined as

$$k_{x0} = k_0 \sin\theta_0 \cos\phi_0 \tag{2.6a}$$
$$k_{y0} = k_0 \sin\theta_0 \sin\phi_0. \tag{2.6b}$$

With such a voltage excitation assumed, the active impedance may be rewritten as a function of scan angle as

$$\Gamma_{act,(00)}(\theta_0, \phi_0) = \sum_{p=-P}^{P} \sum_{q=-Q}^{Q} e^{-jk_0 \sin\theta_0 (x_{pq}\cos\phi_0 + y_{pq}\sin\phi_0)} S_{(00)(pq)}. \tag{2.7}$$

Once the scattering parameters $S_{(00)(pq)}$ are known, then an approximation of $\Gamma_{act,(00)}$ may be determined for any scan angle– the accuracy of the approximation depends on how many scattering interactions are included in the summation [41]. In this work, the only active reflection coefficient considered is that of the central element, such that $\Gamma_{act,(00)}$ and Γ_{act} are interchangeably used to refer to the central element's active reflection coefficient.

For the radiation response of the central element, the *embedded element pattern* is labelled $\overrightarrow{E}_e(\theta, \phi)$ and is defined as the far-field pattern of the array when the central element is excited and all other antennas are passively terminated with a matched load [27]. The embedded element pattern may be transformed into the full array pattern $\overrightarrow{E}_a(\theta, \phi)$ (neglecting edge effects) by multiplying it with the appropriate array factor [41]

$$\overrightarrow{E}_a(\theta, \phi) = \overrightarrow{E}_e(\theta, \phi)\mathrm{AF}(\theta, \phi) = \overrightarrow{E}_e(\theta, \phi) \sum_{p=-P}^{P} \sum_{q=-Q}^{Q} V_{pq}^{+} e^{jk_x x_{pq} + jk_y y_{pq}}, \tag{2.8}$$

where k_x and k_y are defined as

$$k_x = k_0 \sin\theta \cos\phi \tag{2.9a}$$
$$k_y = k_0 \sin\theta \sin\phi. \tag{2.9b}$$

An appropriate choice of P and Q must be carefully considered- the truncated array should be large enough to approximate the desired antenna responses to the designer's desired level of accuracy, yet small enough to avoid unnecessary computational expense. To illustrate the point, a comparison of embedded element pattern H-plane cuts for increasing array size is shown in Figure 2.3. In both cases shown, a planar array of half-wavelength 1 GHz dipole antennas above an infinite ground plane are arranged in a square array regime, and simulated with the CST Microwave Solver (MWS) Frequency Domain solver

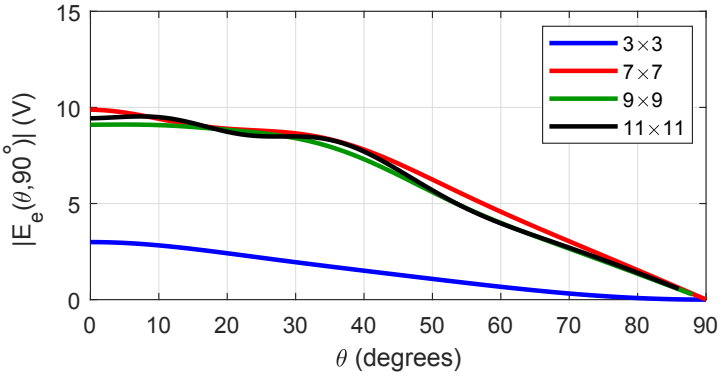

(a)

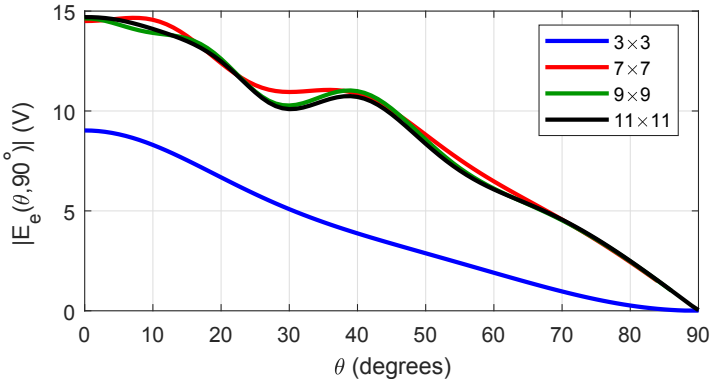

(b)

Figure 2.3: H-plane cuts of the embedded element pattern for the central element of a regular planar array of 1 GHz half-wavelength dipoles– a) $a = b = 0.5\lambda$, $\gamma = 90°$, b) $a = b = 0.75\lambda$, $\gamma = 90°$.

[42]. It can be seen that the pattern cuts only begin to converge when the array is made as large as 11×11 elements, leading to a large simulation domain for the full-wave solution.

The advantages of the truncated array model are that it provides all scan-dependent behaviour of the central element and gives direct access to the embedded element pattern. However, it also bears significant drawbacks– firstly, its computational cost is inherently high given the large array size that must be simulated. Furthermore, it can be difficult to set up the matched terminations for the embedded element pattern as this requires prior knowledge of the antenna elements' input impedance.

2.2.2 Unit Cell Model

The unit cell approach makes use of Floquet theory [41] to model one or more antenna elements in a clearly demarcated cell region bordered by periodic boundaries, as shown in Figure 2.4. The contents of the unit cell are then

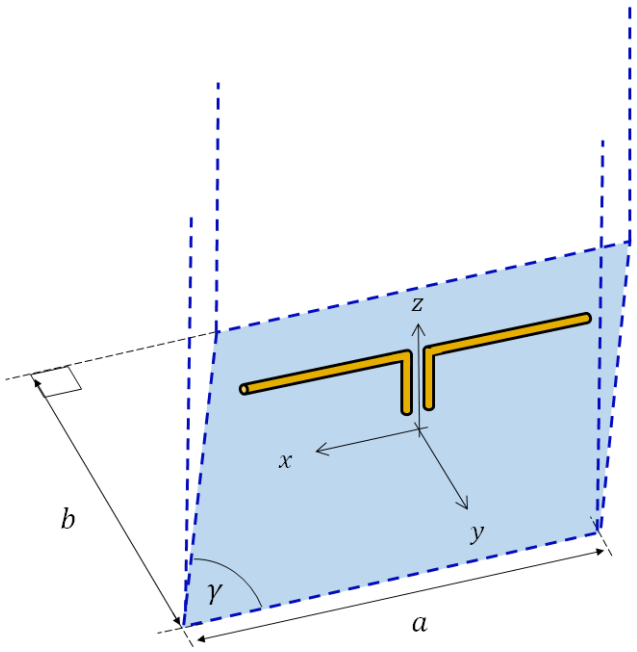

Figure 2.4: Example of a two-dimensional unit cell antenna array model, with a dipole element.

simulated as though they were surrounded by an infinite lattice of identical unit cells, including the mutual coupling interaction between the central cell and all surrounding cells.

In a hypothetical infinite array, the active reflection coefficient of the central element is similar to that of a finite array stimulated with a Floquet excitation,

$$\Gamma_{act,(00)}(\theta_0, \phi_0) = \sum_{p=-\infty}^{\infty} \sum_{q=-\infty}^{\infty} e^{-jk_0 \sin\theta_0 (x_{pq} \cos\phi_0 + y_{pq} \sin\phi_0)} S_{(00)(pq)}. \tag{2.10}$$

For many EM solvers that employ periodic boundaries, the scattering interactions between antennas outside the unit cell cannot be directly determined, and only the active reflection coefficient of the central element is calculated. Additionally, the embedded element pattern is typically not available as the necessary passive terminations cannot be set with periodic boundary conditions. Instead, the *unit cell pattern* labelled $\overrightarrow{E}_{uc-\Omega_0}(\theta, \phi)$ is calculated, which is the far-field pattern radiated by the currents within the central unit cell, including currents induced by mutual coupling from the surrounding cells, when the whole array is stimulated with a Floquet excitation scanned to Ω_0. Unit cell simulations with periodic boundary conditions require a predefined scan angle to be set, and the solutions obtained from each simulation are specific to that particular scan angle.

A single simulation of the unit cell model requires significantly less computation time than the truncated array model, as the physical structure simulated

within the unit cell is much smaller. It is also simpler to set up and obtain results, requiring only one input port to be defined, and does not require prior knowledge of the antenna input impedance to provide a matched load. The distinct disadvantage of the unit cell model lies in its inability to provide continuous scan-dependent response information, requiring N full-wave unit cell simulations to obtain the desired antenna responses at N discrete scan angles. In this sense, a link exists between the infinite array unit cell far-field and the embedded element pattern; For a given scan angle, the unit cell far-field $\overrightarrow{E}_{uc-\theta_0,\phi_0}(\theta,\phi)$ is equal to the embedded element pattern $\overrightarrow{E}_e(\theta,\phi)$ at the spherical pointing angle $(\theta=\theta_0,\phi=\phi_0)$ [43]

$$\overrightarrow{E}_{uc-\Omega_0}(\theta_0,\phi_0) = \overrightarrow{E}_e(\theta_0,\phi_0). \tag{2.11}$$

Thus, the embedded element pattern may be obtained at N discrete pointing angles by simulating the unit cell model for N discrete scan angles.

2.3 Noise in Receiving Aperture Arrays

In a high-sensitivity receiving system, the reduction of system noise is a crucial factor in maximising system sensitivity or signal-to-noise ratio [40]. The primary sources of noise in a receiving array can be written in terms of their *equivalent noise temperatures* as:

- *External noise* (T_{ext}), generated by far astronomical sources and near terrestrial sources (most notably the ground),
- *Loss noise* (T_{loss}), generated by Ohmic and dielectric losses within the antenna elements, and
- *Receiver noise* (T_{rec}), generated by active sources and Ohmic/dielectric losses within the receiver chain.

A weighted sum of these noise temperatures equal the total *system noise temperature* (T_{sys}) [44]. Below 450 MHz, external sky noise dominates T_{sys} [12]. Above 450 MHz, however, sky noise becomes low enough such that T_{rec} becomes a significant portion of T_{sys}; it follows that a minimisation of T_{rec} at the mid-frequencies (around 450–1450 MHz) is necessary to achieve the best sensitivity. Note that if the antenna element is modelled as a lossless structure (PEC conductors and lossless dielectrics), then T_{loss} is zero and does not contribute towards T_{sys}.

Figure 2.5 shows the system model of a general N_A-channel phased array receiving network. The system is divided into sections which contain the N_A-port antenna array network, the $2N_A$-port receiver network and the (N_A+1)-port beamforming network. The $N_A \times N_A$ impedance matrix $\mathbf{Z_A}$ describes the array's impedance parameters looking into the antenna input terminals

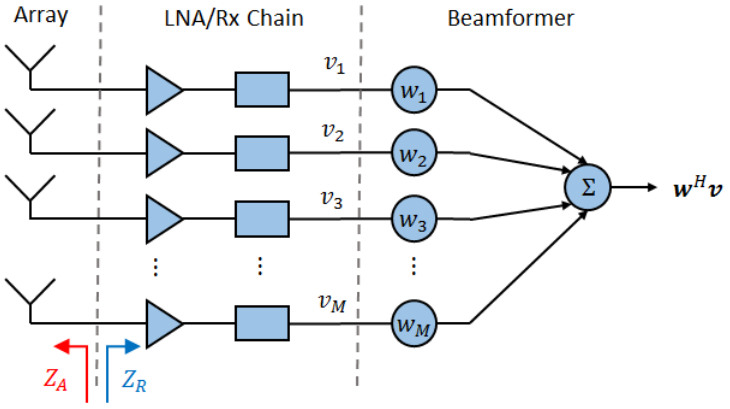

Figure 2.5: Phased array receiver system model

(including the antenna feed), as does $\mathbf{Z_R}$ looking into the left (input) side of the receiver chain. It is assumed that each channel of the receiver chain begins with LNAs having identical input impedances Z_R, and that the receiver chains are uncoupled and identical, giving $\mathbf{Z_R} = Z_R\mathbf{I}$, where $\mathbf{I}$ is the $N_A \times N_A$ identity matrix.

Electromagnetic fields incident on the antenna array generate open-circuit (OC) voltages $\mathbf{v_{oc}} = \begin{bmatrix} v_{oc,1} & v_{oc,2} & \cdots & v_{oc,N_A} \end{bmatrix}^T$, which can be considered as time-harmonic phasors when observed at a single frequency. The receiver voltages appearing at the receiver output/beamformer input junction are related to the OC voltages by

$$\mathbf{v} = Q\mathbf{v_{oc}}, \tag{2.12}$$

where $Q = g\mathbf{Z_R}(\mathbf{Z_R} + \mathbf{Z_A})^{-1}$, given that each receiver chain has identical voltage gain g [45]. Finally, the beamformer modulates each receiver voltage by a corresponding complex weight w_m and sums all N_A channels to produce a 1×1 complex output voltage $v = \mathbf{w}^H\mathbf{v}$, where $\{\cdot\}^H$ denotes the conjugate transpose (Hermitian). This output voltage can be decomposed into a sum of signal and noise voltage, where the signal is received from some astronomical source of interest and the noise is composed of external, loss and receiver noise.

It should be noted that the terms developed in this analysis assume narrowband signal processing techniques and noise equivalent bandwidth B, and are therefore considered to be frequency-dependent terms [46]. Additionally, many of the terms are *beam equivalent* values, since they are dependent on the beamformer weight vector $\mathbf{w} = \begin{bmatrix} w_1 & w_2 & \cdots & w_{N_A} \end{bmatrix}^T$. It is generally assumed that the array is receiving an incident plane wave with an E-field magnitude of E_0 and a power flux density of S_{sig}.

The system diagram of Figure 2.5 is the standard model for a general low-noise phased array system, including aperture arrays and phased array feeds for dish reflectors [44, 47]. However, the model is designed to quantify the performance of the entire array and thus it is not directly compatible with either the truncated array or unit cell antenna models of Section 2.2. In the

following subsections, an exposition of the sensitivity model for the full N_A-channel system is provided as a starting point from which a sensitivity model compatible with the truncated array and unit cell antenna models may be derived.

2.3.1 Noise and Mutual Coupling in Aperture Arrays

In classical antenna theory, a number of subefficiencies are defined that conveniently measure the impact of an antenna's individual features on its total *radiation efficiency* [23]. A number of similar terms are laid out in [44] that redefine existing subefficiencies for phased array receivers and add new subefficiencies that are specific to phased arrays with inter-element mutual coupling.

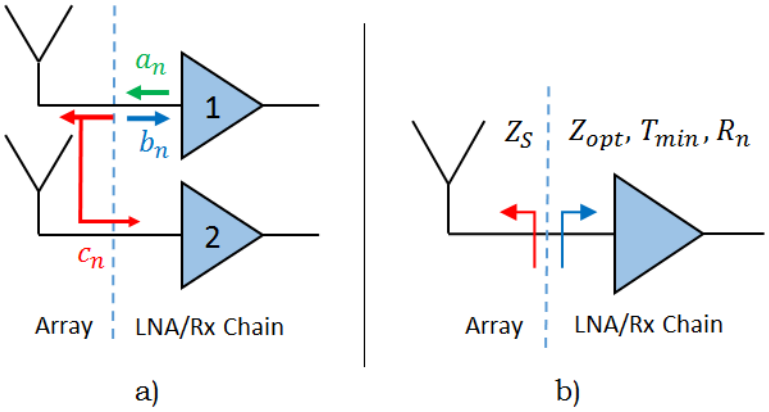

Figure 2.6: Noise considerations in phased array receivers: a) Noise wave coupling between channels due to antenna coupling, b) Noise-matching between LNA and array element.

Figure 2.6a shows a two-channel phased array receiver, at the antenna/LNA junction. A noise wave a_n emanating from channel 1's LNA input port is partially reflected at the antenna input as b_n, and partially transmitted [48]. A portion of the transmitted wave couples to channel 2's antenna elements, which is then partially transmitted into channel 2's LNA. The mutual coupling between the elements is hence responsible for creating correlated noise on the receiver channels.

In order to minimise the impact of antenna-coupled LNA noise on the overall system noise performance, an optimal *noise match* must be obtained. This is similar to traditional noise matching in a single-channel system, where an LNA's input impedance is matched to a source impedance that produces the minimum noise figure in the LNA [49]. The key difference lies in the fact that the input impedance seen at the terminals of an N_A-element phased array is dependent on $\mathbf{Z_A}$, as well as the beamforming vector $\mathbf{w}$ [46], which varies with the beam scan angle. Hence, the value of the optimal "source impedance"

of a phased array receiver is not singularly defined as that of a single-channel system.

2.3.2 Single-Channel Equivalent Antenna Model

For stochastic signals on an N_A-channel network, it is useful to work with the network's *voltage covariance matrix* [45]

$$\mathbf{R_v} = E[\mathbf{v}\mathbf{v}^H] = \lim_{N\to\infty} \frac{1}{N} \sum_{n=1}^{N} \mathbf{v}[n]\mathbf{v}^H[n], \tag{2.13}$$

where $E[\cdot]$ denotes the expected value, and $\mathbf{v}[n]$ represents the n^{th} discrete time sample of $\mathbf{v}$. This fits the general model of radiometric detection, which integrates many time samples of a given signal to mitigate the effects of uncorrelated noise [50]. Correlated noise, conversely, cannot be suppressed by radiometric integration [51], and manifests as nonzero values in the off-diagonal entries of $\mathbf{R_v}$.

Much like $\mathbf{v}$, $\mathbf{R_v}$ can be decomposed into signal and noise components [44] as

$$\mathbf{R_v} = \mathbf{R_{sig}} + \mathbf{R_n} = \mathbf{R_{sig}} + \mathbf{R_{ext}} + \mathbf{R_{loss}} + \mathbf{R_{rec}}. \tag{2.14}$$

These distinct covariance matrices can be used to determine the beam equivalent power at the beamformer output relative to a 1Ω load, dropping the factor of $1/2$ as is common in array signal processing [44]

$$P_{out} = \mathbf{w}^H \mathbf{R_v} \mathbf{w}. \tag{2.15}$$

The output power for each separate covariance matrix can be computed in this way as well, providing scalar power terms that account for all N_A array channels. Following the definitions outlined in [44], these power terms simplify the full N_A-channel system to a single-channel equivalent model (shown in Figure 2.7) with clear definitions for key radiometric figures-of-merit — for instance, the total receiving sensitivity of the array is obtained as [44]

$$\frac{A_e}{T_{sys}} = \frac{k_b B}{S_{sig}} \frac{\mathbf{w}^H \mathbf{R_{sig}} \mathbf{w}}{\mathbf{w}^H \mathbf{R_n} \mathbf{w}} = \frac{\eta_{rad}\eta_{ap} A_p}{\eta_{rad} T_{ext} + (1-\eta_{rad}) T_p + T_{rec}}, \tag{2.16}$$

where k_b is Boltzmann's constant and B is the system equivalent noise bandwidth. These terms are intended to provide a set of IEEE-conforming parameters with which a phased array receiver's performance can easily be quantified. However, the formulation of these terms require knowledge of the full array's embedded element patterns and scattering matrix, which is not computationally feasible for an entire AA station.

Modified versions of the terms developed in [44] may be adopted when considering a single antenna element in a large phased array, as for the element

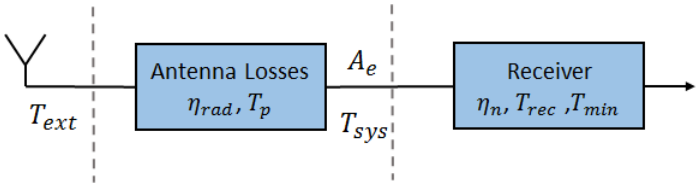

Figure 2.7: Phased array receiver equivalent single-channel model.

models of Section 2.2, to obtain the radiometric figures-of-merit per element. It will be shown that the expressions for this case only require knowledge of the element's active reflection coefficient (or impedance) and either the embedded element pattern or the unit cell far-field.

2.3.3 Noise Temperature Calculations

When the full electromagnetic model of an N_A-element phased array is available, the beamformer weight vector w and voltage correlation matrices are used to calculate the individual noise temperatures that make up T_{sys} [44]. When a single antenna element in a large array is considered, the noise temperatures associated with that element and its receiver chain channel are instead calculated with a modified version of the equations for noise temperatures in a single-channel receiving antenna system.

In a single-channel receiver chain where the antenna terminals are connected directly to a first-stage LNA, the receiver noise temperature is defined as [49]

$$T_{rec} = \left(\left(F_{min} + \frac{4R_N}{Z_0} \frac{|\Gamma_s - \Gamma_{opt}|^2}{(1 - |\Gamma_s|^2)|1 + \Gamma_{opt}|^2} \right) - 1 \right) T_0, \tag{2.17}$$

where Γ_s is the source impedance looking into the antenna input terminals, Z_0 is the system characteristic impedance and T_0 is the standard noise reference temperature at which the two-port noise parameters are characterised (typically taken to be 290 K). The minimum noise figure F_{min}, noise resistance R_N and optimal reflection coefficient Γ_{opt} comprise the noise parameters that describe the LNA's noise behaviour.

When the unit cell or truncated array model is used to analyse a single antenna in a large phased array, the effects of correlated noise from other receiver channels can be modelled by substituting Γ_{act} for Γ_s as [35]

$$T_{rec}(\Omega_0) = \left(\left(F_{min} + \frac{4R_N}{Z_0} \frac{|\Gamma_{act}(\Omega_0) - \Gamma_{opt}|^2}{(1 - |\Gamma_{act}(\Omega_0)|^2)|1 + \Gamma_{opt}|^2} \right) - 1 \right) T_0. \tag{2.18}$$

As can be seen by (2.18), T_{rec} becomes a function of scan angle due to the scan-dependent Γ_{act}.

The external noise temperature T_{ext} can be calculated as [52]

$$T_{ext}(\Omega_0) = \frac{\iint_{4\pi} T_b(\theta,\phi)|F(\theta,\phi|\Omega_0)|^2 \sin\theta d\theta d\phi}{\iint_{4\pi} |F(\theta,\phi|\Omega_0)|^2 \sin\theta d\theta d\phi}, \tag{2.19}$$

where F is the total array field pattern (the magnitude of the co- and cross-polar components) and T_b is the surrounding brightness temperature distribution. A set of models have been developed in [53] to calculate T_b for varying levels of accuracy and computational efficiency.

For a single antenna in a large phased array, F must be set to a scan-dependent radiation response for the element — the unit cell far-field $\overrightarrow{E}_{uc-\Omega_0}$ is directly compatible with this. The embedded element pattern $\overrightarrow{E}_e$, conversely, is not defined as a function of scan angle and may not be appropriate for this external noise temperature model.

Finally, the system noise temperature is given by [44, 54]

$$T_{sys} = \eta_{rad} T_{ext} + (1 - \eta_{rad}) T_0 + T_{rec}, \tag{2.20}$$

where η_{rad} is the array's *radiation efficiency*, standardly defined as the ratio of the radiated power to the total power accepted at the antenna input [23]. This definition is usually applied to an entire phased array system, but when (2.18) and (2.19) are applied it quantifies the system noise temperature of a single receiver channel attached to an antenna element in a regular infinite array environment.

2.3.4 Receiving Sensitivity

In sparse-regular phased array systems, the effective area A_e of the whole array may be approximated as a sum of the effective areas of its individual elements [43]. This is advantageous when modelling an aperture array with either the unit cell or truncated array model, as it allows the designer to calculate the effective area of a single antenna element $A_{e,el}$ and then obtain an estimate of the full N_A-element array's effective area as

$$A_e = N_A \times A_{e,el}. \tag{2.21}$$

For a plane wave incident on an isolated antenna from an angle Ω_0, effective area is defined as the ratio of the power appearing at the antenna terminals to the incident wave's power density [23]. The definition is commonly reformulated as

$$A_e(\Omega_0) = \frac{\lambda^2}{4\pi} G(\Omega_0), \tag{2.22}$$

where λ is the operating wavelength and G is the antenna power gain pattern. For a single antenna in a large phased array, $\overrightarrow{E}_{uc-\Omega_0}$ may be used in place of the isolated antenna's electric far-field pattern to obtain the power gain

pattern per unit cell, when the array is scanned to Ω_0 — this assumes the typical operating conditions of an aperture array, where the main beam is scanned to receive energy from a distant astronomical source. The unit cell gain is denoted in this dissertation as $G_{uc-\Omega_0}$, to differentiate it from the gain of an isolated element G.

The effective area as shown in (2.22) only requires knowledge of the power gain at the incidence angle Ω_0, meaning that only a single far-field value $\overrightarrow{E}_{uc-\Omega_0}(\theta_0, \phi_0)$ is needed per scan/incidence angle. Following (2.11), the embedded element pattern at the incidence angle $\overrightarrow{E}_e(\theta_0, \phi_0)$ may be used instead of $\overrightarrow{E}_{uc-\Omega_0}(\theta_0, \phi_0)$, making the truncated array model compatible with (2.22).

The receiving sensitivity per element, as a function of scan/incidence angle, is now formed by combining (2.20) and (2.22) as

$$\frac{A_e}{T_{sys}}(\Omega_0) = \frac{\frac{\lambda^2}{4\pi} G_{uc-\Omega_0}(\Omega_0)}{\eta_{rad} T_{ext}(\Omega_0) + (1 - \eta_{rad}) T_0 + T_{rec}(\Omega_0)}. \tag{2.23}$$

It can be seen from (2.23) that per-element receiving sensitivity accounts for multiple design aspects in the receiver frontend, including the antenna element radiation pattern, losses in the antenna stucture and the impedance match between the antenna element and the first-stage LNA. It is a particularly useful figure-of-merit from the perspective of antenna element design, as the expression only requires knowledge of the fundamental antenna responses and the noise parameters of the first-stage LNA, and can be scaled to an entire AA, a subarray (such as an AA tile) or a single AA antenna element.

2.4 Global Surrogate Modelling

Surrogate modelling is a paradigm that merges physical insight with numerical analysis techniques to accurately model the responses of computationally costly systems [55]. Surrogate models may be local or global within a parameter space, depending on which type of surrogate model is employed; in this work, global models will be considered that can be applied to antenna responses across frequency and scan angle.

Assume that an antenna response must be known across the entirety of some (generally multivariate) parameter space. This space may include design parameters such as antenna geometry as well as operational parameters such as frequency and scan angle. The antenna response is generally obtained through a full-wave EM solution, which provides the response at one sample point in the parameter space per simulation — these sample-response pairs are referred to as the *fine* (or *high-fidelity*) data. The crux of global surrogate modelling is that a minimal number of responses are simulated at strategic design points that support the construction of an interpolative (or in some cases, approximative) model which provides a continuous approximation of

the response throughout the entire parameter space. The accuracy of this model depends on the choice of interpolation technique, the selection of design points (which may otherwise be considered as interpolation abscissae) and the underlying behaviour of the desired response. For this modelling strategy to be effective, model construction and evaluation should be significantly faster than the evaluation of fine response data.

Surrogate models can be generally classed either as *black-box* or *grey-box* models. A grey-box model is constructed with knowledge of the underlying physical nature of the device/system under scrutiny, and benefits from conventional engineering insight. For instance, when modelling a dipole antenna, it is beneficial to understand that the resonant frequency depends on its overall length, and to incorporate that knowledge into its electrical model. A black-box model, conversely, does not make use of such insight, and is also referred to as a *data-driven* model. Both classes of surrogate model are useful in their own ways; if the designer has a good understanding of the problem at hand, particularly if the problem is well-parametrised to its input variables, then a grey-box model is preferable. When the problem is difficult to parametrise or the designer does not understand the underlying behaviour of the problem in response to a given set of parameters, then a black-box model is likely the better choice.

At this point, a number of modelling terms may need to be specified for the sake of clarity. A model describes a real-world system or device in some approximative way over a continuous parameter space- for this work, models of AA antenna element responses are of interest. A model accepts a vector of input parameters $\mathbf{x} = \begin{bmatrix} x_1 & x_2 & \cdots & x_n \end{bmatrix}^T$, and returns a model response $\hat{y}(\mathbf{x})$ — this approximates the true high-fidelity response $y(\mathbf{x})$, obtained from simulations that are physically accurate but computationally expensive (such as a finely meshed full-wave EM solution). The *parameter space* describes the domain of the inputs over which the model response may be evaluated, and the *response surface* describes the response evaluated across the entire parameter space.

2.4.1 Kriging

Kriging is a class of data-driven techniques that form part of the broader range of Gaussian Processes [56]. Originally developed in 1951 [57], Kriging specifically makes use of the spatial correlations between sample points to create an interpolant of the response surface. The exposition of this subsection follows Kriging for Design and Analysis of Computer Experiments (DACE) [58].

Consider an n-dimensional real parameter space whose values are mapped to a real response surface by an unknown, deterministic function $y(\mathbf{x})$. Given a finite set of sampling points $\mathbf{S} = [\mathbf{x_1}\ \mathbf{x_2}\ ...\ \mathbf{x_m}]^T$ and corresponding responses $\mathbf{Y} = [y_1\ y_2\ ...\ y_m]^T$, both of whose entries are assumed to have zero mean and

a variance of 1, it is desired to find an accurate estimate of any point on the remainder of the unknown response surface. A mean-plus-residual model $\hat{\mathbf{y}}(\mathbf{x})$ is chosen to interpolate the response function

$$\hat{y}(\mathbf{x}) = \mathbf{f}(\mathbf{x})\beta + z(\mathbf{x}), \tag{2.24}$$

where $\mathbf{f}(\mathbf{x})$ is an $1 \times p$ design matrix of regressor functions (typically polynomials of order 0–2), β is a $p \times 1$ vector of regression parameters and $z(\mathbf{x})$ is a 1×1 stochastic residual function, assumed to have zero mean and a covariance of

$$E\left[z(\mathbf{x_i})z(\mathbf{x_j})\right] = \sigma^2 R\left(\theta, \mathbf{x_i}, \mathbf{x_j}\right), \tag{2.25}$$

where σ^2 is the process variance of the residual function, and $R\left(\theta, \mathbf{x_i}, \mathbf{x_j}\right)$ is the correlation function between the i^{th} and j^{th} sample points.

The regression term in (2.24) represents the mean of the Kriging model, for which several strategies are commonly adopted, including *Ordinary Kriging* (regressor functions set to a constant) and *Universal Kriging* (regressor functions set to a polynomial). In this dissertation, Ordinary Kriging is used for its proven flexibility and simplicity [59].

In Kriging, $R\left(\theta, \mathbf{x_i}, \mathbf{x_j}\right)$ is a function of the distance between sample points, generally expressed as

$$R\left(\theta, \mathbf{x_i}, \mathbf{x_j}\right) = \prod_{k=1}^{n} R_k(\theta_k, x_{i,k} - x_{j,k}), \tag{2.26}$$

where $\theta = [\theta_1\ \theta_2 ...\ \theta_n]^T$ is a vector of correlation weights. Various choices for $R_k(\theta_k, x_{i,k} - x_{j,k})$ exist, such as the Gaussian, exponential and Matérn functions [58]. In this dissertation, the Matérn $(\frac{3}{2})$ correlation function is favoured for its ability to model response surfaces of varying levels of smoothness, and is defined as [60]

$$R_k(\theta_k, x_{i,k} - x_{j,k}) = \left(1 + \frac{\sqrt{3}|x_{i,k} - x_{j,k}|}{\theta_k}\right) e^{-\frac{\sqrt{3}|x_{i,k} - x_{j,k}|}{\theta_k}}. \tag{2.27}$$

It is important to note that all of the correlation functions decrease as the distance between sampling points $\mathbf{x_i}$, $\mathbf{x_j}$ increases, and that the larger θ_k is chosen to be, the weaker the correlation becomes along the k^{th} dimension of the parameter space. The choice of correlation functions should depend on what general shape the designer expects the response surface to take.

For the sake of brevity, the derivation of the Kriging interpolant is omitted, and its results are summarised here. For the m sampled points, let the expanded design matrix $\mathbf{F}$ be defined as

$$\mathbf{F} = [\mathbf{f}(\mathbf{x_1})\ \mathbf{f}(\mathbf{x_2}) ...\ \mathbf{f}(\mathbf{x_m})]^T. \tag{2.28}$$

At an arbitrary, unsampled point $\mathbf{x}$, the general solution for the Kriging interpolant $\hat{\mathbf{y}}(\mathbf{x})$ is

$$\hat{\mathbf{y}} = \mathbf{r}^T\mathbf{R}^{-1}\mathbf{Y} - (\mathbf{F}^T\mathbf{R}^{-1}\mathbf{r} - \mathbf{f})^T(\mathbf{F}^T\mathbf{R}^{-1}\mathbf{F})^{-1}\mathbf{F}^T\mathbf{R}^{-1}\mathbf{Y}, \tag{2.29}$$

where $\mathbf{r}$ is an $m \times 1$ vector of correlations between $\mathbf{x}$ and the sampled points

$$\mathbf{r} = [R(\theta, \mathbf{x_1}, \mathbf{x}) \;\; R(\theta, \mathbf{x_2}, \mathbf{x}) \ldots R(\theta, \mathbf{x_m}, \mathbf{x})]^T, \tag{2.30}$$

and $\mathbf{R}$ is an $m \times m$ matrix of correlations between the sampled points, whose entries are given by

$$R_{ij} = R(\theta, \mathbf{x_i}, \mathbf{x_j}), \quad i, j \in [1, 2 \ldots m]. \tag{2.31}$$

The optimal values of the correlation weight vector θ, regression parameter vector β and variance σ^2 are solved as a maximum-likelihood estimation (MLE) problem [58].

Note that Kriging, as described in this exposition, is only capable of modelling real response surfaces. When a complex response is modelled, the response surface must be separated into its real and imaginary parts, each of which is then modelled with a distinct Kriging model.

2.5 Initial Design Study - BLU Antenna Array

In this section, a design study of a regularly spaced AA of BLU (Bowtie Low-frequency Ultrawideband) antenna elements [35] is presented as a first attempt to enhance AA antenna element design via surrogate modelling. The response to be modelled is the receiving sensitivity per unit cell, as a function of the input parameters, frequency and scan angle,

$$y(\mathbf{x}, f, \Omega_0) = \frac{A_e}{T_{sys}}(\mathbf{x}, f, \Omega_0). \tag{2.32}$$

The unit cell model is chosen to simulate the antenna structure — note that the antenna feed is idealised for simplicity, although a practical feed could be included either in the full-wave EM model or as a separate two-port network between the antenna input and the LNA input. The design problem is drawn from an existing study in which an infinite regular array of BLU elements was simulated and the sensitivity per unit cell was observed over linear sweeps of the antenna geometry, over the 100-450 MHz frequency range [35]. This study uses a similar model, but aims to observe the entire parameter space outlined in [35]. It is shown that a complete view of a desired response surface can help to identify good designs that may otherwise be missed by conventional methods.

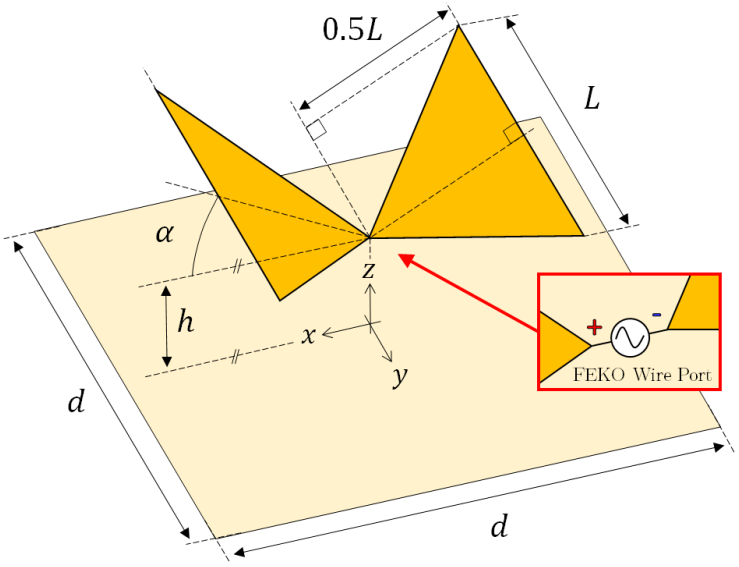

Figure 2.8: Geometry of BLU antenna unit cell with PEC ground plane, with a magnified view of the wire port.

2.5.1 Experimental Design

Figure 2.8 shows the geometry of a square unit cell in the infinite array. The PEC bowtie radiating element is placed h cm above a PEC ground plane, and its length is defined by the parameter L. The bowtie arms are tilted up from the ground at an angle α. The inter-element spacing (and therefore the unit cell length) is defined by the parameter d. Note that the antenna feed structure is idealised to reduce the complexity of the EM model. The LNA topology is also idealised for the same reason, although these structures could be added to the model for a more comprehensive design, albeit at a higher computational expense.

In this study, the following parameters are kept constant: $\alpha = 20°$, $h = 16.6$ cm. The former is the optimal tilt angle found in [35], while the latter was fixed throughout the study. A two-dimensional parameter space is thus considered, defined by the inputs

$$\mathbf{x} = [x_1 \; x_2]^T = \left[\frac{L}{d} \; f_d\right]^T, \tag{2.33}$$

where $d = \frac{c_0}{2f_d}$ (half-wavelength spacing at the frequency f_d), and c_0 is the speed of light in vacuum. The input domain is bounded by $0.2 \leq x_1 \leq 0.9$ and 70 MHz $\leq x_2 \leq$ 290 MHz.

The structure is simulated at 31 equidistant frequencies between 100-450 MHz in FEKO with the Periodic Boundary Conditions Method of Moments (PBC-MoM), and driven by a wire port. Although the system under consideration is a receiving array, reciprocity is assumed and the structure is modelled

in transmit mode (note that the FEKO simulation only encompasses the passive antenna structure, with the LNA modelled separately as described below). The sensitivity per unit cell is calculated with the equations of Section 2.3.1. Note that $\Omega_0 = (0°, \phi_0)$ is collinear with the z-axis of the global coordinate system shown in Figure 2.8, and represents zenith pointing.

The single-channel model used to obtain T_{sys} assumes a system impedance of $Z_0 = 200\,\Omega$, and that the antenna is directly connected to a low-noise amplifier (LNA) with noise parameters $F_{min} = 0.2$ dB, $R_n = 10\,\Omega$ and $Z_{opt} = 200\,\Omega$. The LNA input impedance is also $200\,\Omega$. These parameters are assumed to be constant across the frequency range of interest.

The training set is composed of a regular grid of $N = 400$ points (20×20) to build the Kriging model $\hat{y}(\mathbf{x}, f, \Omega_0)$, at three discrete scan angles: $\Omega_0 = (0°, \phi_0)$, $(45°, 0°)$ and $(45°, 90°)$. At each sampled frequency, a separate model is built across the two-dimensional parameter space. The global surrogate model is implemented in MATLAB [61] with the SUrrogate modelling (SUMO) Toolbox [62].

The form of the Kriging model's regression function is restricted to a constant, whereas the Matérn $(\frac{3}{2})$ function is chosen to determine the model's spatial correlation matrix.

2.5.2 Objective Function

The sensitivity requirement pursued in [35] stipulates a minimum 4000 m^2/K at $\theta_0 = 45°$ across the desired frequency range (note that this is a requirement for the entire aperture array, rather than a single element) [12]. In alignment with this, an objective function is adopted that gives the minimum of the sensitivity over all scan angles and frequencies, and can thus be maximised as a whole to meet the aforementioned requirement

$$U(\mathbf{x}) = \min_{r_0} \left(U_f(\mathbf{x}, \Omega_0) \right), \tag{2.34}$$

where $U_f(\mathbf{x}, \Omega_0)$ is a frequency-dependent objective function. If maximum sensitivity across all simulated scan angles and frequencies is desired, as in (2.34), perhaps the most straightforward expression for U_f is

$$U_{f,1}(\mathbf{x}, \Omega_0) = \min_f (\widehat{y}(\mathbf{x}, f, \Omega_0)). \tag{2.35}$$

While easy to implement, $U_{f,1}$ is flawed in the sense that it minimises indiscriminately at all scan angles, where the sensitivity at scan angles further from zenith will naturally be lower due to the $\cos(\theta_0)$ decrease in effective area. This can cause situations where the objective function favours a design with high minimum sensitivity at scan angles far from zenith, but misses unwanted sharp "spikes" at other scan angles that have otherwise been masked out by the objective function. Furthermore, the system noise temperature at the lower end

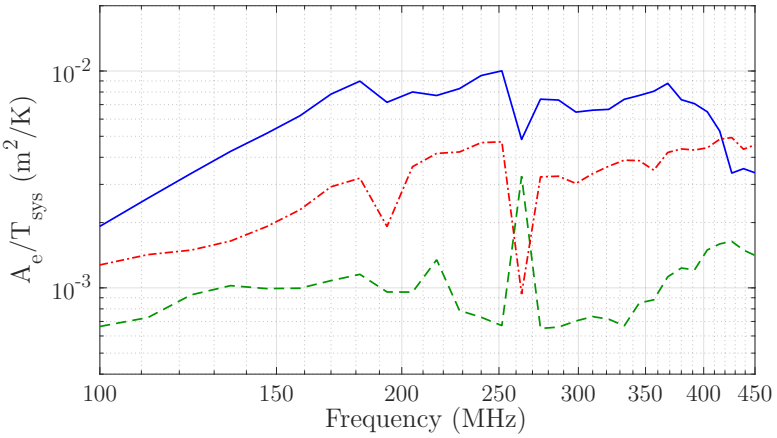

Figure 2.9: Optimal BLU antenna array's per-element sensitivity response found at $\mathbf{x} = [0.487, 96.4 \text{ MHz}]^T$, as found using $U_{f,1}$: — $\Omega_0 = (0°, \phi_0)$, -·- $\Omega_0 = (45°, 0°)$, and - - - $\Omega_0 = (45°, 90°)$.

of the required frequency band will be dominated by unavoidable sky noise, causing the per-element sensitivity to gradually decrease as frequency decreases — in this case, $U_{f,1}$ may also fail to discern responses with sharp downward spikes at higher frequencies. An example of this is given for the BLU antenna simulated at $\mathbf{x} = [0.487, 96.4 \text{ MHz}]^T$ in Figure 2.9, where sensitivity responses with undesirable spikes near 260 MHz is erroneously ranked as an optimal design.

Alternatively, a second objective function is defined as

$$U_{f,2}(\mathbf{x}, \Omega_0) = \min(\hat{y}_l, \hat{y}_h) + \min_f(\min(0, \epsilon_{\hat{y}}(\mathbf{x}, f, \Omega_0)), \tag{2.36}$$

where $\hat{y}_l$ and $\hat{y}_h$ are the values of $\hat{y}(\mathbf{x}, f, \Omega_0)$ evaluated at the lowest and highest frequencies, respectively, while $\epsilon_{\hat{y}}$ is given by

$$\epsilon_{\hat{y}}(\mathbf{x}, f, \Omega_0) = \hat{y}(\mathbf{x}, f, \Omega_0) - \mu(\mathbf{x}, f, \Omega_0), \tag{2.37}$$

where $\mu(\mathbf{x}, f, \Omega_0)$ is a 3^{rd}-order polynomial function that is fitted through $\hat{y}(\mathbf{x}, f, \Omega_0)$, across frequency. While this objective function still maximises the worst-case sensitivity across all considered scan angles and frequencies, it is also designed to reject responses that exhibit sharp spikes that fall below the general trend of the scan-dependent sensitivity responses across frequency.

Figure 2.10 shows the ranking scores generated by $U_{f,1}$ and $U_{f,2}$, for zenith-scanned sensitivity responses obtained at two different points in the parameter space of (2.33). Figure 2.10a shows a clearly undesirable response, exhibiting sharp decreases in sensitivity near 300 MHz and 450 MHz, and is ranked accordingly at a negative score of $U_{f,2} = -2.6 \times 10^{-3}$. A much smoother response is shown in Figure 2.10b, and is assigned a positive score of $U_{f,2} = 1.2 \times 10^{-3}$. Although both responses exhibit similar minimum response values

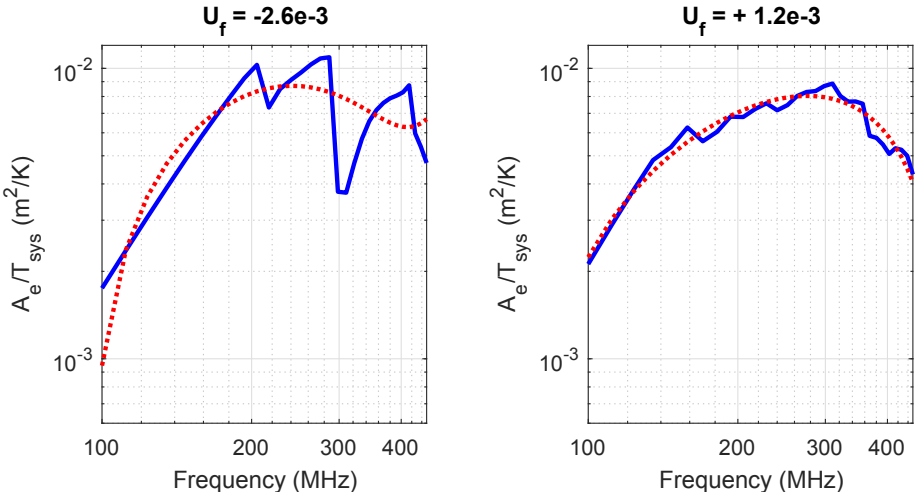

(a) (b)

Figure 2.10: Examples of sensitivity responses $\hat{y}$ (——) plotted against fitted trend functions μ (·····), with the corresponding $U_{f,2}$ objective scores marked above the plots. Both responses are plotted for $\Omega_0 = (0°, \phi_0)$: a) undesired jagged response, b) desired smooth response.

at $f = 100$ MHz, the more jagged response is rejected by the objective function in favour of a smoother response.

The purpose of $U_{f,2}$ is to prevent undesired response features from being hidden by naturally low response values at low frequencies and scan angles far from zenith. The former is only required when the sensitivity naturally and unavoidably decreases with frequency, as is the case for the SKA1 LFAA frequency band. However, it should be clear that $U_{f,2}$ is designed to be applicable to a general sensitivity response with no strict assumptions on the general shape of the sensitivity response as a function of frequency or scan angle, and will still perform its intended function in design situations such as MFAA, where the receiver noise dominates the system noise temperature across the whole frequency band.

2.5.3 Numerical Results

The Kriging model's accuracy and ability to predict unsampled regions of the parameter space is measured with the k-fold cross-validation technique [63]. The root mean squared error (RMSE) is used as an error metric in the cross-validation, given by

$$RMSE(y, \hat{y}) = \sqrt{\frac{1}{N}\sum_{n=1}^{N}(y_n - \hat{y}_n)^2}, \tag{2.38}$$

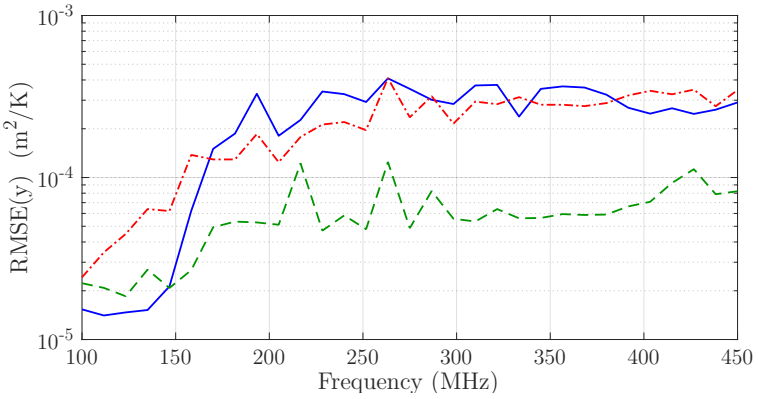

(a)

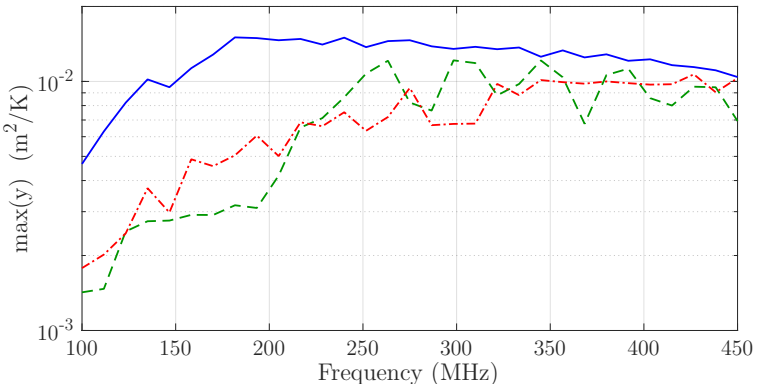

(b)

Figure 2.11: Modelling results: a) 20-fold cross-validation of sensitivity RMSE, b) Maximum sensitivity over all sampled points. — $\Omega_0 = (0°, \phi_0)$, - - - $\Omega_0 = (45°, 0°)$, -·-· $\Omega_0 = (45°, 90°)$.

where y_n and $\hat{y}_n$ denote the high-fidelity and modelled responses evaluated at the n^{th} training point location. This measure is minimised during model construction to attain the most accurate surrogate possible for the given data. RMSE is known to penalise errors more severely in regions where the response is large than where it is close to zero [63]. This is desired for the current design problem, where regions of high sensitivity are sought and must therefore be modelled with a high degree of accuracy.

Figure 2.11a shows the 20-fold cross validation of RMSE versus frequency, for the unit cell's receiving sensitivity at the three scan angles under consideration. RMSE at $\Omega_0 = (45°, 0°)$ is observed to be the lowest overall; this is expected, since the response surface at this scan angle has smaller maxima across the parameter space than at the other scan angles (as is shown in the following subsection). This leads to a slower-varying surface that is generally easier for the chosen Kriging model to capture accurately.

Figure 2.11b shows the maximum sampled sensitivity versus frequency,

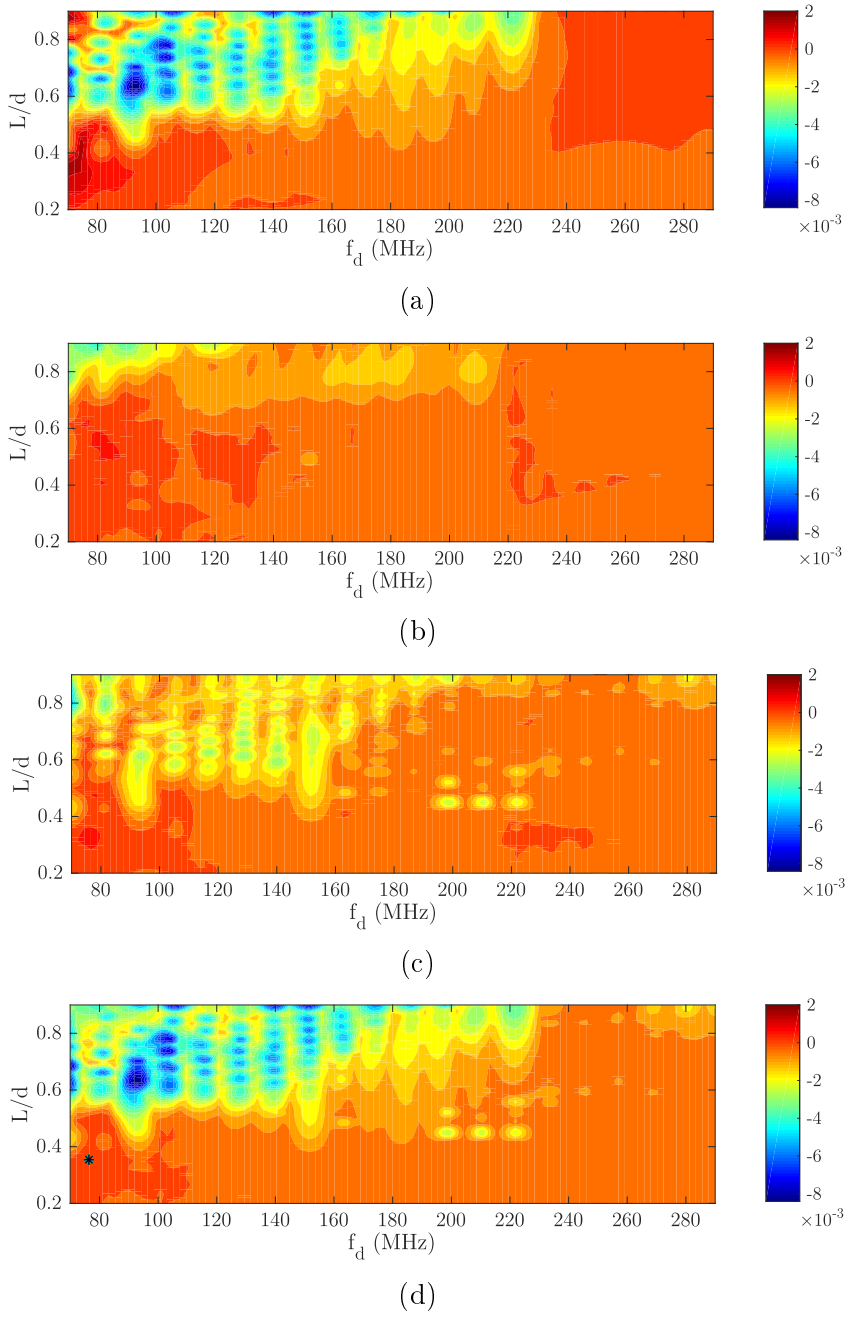

Figure 2.12: Contour plots of $U_{f,2}(\mathbf{x}, r_0)$ at a) $\Omega_0 = (0°, \phi_0)$, b) $\Omega_0 = (45°, 0°)$ and c) $\Omega_0 = (45°, 90°)$, and d) contour plot of $U(\mathbf{x})$.

across the entire parameter space. The RMSE at the three scan angles can be seen to rise with frequency with their respective values of $\max(y)$. This is expected, since the magnitude of the sensitivity in designs of this problem has been generally observed to rise with increasing frequency [35]. Since RMSE is an absolute error metric, it would rise accordingly.

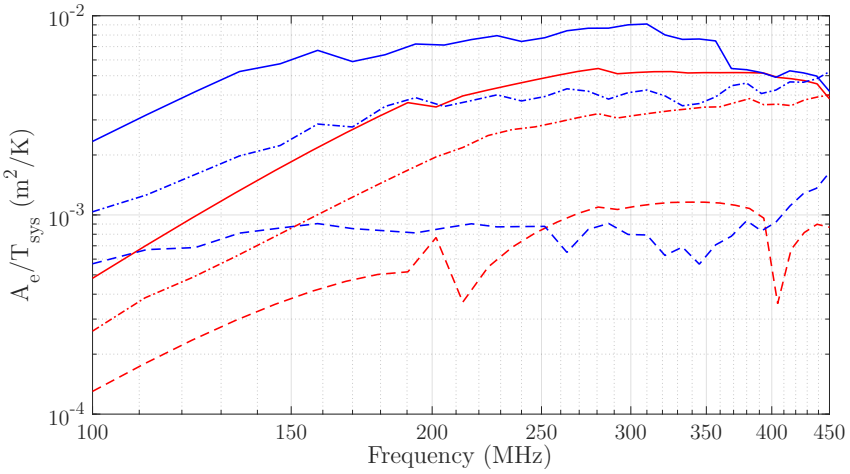

Figure 2.13: Sensitivity vs. frequency of design with parameters $\mathbf{x} = [0.354\,,\, 76.6\text{ MHz}]^T$ (blue traces) and optimal design of the previous study (red traces), simulated with PBC-MoM. For each design: — $\Omega_0 = (0°,\, \phi_0)$, - - - $\Omega_0 = (45°, 0°)$, -·-· $\Omega_0 = (45°, 90°)$.

Figure 2.12a, 2.12b and 2.12c show the contour plots of $U_f(\mathbf{x}, \Omega_0)$ at each scan angle. $U_f(\mathbf{x}, \Omega_0)$ degrades for all three scan angles as $\frac{L}{d}$ increases and f_d decreases. This degradation is caused by several frequency-dependent nonlinear effects, including the onset of grating lobes and the formation of multiple lobes in the embedded element gain pattern when $L > \lambda$ [35]. The distinct nulls in the plots are mostly caused by the latter, and appear at discrete positions in the model because it is built at a discrete set of frequencies. In reality, these nulls move continuously across the parameter space as the frequency f varies, which would create large continuous regions that exhibit degraded scores of $U_f(\mathbf{x}, \Omega_0)$. This is considered to be a modelling artefact caused by the limited and discrete number of frequency samples.

The contour plot of $U(\mathbf{x})$ is shown in Figure 2.12d; this is obviously not a comprehensive worst-case sensitivity prediction across the entire scanning region of interest, but it does present an indication of the AA's performance at the limits of the scanning range in the antenna's E- and H-planes. The global maximum $U(\mathbf{x}) = 4.178 \times 10^{-4}$ m^2/K occurs at $\mathbf{x} = [0.354\,,\, 76.6\text{ MHz}]^T$ (marked in Figure 2.12d with $*$).

Figure 2.13 shows the sensitivity versus frequency of the antenna designed with parameters $\mathbf{x} = [0.354\,,\, 76.6\text{ MHz}]^T$. The sensitivity per unit cell remains above the predicted minimum of 4.178×10^{-4} m^2/K across the entire frequency band and exceeds the minimum sensitivity achieved by the optimal design of [35] ($L = 40$ cm, $f_d = 100$ MHz). The sensitivity response of [35]'s optimal design is also shown for comparison, re-simulated in FEKO with the PBC-MoM solver.

2.5.4 Study Conclusion and Limitations

This first design study has shown that AA antenna element design may be improved with the use global surrogate models in several ways:

1. The full design parameter space is accessed and explored, allowing for a more comprehensive design than a parameter sweep design,

2. A coarse grid of training points is used to obtain a global response surface model across the parameter space, leading to a significant decrease in computational expense when compared to that of a densely sampled brute-force grid search, and

3. An optimal solution is predicted by the response surface model at an unsampled point in the parameter space, simultaneously showing that a search across the full parameter space can yield significantly better design results than parameter sweeps and that the predictive capability of the Kriging model can support accurate design procedures without incurring the cost of brute-force dense grid sampling.

At this point, the limitations of the study should also be considered in terms of the ultimate goals of this dissertation:

1. The per-element sensitivity is only calculated at discrete frequency points and scan angles, giving no indication of the continuous response behaviour over the operational parameter space, and

2. The regular grid is likely a poor choice of training points to support the global response surface model, and could be improved either with better space-filling designs or by picking training points with an adaptive sampling scheme.

The first point of the above list is a limitation that is common to most contemporary AA design procedures, most often due to the high computational expense of simulating antenna responses across a three-dimensional space of operational parameters. It will be shown in Chapters 3 and 4 that the sparse-regular AA environment affects the behaviour of most antenna elements such that their responses must be carefully characterised across the full required scanning space. The second point mentioned above will also be explored in subsequent chapters over the operational parameter space, with the intent to increase the efficiency and accuracy of scan- and frequency-dependent global AA element response models.

2.6 Conclusion

In this chapter, a theoretical basis has been provided for the design of antenna elements in regular aperture arrays, considering the contemporary design methods for AA antenna elements as well as motivating the need to extend the current techniques towards more comprehensive models over frequency, scan angle and antenna design parameters. An exposition of noise modelling in aperture arrays was also given to estimate pertinent radiometric figures-of-merit, beginning with a general multichannel receiver model before focusing on the equivalent per-element system model applicable to unit cell antenna element EM models. Global surrogate modelling was introduced with a brief overview as well as the specifics of Kriging, an interpolation technique which will be invoked regularly throughout the rest of the dissertation. Finally, a one-shot design of the BLU antenna was provided as an initial study of the application of global surrogate modelling to the design problem at hand, showing the potential effectiveness of this approach while simultaneously underlining a set of challenges to be addressed in subsequent chapters of this work.

The main contribution of this chapter was to develop a multivariate global surrogate-based modelling and optimisation framework for broadband antenna elements in regular aperture arrays. The framework was shown to yield improved design results for per-element receiving sensitivity over those of a previous study, and serves as a first step towards developing a modelling framework that provides more comprehensive response information over the full scanning and frequency range of broadband sparse-regular AA elements. The content of Section 2.5 was published in the proceedings of the 2017 International Conference on Electromagnetics in Advanced Applications (ICEAA) [28].

The following chapter will give an analysis of adaptively sampled global surrogate models for the active reflection coefficient of AA antenna elements. A number of deficient aspects of Section 2.5's design study are to be addressed, including the efficiency of training samples and better coverage of antenna responses across operational parameters such as frequency and scan angle.

Chapter 3

Adaptively Sampled Models for Unit Cell Impedance Responses

In Chapter 2, it was shown that the design and optimisation of antenna elements in regularly spaced AAs could be enhanced with the use of global surrogate modelling techniques. A design study of the BLU antenna's geometric parameters was considered in Section 2.5, for which the per-element sensitivity was evaluated at a limited, discrete set of operational parameters (scan angle and frequency). This discrete response set gave no indication of the antenna responses at unsampled frequencies and scan angles, and was identified as a limitation of the study to be considered in further detail.

Additionally, the grid used to sample the design and operational parameter spaces is a commonly used scheme for parameter sweeps but inefficient for global modelling, and is poorly suited to capture the behaviour of a response with a high degree of nonlinearity. More effective sampling techniques include space-filling methods such as the latin hypercube [64] and adaptive sampling algorithms [65].

While Chapter 2 focused on per-element receiving sensitivity, this dissertation aims to develop effective modelling techniques for general sparse-regular AA element responses. This includes the fundamental AA element impedance and radiation responses such as the active reflection coefficient and unit cell far-fields as well as specific radiometric figures-of-merit such as sensitivity and intrinsic cross-polarisation ratio. Given that these figures-of-merit are derived from the fundamental responses, a thorough modelling study of the latter would provide insight to the problem at hand which can then be applied to modelling the desired response term.

This chapter investigates methods to efficiently model the scan- and frequency-dependent impedance behaviour of antenna elements in large sparse-regular AAs. These models are to be constructed over an operational parameter space constituting the AA's required scanning range and frequency bandwidth. It is assumed that the antenna element is simulated in a well-defined infinite array unit cell with periodic boundary conditions (PBC) [66],

and that the array itself is planar, but otherwise the element geometry may be arbitrary as long as a clear input port is defined where the antenna's input impedance is quantified. Considerations specific to sparse-regular AAs are taken into account, such as the presence of grating lobes in the visible region, and a method is proposed to augment the adaptive sampling process with a pre-sampling technique that makes use of standard array factor theory. At this stage, single-polarisation receivers are considered with the active reflection coefficient (Γ_{act}) as the desired response, although the modelling techniques used in this chapter can also be readily applied to modelling the active impedance (Z_{act}) and the mutual and self-impedance terms of a dual-polarised system.

Section 3.1 outlines the modelling scenario posed by the impedance responses of sparse-regular AA elements, and proposes an adaptively sampled global surrogate modelling method to obtain accurate scan response models in the presence of grating lobes in visible space. Section 3.2 applies the proposed technique to a set of numerical experiments, considering both narrowband and broadband elements over wide scanning ranges. Section 3.3 concludes.

3.1 Sparse-Regular AA Scan Modelling

Sparse-regular aperture arrays face a unique AA design problem in the sense that multiple grating lobes (GLs) move in and out of visible space across the array's operating bandwidth and scanning range. This is a challenging scenario not only at the system level, but also at the level of the individual antenna elements, where the mutual coupling interactions can be strongly affected whenever a GL crosses the edge of the visible region [26].

Although the connection between phased array antenna element active reflection coefficient Γ_{act} and GLs is already well-established [26,27,41,67], a simple example is provided here for clarity. Figure 3.1 shows the scan-dependent $|\Gamma_{act}|$ surfaces of a half-wave dipole element placed $\frac{\lambda}{8}$ above a ground plane and at respective array spacings of $d = 0.85\lambda$ and $d = 1.5\lambda$, where λ is the wavelength corresponding to the fixed operating frequency $f = 1$ GHz. A square array layout is considered here for simplicity, yet the observations to be made are also applicable to a general sparse-regular array with parameters (a, b, γ), as defined in the previous chapter. The element is simulated with the Method of Moments in the FEKO software package [36] in a PBC unit cell. A set of loci are also plotted showing the scan angles where GLs cross the visible region boundary, which are numerically determined from the array factor (AF) and GL diagram [41]; Section 3.1.2 discusses the determination of these loci in further detail.

Rapid response variation is seen to occur along many of these loci, intensifying where multiple GL loci intersect. It is interesting to note that for both examples, the maximum $|\Gamma_{act}|$ occurs far from the antenna E- and H-planes,

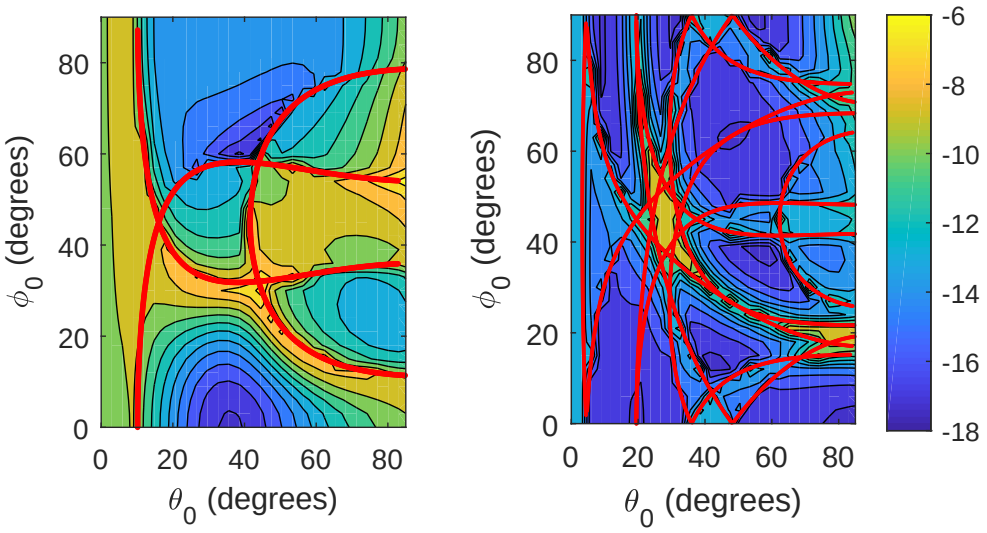

(a) (b)

Figure 3.1: $|\Gamma_{act}|$ response surfaces (in dB) for unit cell models of 1 GHz half-wave dipole antennas with differing inter-element spacings d: a) $d = 0.85\lambda$, and b) $d = 1.5\lambda$. Sudden variations in Γ_{act} are clearly visible around the loci of GL incursion, which are demarcated by red lines (—) in the plots.

and that an accurate picture of the elements' scan performance requires response information from the whole scanning space.

The effect of GLs on the scan- and frequency-dependent $|\Gamma_{act}|$ is also apparent in practical measurements of sparse-regular phased arrays (recall from (2.16) that T_{rec} is strongly dependent on Γ_{act}). Figure 3.2 shows a set of T_{rec} measurements for a version of the APERTIF phased array feed, when configured as an aperture array tile with a direct view of the radio sky [68]. At 1350 MHz, the tile's square array layout has a spacing of $d = 0.495\lambda$, satisfying the spatial Nyquist sampling criterion such that no GLs enter visible space for any scan angle from zenith to the horizon. This is the unperturbed T_{rec} for a tile of well-matched APERTIF elements; the high-temperature band near the horizon for all scanning azimuths is due to the surrounding forestry of the measurement environment, while the conspicuous solid dot is the sun [69].

As the operating frequency increases, the T_{rec} scan response notably changes, with the high-temperature band growing until a curved set of high-temperature arcs become visible. These arcs are visible from 1650 MHz upwards, and can even be seen at 1750 Mhz despite the distortion of the response surface as a result of a "blind scan angle range" (as it is referred to in [68]). For each frequency shown in Figure 3.2, a set of loci are superimposed where, according to the array factor and GL diagram, GLs cross into visible space. These loci coincide with the observed high-temperature arcs, demonstrating the influence of GLs on a practical sparse-regular AA

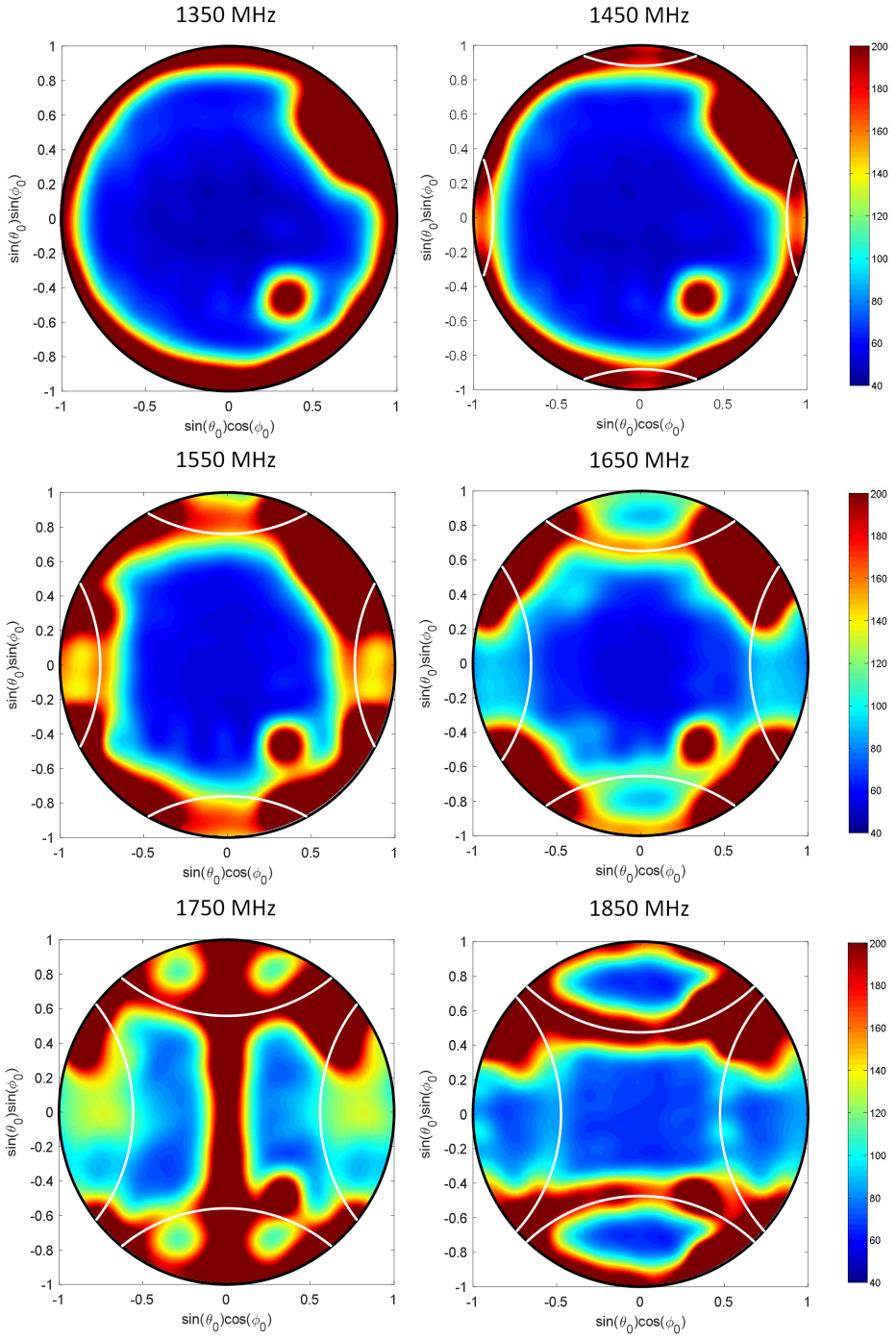

Figure 3.2: Measured T_{rec} of an APERTIF feed, as a function of scan angle for six distinct operating frequencies. White lines delineate the exact locations for which GLs enter visible space. For these measurements, the feed is configured and operated as an aperture array tile; elements are spaced $d = 11$ cm apart.

tile. These results, as well as those of Figure 3.1, show the importance of modelling the whole scanning plane in the design of sparse-regular AAs, as

an antenna element that appears matched in the cardinal E- and H-planes may actually exhibit a poor impedance match at other scan angles due to GL effects.

The remainder of this section considers a set of techniques to efficiently model Γ_{act} as a function of scan angle and frequency for sparse-regular AA elements in an infinite array simulation environment, specifically addressing the modelling of response variations caused by the incursion of GLs into visible space.

3.1.1 Adaptive Sampling

The aim of the global surrogate model is to attain an accurate estimate of the antenna element complex Γ_{act}, with a minimal number of high-fidelity EM simulations. The effectiveness of this strategy strongly depends on two factors: the type of model used, and the distribution of sampling points.

The choice of model type should be carefully chosen to fit the functional variation of the desired response. Rational interpolation, for instance, has already proven effective for the frequency variation of isolated antenna input impedance [70] [71] and the bivariate active reflection coefficient of dense-regular phased array elements [72]. However, the discontinuous behaviour of Γ_{act} in regions of GL incursion is more stably captured by pole-free models such as Kriging.

For a multidimensional parameter space (polar scan θ_0, azimuth scan ϕ_0 and frequency f) with highly nonlinear response behaviour in regions of GL incursion, Ordinary Kriging with the Matérn $(\frac{3}{2})$ correlation function is chosen for its versatility and modelling stability [56]. During model construction, the Kriging hyperparameters are set via maximum likelihood estimation and tuned to minimise the 5-fold cross-validation score of the model.

An adaptive sampling component allows the modelling process a degree of error control, sequentially trading accuracy for computational expense. Instead of building a one-shot sample set such as the grid-based design in Chapter 2, an adaptively sampled design begins with some initial set of samples, constructs a model from this set and then decides where to select the next sample based on some measure derived from the model. After the new sample-response pair is added to the sample set, a new model is constructed and the process is iteratively repeated until some termination criterion is met (such as reaching a maximum number of samples, or the convergence of a model measure below a set threshold value).

In this chapter, the LOLA-Voronoi algorithm [73] is chosen to drive the adaptive sampling process, which is suited to seeking out and iteratively sampling nonlinear response regions. At each model building iteration, a discrete set of candidate points are generated at which the next sample may be placed, and ranking each point by a weighted sum of an *exploitation* score (based on an estimate of the local response linearity/smoothness) and an *exploration*

score (based on the sampling density around the candidate point by means of Voronoi tessellation). The next sampled point is then chosen as the candidate point with the highest ranking score. LOLA-Voronoi thus achieves a balance between comprehensively sampling the whole design space and sampling intensively around nonlinear regions of the response surface, leading to a global surrogate model that is optimally sampled without compromising model accuracy.

Although surrogate modelling has been employed in the past to design isolated antenna elements [74] and linear phased arrays [75], the work presented in this chapter is, to the author's knowledge, the first application of surrogate modelling to the design of planar broadband scanning phased arrays.

3.1.2 Array Factor-based Pre-sampling

Modern adaptive sampling techniques are known for their ability to robustly construct accurate and optimally sampled global surrogate models, regardless of the initial design set that they are provided with. Nonetheless, these adaptive samplers may require many sampling iterations to capture the behaviour of a response surface with multiple localised nonlinear regions if the initial design does not identify them (a possible occurrence for typical space-filling initial designs such as a latin hypercube). If some or all of these nonlinearities can be predetermined as part of an initial design, less exploration burden is placed on the adaptive sampler. Additionally, if response extrema occur in these nonlinear regions, the adaptive sampler is better equipped to identify them if an initial design sample is placed nearby. As has been shown earlier in this section, GL incursion can strongly affect Γ_{act} over frequency and scan angle, creating multiple nonlinearities and sharp response maxima at the incursion points.

The proposed method selects a number of pre-sampling points to form part of the global surrogate model's initial design set, based on the density of GL incursion points at a given frequency f and in a scan plane defined by the elevation and azimuth scan parameters $\theta_0 \in [\theta_{0,min}, \theta_{0,max}]$ and $\phi_0 \in [\phi_{0,min}, \phi_{0,max}]$, respectively. GL incursion points are calculated using a GL diagram and by defining a discrete set of N_{VB} points on the visible region boundary. In the (θ_0, ϕ_0) plane, these points are defined as

$$\theta_0(n_{VB}) = 90°, \quad \phi_0(n_{VB}) = \frac{n_{VB}}{N_{VB}} \times 360°, \quad n_{VB} \in [0, 1, 2 \cdots N_{VB} - 1]. \tag{3.1}$$

For each n_{VB}, a total $N_C(n_{VB})$ crossings are made into (or out of) visible space by all GLs; should $N_C(n_{VB}) > 0$, the corresponding scan angles $(\theta_0(n_C), \phi_0(n_C))$, $n_C \in [1, 2 \cdots N_C]$ are determined where each crossing occurs. Thus, a final total of

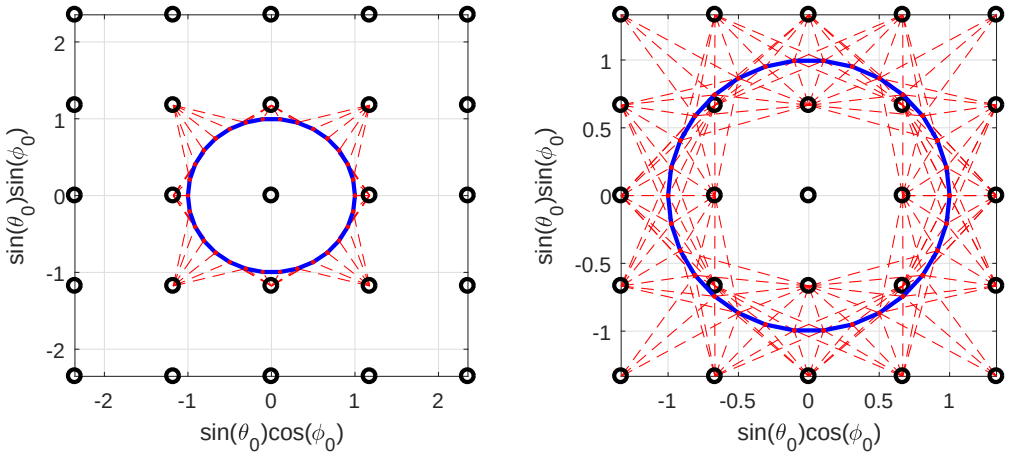

(a) (b)

Figure 3.3: GL diagrams showing GL locations (black rings), visible region boundary (——) and scanning loci from each GL to the N_{VB} boundary points (- - -): a) $d = 0.85\lambda$, and b) $d = 1.5\lambda$. For both plots, $N_{VB} = 31$, $\theta_{0,min} = \phi_{0,min} = 0°$, $\theta_{0,max} = 90°$ and $\phi_{0,max} = 360°$.

$$N_L = \sum_{n_{VB}=1}^{N_{VB}} N_C(n_{VB}) \tag{3.2}$$

points are generated that describe the loci of GL incursion across the scanning space. Two example scenarios are provided in Figure 3.3 to illustrate this numerical procedure. In each case, $N_{VB} = 31$ for visual clarity, although the numerical examples in this dissertation use $N_{VB} = 361$ to describe each locus arc in sufficient detail.

These "raw" incursion points are not uniformly spaced along their loci in the (θ_0, ϕ_0) scanning plane, and are not suited for the intended density-based sampling. To rectify this, the curve of each locus of GL incursion is obtained by cubic spline interpolation of the K calculated incursion points, and uniformly re-sampled along the curves to attain a new set of incursion points. The new points are sampled such that an absolute distance of 0.5° is maintained between adjacent points on the loci. Examples of these two locus sampling schemes are shown in Figure 3.4; it is clear that the points obtained by spline interpolation are more uniformly distributed along the locus arcs than the raw incursion points.

Finally, the parameter space is divided into an $N_\theta \times N_\phi$ grid of uniform cells, which are ranked according to the number of new incursion points that fall within the cell. It should be noted that this ranking operation requires a uniform density of points along each locus arc across the scanning space, necessitating the arc interpolation and uniform re-sampling described earlier.

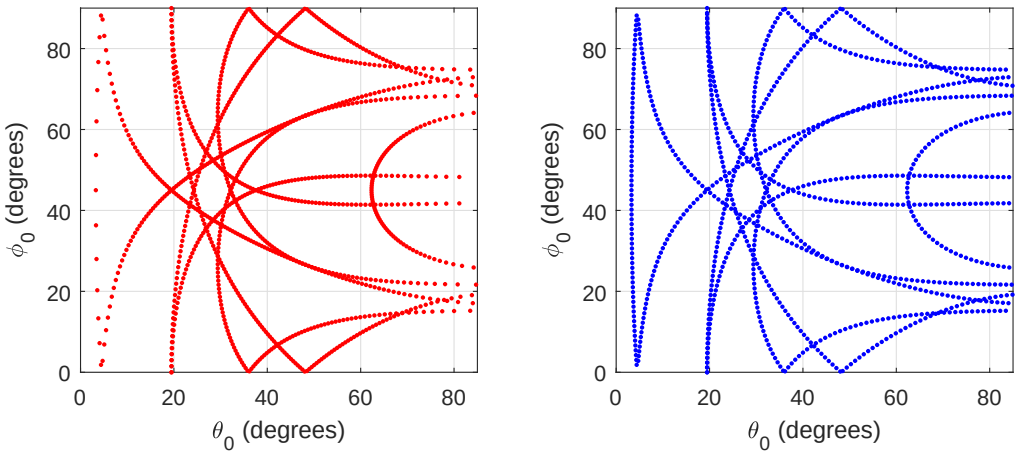

Figure 3.4: Sampling of the GL incursion loci for $d = 1.5\lambda$ and $\theta_0 \in [0°, 85°]$, $\phi_0 \in [0°, 90°]$: a) raw points before re-sampling, and b) uniformly re-sampled cubic spline interpolants of the locus arcs.

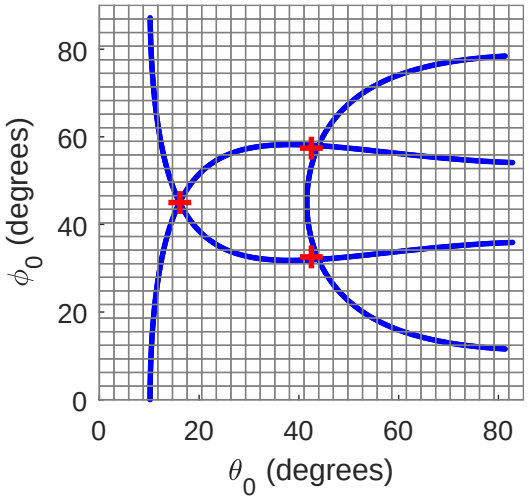

Figure 3.5: Example of the proposed array factor-based pre-sampling method, for an array spacing of $d = 0.85\lambda$. Cell boundaries are demarcated with —, GL loci with —, and + marks the pre-sampled points for $P = 3$.

The final set of pre-sampling points are then found at the centres of the P highest-ranked cells. Figure 3.5 shows an example where $\theta_{0,min} = \phi_{0,min} = 0°$, $\theta_{0,max} = 85°$, $\phi_{0,max} = 90°$ and $P = 3$. Here, and in the numerical examples of Section 3.2, N_θ and N_ϕ are chosen for a cell width and height of 3°. It can clearly be seen that the method selects cells around the intersections of GL loci.

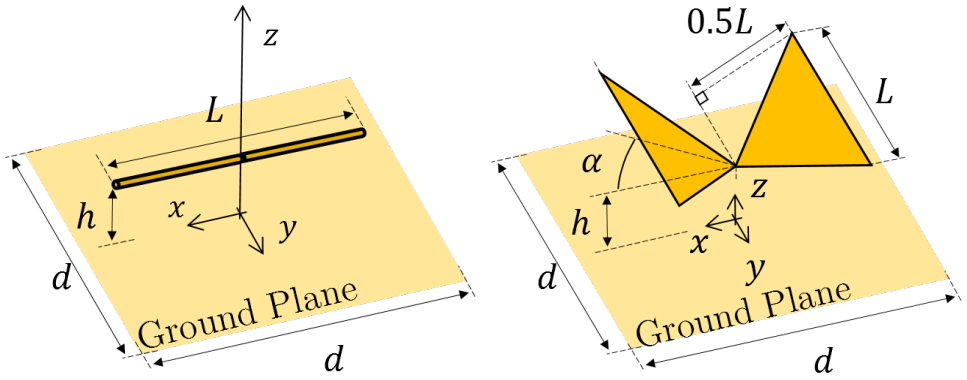

(a) (b)

Figure 3.6: Antenna unit cell geometries used in Section 3.2: a) dipole element, and b) BLU element.

The parameters N_θ, N_ϕ and P may be chosen freely, although some heuristics are suggested here. The density cell parameters N_θ and N_ϕ should be set to allow a sufficient number of points to fall in cells where many GL loci intersect — The number of pre-sampled points P should scale with the response complexity, which can be seen by Figure 3.1 to depend on the number of GLs that enter the observed scanning space.

Assuming that the loci only intersect once with one another, P may be set to the maximum number of these intersections as

$$P = \frac{V(V+1)}{2}, \tag{3.3}$$

where V is the number of GLs entering the visible region. However, many of the intersections do not significantly perturb Γ_{act}, as can be seen in Figure 3.1, making it potentially wasteful to sample each one. A more conservative scheme is to set $P \propto V$, which does not expand as rapidly as (3.3) with increasing array sparsity.

3.2 Numerical Experiments

In this section, three pertinent examples are investigated with the proposed modelling method. The first two involve 1 GHz half-wave dipole antenna elements at two different sparse array spacings, which serve to test the method at a fixed frequency, to model Γ_{act} as a function of scan angle only. The third example models Γ_{act} of the Bowtie Low-Frequency Ultrawideband (BLU) antenna [35], as a function of frequency and scan angle. For the two dipole experiments, the model construction is repeated 10 times with distinct LHS designs and averaged to smooth the random nature of the LHS distributions. For the BLU element, model construction is performed only once due to high

computational expense, yet the results shown behave similarly to those of the dipole experiments.

Three different sampling schemes are to be compared: one-shot latin hypercube sampling (LHS) [64], LOLA-Voronoi with an N_i-point LHS initial design, and LOLA-Voronoi with an N_i-point initial design built from a combination of LHS and points generated by the AF-based pre-sampling method detailed in Section 3.1.2. These schemes are henceforth referred to as S_1, S_2 and S_3 respectively.

Two error metrics are used to quantify the model performance. The first is the mean absolute difference error in Γ_{act}, given by

$$\epsilon_{mean}(N_s) = \frac{1}{N_v} \sum_{n=1}^{N_v} \left| \Gamma_{act}(\mathbf{x}_n) - \widetilde{\Gamma}_{act,N_s}(\mathbf{x}_n) \right|, \tag{3.4}$$

where Γ_{act} denotes the responses of a validation set of length N_v, $\widetilde{\Gamma}_{act,N_s}$ denotes responses of a model built with N_s samples, and $\mathbf{x}_n = (\theta_{0,n}, \phi_{0,n}, f_n)$ is the parametric combination for the n^{th} response in the validation set.

During optimisation tasks where an antenna design must meet a fixed performance requirement, it is often useful to know the worst response performance across its operating parameters. Here the "worst performance" is considered to be the largest validation $|\Gamma_{act}|$, assuming that the element should be well-matched over its frequency and scan range, and the second error metric is accordingly defined as

$$\epsilon_{worst}(N_s) = \left| \max_{\mathbf{x}_n} |\Gamma_{act}(\mathbf{x}_n)| - \max_{\mathbf{x}_n} |\widetilde{\Gamma}_{act,N_s}(\mathbf{x}_n)| \right|. \tag{3.5}$$

The pre-sampling technique and adaptively sampled global surrogate model are implemented in MATLAB [61] with the SUrrogate modelling (SUMO) Toolbox [62]. The dipole antennas are simulated in in FEKO's PBC-MoM solver, while the BLU antenna is simulated in CST's Frequency Domain Solver with PBC [42].

The space-filling initial designs of S_1 and S_2 are designed to sample the parameter space as broadly as possible for a given N_i; this is contrasted by S_3, which uses a portion of its samples to bias the model towards known regions of GL-related response variation. This biasing is expected to result in an initially low ϵ_{worst} score, or to inform the adaptive sampler of the landscape near the response maxima so that it may place additional samples to model them accurately and thereby lower ϵ_{worst}. The expected effect is that S_3 will tend to sacrifice some of its initial general modelling accuracy to improve the model accuracy at response maxima, after which the general accuracy is improved by subsequent samples selected by LOLA-Voronoi.

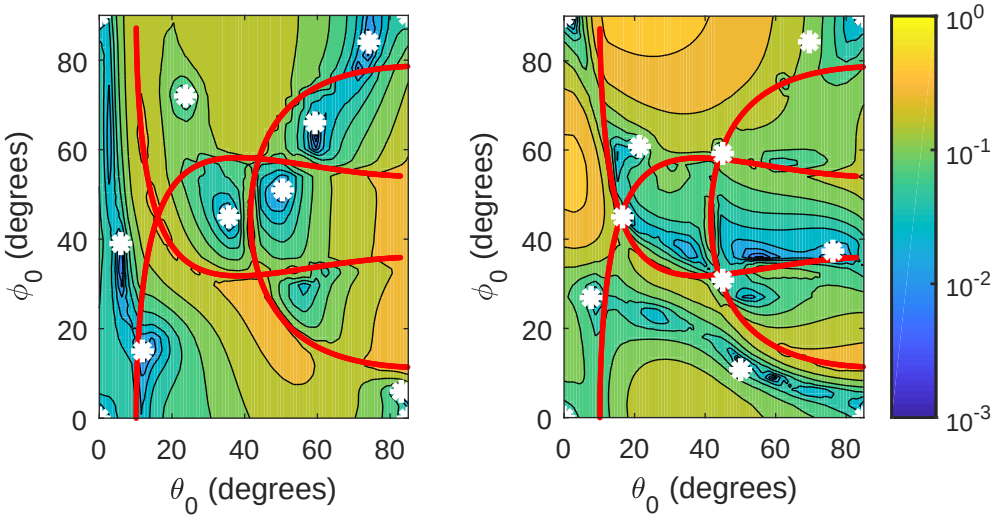

(a) (b)

Figure 3.7: Γ_{act} absolute difference surfaces for the first dipole experiment ($d = 0.85\lambda$): a) S_2, and b) S_3. Red lines (—) show the loci of GL incursion, while white stars mark sample locations.

3.2.1 Narrowband Scan Modelling — Dipole Element

The two dipole experiments are chosen to represent a broadband sparse-regular phased array operating at its lower and upper frequency ranges, respectively. Figure 3.6a shows a PBC unit cell model of the dipole antenna above a conducting ground plane — the array spacing for the first experiment is set as $d = 0.85\lambda$, and $d = 1.5\lambda$ for the second. The remaining geometric parameters are set as $L = 0.475\lambda$ and $h = \frac{\lambda}{8}$. The response to be modelled is Γ_{act} observed at the 50 Ω wire port in the dipole center, across the parameter space defined by $x_1 = \theta_0 \in [0°, 85°]$, $x_2 = \phi_0 \in [0°, 90°]$. For S_2 and S_3, the number of initial design points is set as $N_i = N_{GL} \times 4$, while $P = N_{GL}$ for S_3, leading to initial designs of 12 points for the first dipole and 60 points for the second. The initial design size is chosen to scale with the response surface complexity, which is seen in Figure 3.1 to increase as more GLs enter the scanning space. For $d = 0.85\lambda$, 3 GLs cross into visible space, while 15 GLs are present for $d = 1.5\lambda$.

Figure 3.7 shows the absolute difference error for the second dipole experiment ($d = 1.5\lambda$), for S_2 and S_3 with $N_s = N_i$. The space-filling placement of S_2's initial design yields a slightly lower overall model error, yet the response maxima are poorly modelled. In comparison, the biasing effect of S_3 towards the response maxima is clearly visible, as the modelling error is lowest around the intersection points of the GL incursion loci.

Figure 3.8 shows the averaged ϵ_{mean} scores of the two dipole experiments. The biasing effect of S_3's initial design is evident, beginning with the highest

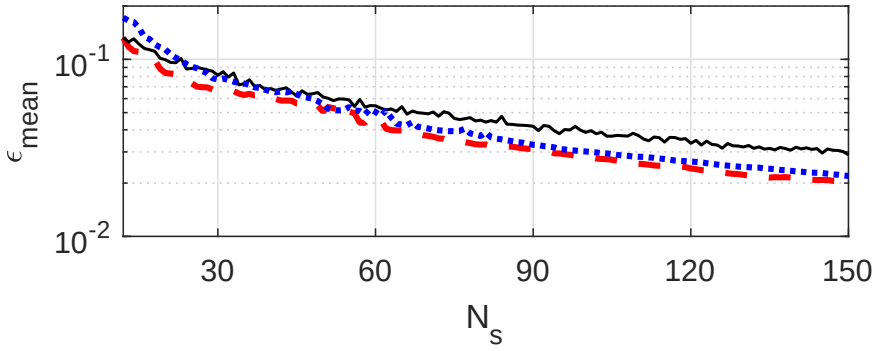

(a)

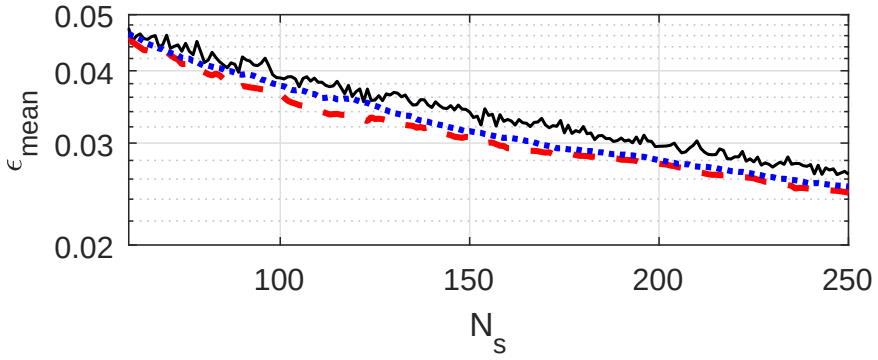

(b)

Figure 3.8: ϵ_{mean} scores for a) dipole ($d = 0.85\lambda$), and b) dipole ($d = 1.5\lambda$) For both plots: — S_1, - - - S_2, ····· S_3.

ϵ_{mean} scores. However, it can also be seen that as N_s increases, S_3 improves until its ϵ_{mean} scores rival that of either S_1 or S_2.

Figure 3.9 shows the averaged ϵ_{worst} scores of the dipole experiments. For the first dipole, the validation maximum $|\Gamma_{act}| = 0.519$ (-5.69 dB) at $(\theta_0, \phi_0) = (44.7°, 30.1°)$. For the second dipole, the maximum $|\Gamma_{act}| = 0.401$ (-7.94 dB) at $(\theta_0, \phi_0) = (41.5°, 31°)$. In both cases, the ϵ_{worst} score for S_3 shows relatively steady and rapid convergence to values several orders of magnitude lower than S_1 and S_2. This is attributed to the pre-sampling algorithm placing samples near the points of GL incursion, where the validation maxima occur.

The results shown in Figures 3.8 and 3.9 thus indicate that, while S_3 may sacrifice some *initial* general modelling accuracy in exchange for lower ϵ_{worst}, the use of an appropriate adaptive sampling scheme can recover most or all of this accuracy in relation to the other sampling schemes.

3.2.2 Broadband Scan Modelling — BLU Element

The third experiment considers the broadband BLU antenna element over the parameter space defined by $x_1 = \theta_0 \in [0°, 60°]$, $x_2 = \phi_0 \in [0°, 90°]$, $x_3 = f \in$

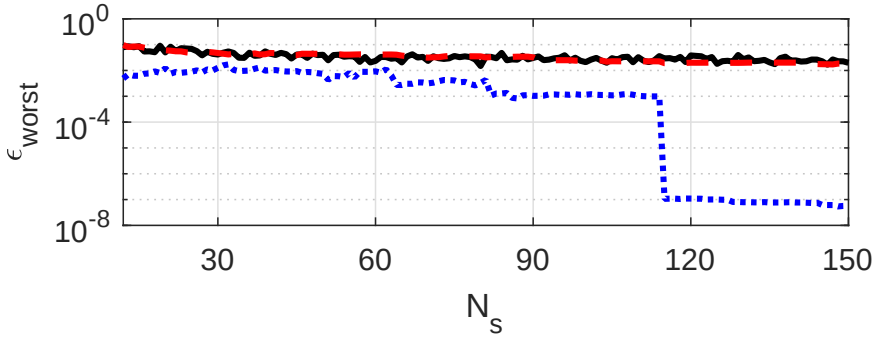

(a)

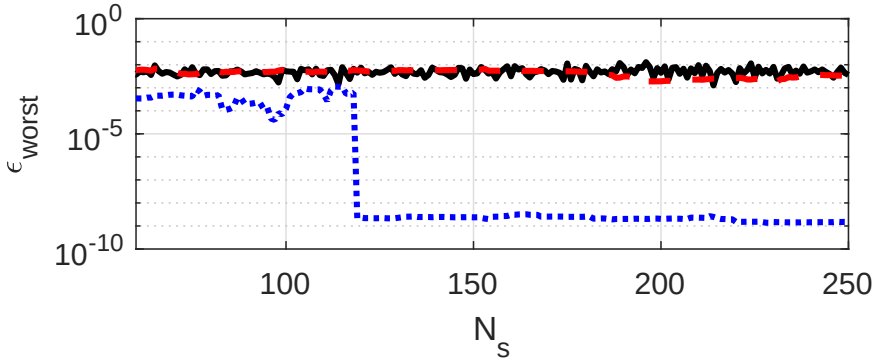

(b)

Figure 3.9: ϵ_{worst} scores for a) dipole ($d = 0.85\lambda$), and b) dipole ($d = 1.5\lambda$) For both plots: — S_1, - - - S_2, ····· S_3.

$[100, 450]$ MHz. Figure 3.6b shows a PBC unit cell model of the BLU element above a ground plane. The labelled geometric parameters are set as follows: $L = 0.693$ m, $h = 0.166$ m, $\alpha = 20°$ and $d = 1.958$ m. The selected element geometry is the optimal geometry obtained in the design study of the previous chapter — consequently, the design is poorly matched ($|\Gamma_{act}| > -10$ dB) in the 100–300 MHz band across the entire scanning range, lowering gradually with increasing frequency and leading to a wider response variation that must be accurately captured by the global model.

In this experiment, Γ_{act} is observed at the antenna's 200 Ω wire port connecting the two bowtie arms. At the lowest and highest operating frequencies, the electrical length of the array spacing d is 0.653λ (with 2 GLs entering visible space) and 2.937λ (with 31 GLs entering visible space), respectively. An initial design of 300 samples is used for the adaptively sampled models. For S_3, AF-based pre-sampling is performed in the scanning plane at a uniformly spaced set of 15 frequencies f_k, $k = 1, 2 \ldots 15$ in the 100–450 MHz frequency range. To keep the initial design set at a reasonable size and scale with the response complexity, the pre-sample size at frequency f_k is set as $P(f_k) = \text{round}(\frac{2N_{GL}(f_k)}{3})$.

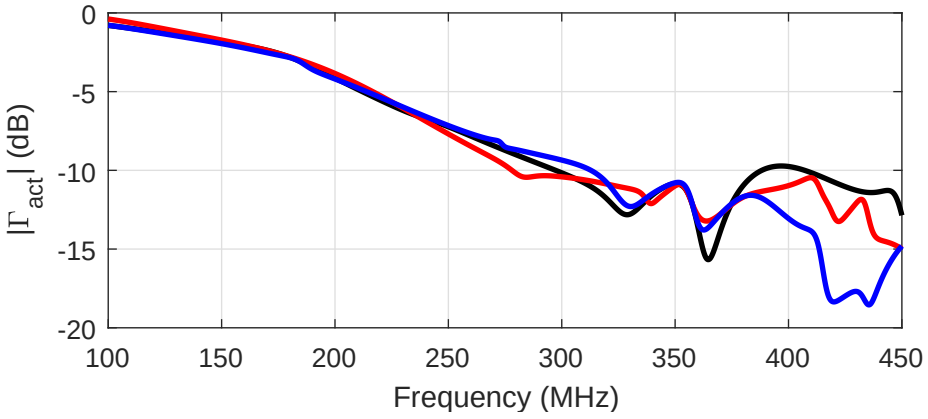

Figure 3.10: Simulated Γ_{act} vs. frequency for the BLU antenna geometry considered in this chapter: —$(\theta_0, \phi_0) = (0°, \phi_0)$, —$(\theta_0, \phi_0) = (60°, 0°)$, and —$(\theta_0, \phi_0) = (60°, 90°)$.

For the particular BLU geometry considered here, the aforementioned poor impedance match in the 100–300 MHz range diminishes the influence of GLs on the Γ_{act} response surface shape. However, in the 300–450 MHz range, $|\Gamma_{act}| < -10$ dB is required and the effect of GLs on Γ_{act} remains a concern. Hence, $\epsilon_{worst}(N_s)$ of the BLU antenna experiment is plotted for $f \geq 300$ MHz, where the maximum validation $|\Gamma_{act}| = 0.395$ (-8.06 dB) at $(\theta_0, \phi_0, f) = (22°, 45°, 310$ MHz), which is near an intersection of GL incursion loci. The three sampling schemes perform similarly to those of the dipole experiments — in the case of S_3, the AF-based pre-sampling places a sample near the validation maximum and leads to an initially low ϵ_{worst} as well as continual focused improvement of ϵ_{worst} with increasing N_s.

3.2.3 Discussion

As a whole, the numerical results indicate that the sampling scheme of S_3 is well-suited to both global modelling and the estimation of the global maximum $|\Gamma_{act}(\theta_0, \phi_0, f)|$ of broadband antenna elements in large sparse-regular phased arrays. The AF-based pre-sampling of S_3 helps to ensure that the initial design begins with samples in regions of rapid response variation where GLs enter the visible region, after which the adaptive sampling scheme selects samples to build a globally accurate model.

Although S_3 loses some initial global modelling accuracy, quantified by ϵ_{mean} in the three experiments, it is shown that the application of an appropriate adaptive sampler such as LOLA-Voronoi can be used to improve ϵ_{mean} to the same level as S_2 while simultaneously bringing ϵ_{worst} several orders of magnitude below the other sampling schemes.

The modelling techniques presented are well-suited to characterising the scan- and frequency-dependent impedance behaviour of sparse-regular AA el-

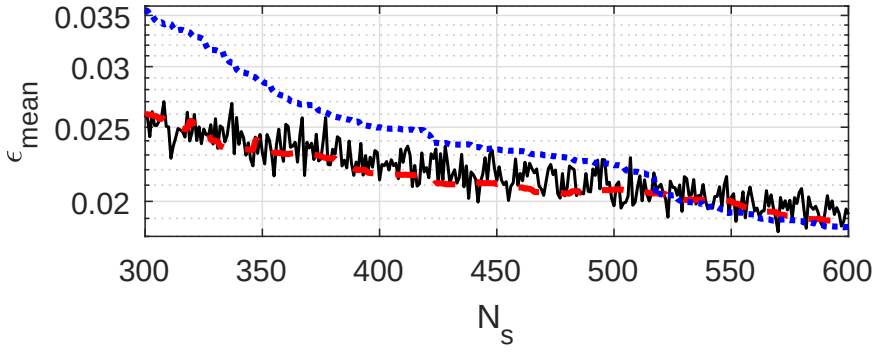

(a)

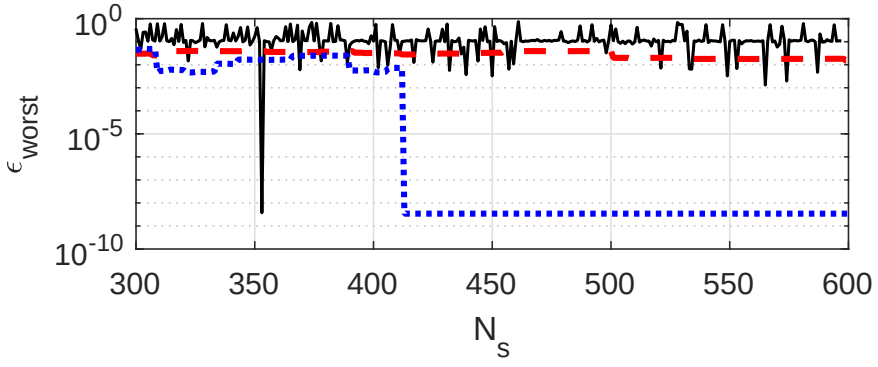

(b)

Figure 3.11: BLU element a) ϵ_{mean} score, and b) ϵ_{worst} score. For both plots: — S_1, - - - S_2, ····· S_3.

ements, and may be readily inserted into a larger optimisation loop. The S_3 model building scheme can be used to rapidly and accurately determine antenna impedance response performance against a set of design criteria, driving the attainment of an objective function to be optimised over one or multiple design parameters. This type of optimisation structure is considered in further detail in Chapter 5.

3.3 Conclusion

This chapter has investigated several adaptively sampled model construction techniques for the active reflection coefficient of narrowband and broadband sparse-regular AA elements over two-dimensional (θ_0, ϕ_0) and three-dimensional (θ_0, ϕ_0, f) operational parameter spaces. Global Surrogate modelling has been applied for the first time to this problem type, and adaptively sampled models have been shown to exhibit superior performance to standard space-filling techniques.

A pre-sampling method based on the fundamental theory of regular an-

tenna arrays has been proposed to augment the initial design of the model, which has been proven in several numerical examples to attain a significantly better estimate of the maximum $|\Gamma_{act}|$ than the other considered techniques. It is emphasised here that the density-based pre-sampling of the GL loci intersections is computationally efficient and performed once, before the adaptive modelling process is initiated. The pre-sampling is also performed *a priori* without requiring any high-fidelity simulation data, and may be done for an arbitrary scanning range and regular array layout. The method permits several degrees of control to the user to set the density-based sampling as desired, with suggested settings provided for general use.

The main contribution of this chapter is the set of modelling techniques developed for scan-dependent sparse-regular AA impedance responses, including the density-based selection of GL locus intersection points and consequent pre-sampling method. These techniques have been detailed in a communication submitted to the *IEEE Transactions on Antennas and Propagation* journal [29].

The following chapter goes on to investigate similar modelling techniques for the unit cell far-field radiation responses, focusing on the efficient modelling of full unit cell far-fields over scan angle and frequency.

Chapter 4

Orthogonal Basis Function Decomposition of Unit Cell Far-fields

The previous chapter considered the problem of modelling the active reflection coefficient of sparse-regular AA elements over frequency and scan angle, particularly focusing on the convergence of the response model error versus the number of high-fidelity samples used to build the Γ_{act} model. As pointed out in Chapter 2, however, a full picture of the element response behaviour includes characterisation of the impedance *and* radiation responses, the latter being $\overrightarrow{E}_{uc-\Omega_0}$ for an AA unit cell.

Whereas Γ_{act} is a single complex number for each parametric combination of frequency and scan angle, $\overrightarrow{E}_{uc-\Omega_0}$ is a continuous complex far-field function of θ and ϕ that must be interpolated across frequency and scan angle. Although a discrete set of spherical angles could be chosen to interpolate, this is an inelegant option due to its high computational expense for most practical requirements (a discrete set of field points with 5° angular resolution requires 2701 interpolants, while 1° resolution requires 65341 interpolants.) While the construction of these global model interpolants are, in general, significantly faster than a high-fidelity EM simulation of an AA antenna element unit cell (especially for electrically large broadband elements), the task of generating several thousands of multivariate interpolants is certain to diminish the overall computational efficiency of the modelling procedure, particularly for methods such as Ordinary Kriging whose computational expense is $\mathcal{O}(N^3)$ for N high-fidelity samples [76]. As an alternative, methods are considered which decompose the far-fields into a weighted set of orthogonal basis functions; these weights are typically much fewer in number than a set of discrete far-field points, requiring significantly less computational cost to interpolate across the operating parameters.

In this chapter, two orthogonal basis function decomposition techniques

for antenna far-fields are investigated, with the intention of using them to efficiently model AA unit cell far-fields as functions of frequency and scan angle. These are known as the *Spherical Wave Expansion* (SWE) method and the *Characteristic Basis Function Pattern* (CBFP) method, respectively. When combined with the impedance response modelling techniques explored in Chapter 3, a set of global models are provided for the fundamental antenna element responses, which can further be applied in determining key radiometric figures-of-merit such as receiving sensitivity and intrinsic cross-polarisation ratio (IXR) [77] in a dual-polarised system. Station beam patterns may also be approximated from the unit cell far-fields, as discussed in Chapter 2.

To date, no structured comparison has been made between the SWE and CBFP decomposition methods for any type of design-oriented antenna modelling problem, yet individual studies have been performed for both techniques on a variety of antenna problems [71, 74, 78–80]. The positive results of these studies serve as motivation to investigate SWE and CBFP for antenna elements in PBC unit cells, which are a class of antennas that have not been covered by any of the aforementioned studies.

Section 4.1 gives a concise exposition of the SWE, whereas Section 4.2 covers the CBFP; Section 4.3 discusses how the coefficients of each are to be interpolated across a multivariate parameter space of operational parameters including frequency. The two methods are compared for accuracy and efficiency in Section 4.4 across a number of antenna types, including AA antenna elements in a PBC unit cell. Section 4.5 concludes.

4.1 Spherical Wave Expansion

The spherical wave expansion is a classical electromagnetic field decomposition technique, first formulated by Stratton in 1941 [81]. The technique has seen extensive use in the fields of spherical near-field antenna scanning measurements [82], and is implemented in various full-wave EM solver software packages to decompose simulated electric and magnetic near- or far-fields [36,42,83].

The SWE expands a target radiated near- and far-field, defined on a spherical surface with nonzero radius (infinite radius if working with a far-field) centred at the origin, into an infinite series of physics-based, orthogonal weighted basis functions, known as *spherical modes*. These modal functions are considered to be "physics-based" because they arise from Maxwell's Equations and are solutions to the vector wave equation in spherical coordinates. This underlying physical connection between the radiated field and the equivalent set of SWE modes is favourable, since fewer modal functions are usually required to fully describe the target field than a set of basis functions with weaker or no physical similarity.

In the literature, two sets of modal functions are defined; the *standard* and *power-normalised* modes, respectively [82]. In this work, the power-normalised

(otherwise known as the *Q-mode*) formulation is chosen to work with for its compatibility with floating point arithmetic, as well as the convenience that the radiated power of each mode is fully and concisely described by its corresponding Q-coefficient.

Given a target electric (or magnetic) vector field $\overrightarrow{E}$ ($\overrightarrow{H}$) as a function of the spherical coordinates (r, θ, ϕ), its Q-mode spherical wave expansion is given by

$$\overrightarrow{E}(r,\theta,\phi) = k\sqrt{\zeta}\sum_{s=1}^{2}\sum_{n=1}^{N}\sum_{m=-n}^{n} Q_{smn}\overrightarrow{f}_{smn}(r,\theta,\phi), \tag{4.1}$$

$$\overrightarrow{H}(r,\theta,\phi) = \frac{jk}{\sqrt{\zeta}}\sum_{s=1}^{2}\sum_{n=1}^{N}\sum_{m=-n}^{n} Q_{smn}\overrightarrow{f}_{(3-s),m,n}(r,\theta,\phi), \tag{4.2}$$

where k is the free-space wave number, ζ is the free-space wave impedance, Q_{smn} is the modal weight/coefficient, $\overrightarrow{f}_{smn}$ is the spherical mode function and (s, m, n) are the integer mode indices. The index s indicates whether the mode is transverse-electric ($s = 1$) or transverse-magnetic ($s = 2$) to the radial variable r, while the indices m, n are azimuthal and polar mode-numbers, respectively.

The target field is then a weighted linear summation of spherical modal functions, each of which is defined as

$$\overrightarrow{f}_{1mn}(r,\theta,\phi) = \frac{1}{\sqrt{2\pi}}\frac{1}{\sqrt{n(n+1)}}\left(-\frac{m}{|m|}\right)^{m}\overrightarrow{m'}_{mn}(r,\theta,\phi), \tag{4.3}$$

$$\overrightarrow{f}_{2mn}(r,\theta,\phi) = \frac{1}{\sqrt{2\pi}}\frac{1}{\sqrt{n(n+1)}}\left(-\frac{m}{|m|}\right)^{m}\overrightarrow{n'}_{mn}(r,\theta,\phi), \tag{4.4}$$

where the modal subfunctions $\overrightarrow{m'}_{mn}$ and $\overrightarrow{n'}_{mn}$ are:

$$\begin{aligned}\overrightarrow{m'}_{mn}(r,\theta,\phi) = &-h_n^{(2)}(kr)\frac{jm\bar{P}_n^{|m|}\cos\theta}{\sin\theta}e^{-jm\phi}\overrightarrow{\hat{a}}_\theta \\ &-h_n^{(2)}(kr)\frac{d(\bar{P}_n^{|m|}(\cos\theta))}{d\theta}e^{-jm\phi}\overrightarrow{\hat{a}}_\phi,\end{aligned} \tag{4.5}$$

$$\begin{aligned}\overrightarrow{n'}_{mn}(r,\theta,\phi) = &\frac{n(n+1)}{kr}h_n^{(2)}(kr)\bar{P}_n^{|m|}(\cos\theta)e^{-jm\phi}\overrightarrow{\hat{a}}_r \\ &+\frac{1}{kr}\frac{d}{d(kr)}\left(krh_n^{(2)}(kr)\right)\frac{d\left(\bar{P}_n^{|m|}(\cos\theta)\right)}{d\theta}e^{-jm\phi}\overrightarrow{\hat{a}}_\theta, \\ &-\frac{1}{kr}\frac{d}{d(kr)}\left(krh_n^{(2)}(kr)\right)\frac{jm\bar{P}_n^{|m|}(\cos\theta)}{\sin\theta}e^{-jm\phi}\overrightarrow{\hat{a}}_\phi\end{aligned} \tag{4.6}$$

where $\bar{P}_n^{|m|}(\cos\theta)$ is the normalised associated Legendre polynomial [84]

$$\bar{P}_n^{|m|}(\cos\theta) = \sqrt{\frac{2n+1}{2}\frac{(n-m)!}{(n+m)!}}(\sin\theta)^{|m|}\frac{d^{|m|}P_n(\cos\theta)}{d(\cos\theta)^{|m|}} \ , \ m \leq n, \tag{4.7}$$

wherein the Legendre polynomial $P_n(\cos\theta)$ is given by

$$P_n(\cos\theta) = \frac{1}{2^n n!}\frac{d^n}{d(\cos\theta)^n}\left(\cos^2\theta - 1\right)^n \ , \ n \geq 0, \tag{4.8}$$

and where $h_n^2(kr)$ is the spherical Hankel function of the second kind [84], described by the recurrence relation

$$h_{n-1}^{(2)}(kr) + h_{n+1}^{(2)}(kr) = (2n+1)\frac{h_n^{(2)}(kr)}{kr}, \tag{4.9}$$

and

$$h_0^{(2)}(kr) = j\frac{e^{-jkr}}{kr}, \tag{4.10}$$

$$h_1^{(2)}(kr) = \left(-1 + \frac{j}{kr}\right)\frac{e^{-jkr}}{kr}. \tag{4.11}$$

Further, the derivatives of $h_n^2(kr)$ are described by the recurrence relation

$$\frac{1}{kr}\frac{d}{dkr}\left\{krh_n^{(2)}(kr)\right\} = h_{n-1}^{(2)}(kr) - n\frac{h_n^{(2)}(kr)}{kr}. \tag{4.12}$$

The above expressions for the spherical modes are well-defined functions on the interval $[-1;1]$, corresponding to the range of $\cos\theta$ for polar angles $\theta \in [0;\pi]$. Only the Q-coefficients then remain as the unknown quantities that must be determined, in order to fully describe the target field in terms of the spherical modes.

It should be noted that two differing conventions exist regarding the formulation of the SWE Q-mode functions — The first is detailed by [27] and is used internally by FEKO, while the second appears in the GRASP reflector antenna simulation software package [83]. The two formulations differ in the sign of the m-index terms that appear in $\overrightarrow{m'}_{mn}$ and $\overrightarrow{n'}_{mn}$. This dissertation follows the conventions used by GRASP to remain aligned with the definition of its *SPH* spherical wave file format, which is also the file format that FEKO uses to export SWE far-field decompositions.

4.1.1 Attaining Q-coefficients

Assume a target electric field $\overrightarrow{E}(r,\Omega)$, with $\Omega = (\theta,\phi)$, to be expressed with SWE. The field is also assumed to be measured or simulated at N_p different

spherical angles $S_p = \{\Omega_k\}_{k=1}^{N_p}$ on the surface of a sphere of radius r_M centred at the origin of the global coordinate system. The field quantities can be expressed as a column vector by stacking the field components as

$$\mathbf{E}(r_M, \Omega) = \begin{bmatrix} E_{r,\Omega_1} & \cdots & E_{r,\Omega_{N_p}} & E_{\theta,\Omega_1} & \cdots & E_{\theta,\Omega_{N_p}} & E_{\phi,\Omega_1} & \cdots & E_{\phi,\Omega_{N_p}} \end{bmatrix}^T, \tag{4.13}$$

where E_{ψ,Ω_k} denotes the ψ-component (ψ acting as a placeholder for either r, θ or ϕ) of $\overrightarrow{E}(r_M, \Omega_k)$. Each spherical mode function $\overrightarrow{f}_{smn}$ may similarly be expressed as a $3N_p \times 1$ complex column vector, determined at the same N_p spherical angles as $\mathbf{E}(r_M, \Omega)$ and given by

$$\mathbf{f}(r_M, \Omega) = \begin{bmatrix} f_{r,\Omega_1} & \cdots & f_{r,\Omega_{N_p}} & f_{\theta,\Omega_1} & \cdots & f_{\theta,\Omega_{N_p}} & f_{\phi,\Omega_1} & \cdots & f_{\phi,\Omega_{N_p}} \end{bmatrix}^T. \tag{4.14}$$

If the target E-field is a far-field, then $r_M \to \infty$ and the above expressions reduce to $2N_p \times 1$ complex column vectors,

$$\mathbf{E}(\infty, \Omega) = \begin{bmatrix} E_{\theta,\Omega_1} & \cdots & E_{\theta,\Omega_{N_p}} & E_{\phi,\Omega_1} & \cdots & E_{\phi,\Omega_{N_p}} \end{bmatrix}^T \tag{4.15a}$$

$$\mathbf{f}(\infty, \Omega) = \begin{bmatrix} f_{\theta,\Omega_1} & \cdots & f_{\theta,\Omega_{N_p}} & f_{\phi,\Omega_1} & \cdots & f_{\phi,\Omega_{N_p}} \end{bmatrix}^T. \tag{4.15b}$$

For the moment, assume that a finite set of spherical modes with j-indices $1, 2 \cdots N_j$ are sufficient to fully represent the target field. These j-indices are related to the (s, m, n)-indices by [27]

$$j = 2\left(n(n+1) + m - 1\right) + s. \tag{4.16}$$

Equation 4.1 may then be rewritten in matrix form as

$$\mathbf{E} = \mathbf{F}\mathbf{Q} = \begin{bmatrix} \mathbf{f}_1, \mathbf{f}_2 \cdots \mathbf{f}_{N_j} \end{bmatrix} \begin{bmatrix} Q_1, Q_2 \cdots Q_{N_j} \end{bmatrix}^T. \tag{4.17}$$

Equation 4.17 represents a system of linear equations, for which $\mathbf{Q}$ can generally be approximated as

$$\mathbf{Q} = \mathbf{F}^{\dagger}\mathbf{E}, \tag{4.18}$$

where the superscript † denotes the matrix pseudoinverse. In most cases, $N_j < 3N_p$ (or $2N_p$ for far-fields), and (4.18) represents the least-squares solution for the Q-coefficients. Note that when $\mathbf{F}$ is square, the pseudo-inverse reduces to a standard matrix inverse and the exact solution to $\mathbf{Q}$ is obtained.

A distinct strength of the SWE is that, once accurately obtained, the Q-coefficients may be used to reconstruct the desired far-field using (4.1) or (4.2) over an arbitrary set of spherical pointing angles. However, it is also required that the set of pointing angles chosen to build the $\mathbf{F}$-matrix covers the angular range $\theta \in [0°, 180°]$, $\phi \in [0°, 360°]$ and is sampled with high enough angular resolution to ensure that $\mathbf{F}$ is well-conditioned. This is illustrated in Figure

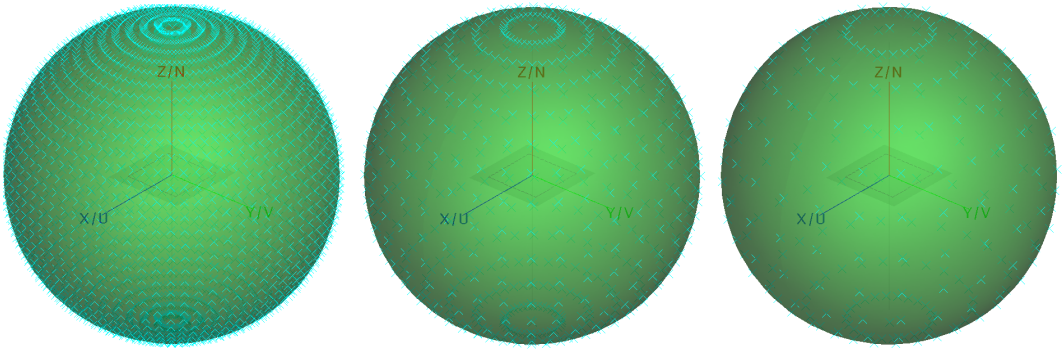

Figure 4.1: Far-field sampling grids with angular resolutions of 5° (left), 10° (middle), and 15° (right).

Table 4.1: Condition numbers of the SWE **F**-matrix for far-field sampling grids of varying angular resolution.

Angular Resolution	$\kappa(\mathbf{F})$
1°	3.454
5°	3.8709
10°	4.3486
15°	9.379×10^{15}

4.1 and Table 4.1 for an **F**-matrix with $N_j = 336$. It can be seen that the condition number $\kappa(\mathbf{F})$ slowly increases as the angular resolution broadens, until **F** becomes near-singular for 15° resolution, indicating that the far-field is undersampled. To prevent this situation and maintain a well-conditioned **F**-matrix, all of the far-fields in this chapter are assumed to be simulated with 5° angular resolution for a total of 2701 points per field component.

The definitive literature on spherical near-field scanning measurements advocates that this matrix inversion technique is to be avoided in favour of a numerical integration technique that makes use of the orthogonality of the spherical mode functions [82]. However, contemporary standards of processing power in personal computers combined with matrix-oriented software such as MATLAB make matrix inversion a straightforward procedure. Furthermore, it has been shown for several antenna modelling cases (including a sparse-regular AA example) that finding the Q-coefficients by numerical pseudo-inversion of **F** provides a more accurate and efficient solution than the integral method [85]. In this dissertation, the Q-coefficients are henceforth assumed to be attained via (4.18).

4.1.2 Maximum Number of Modes

Although the ideal spherical wave representation of a far-field consists of an infinite weighted summation of spherical modes, practical implementations of

the SWE truncate the summation by electing maximum polar and azimuthal mode-numbers, referred to here as N_{max} and M_{max} respectively. The designer is also at liberty to choose specific mode-numbers to include in the summation when properties of the antenna current distribution (and thereby the radiation pattern) are known *a priori*, such as selecting a specific value of m to include when the current distribution is known to be rotationally symmetric along the azimuthal coordinate ϕ.

A common choice in EM solvers that use the SWE, such as FEKO, is to set $M_{max} = N_{max}$, and then to determine N_{max} as a function of the so-called *minimum sphere* labelled r_{min} which contains the full geometry of the antenna [27]. The minimum sphere is standardly centred at the phase reference point and the origin of the global coordinate system. A commonly-used formula for N_{max} based on r_{min} which guarantees a sufficient degree of numerical accuracy is then [27, 36, 83]

$$N_{max} = kr_{min} + \max\left(3.6\sqrt[3]{kr_{min}}, 10\right). \tag{4.19}$$

For antenna elements in a PBC unit cell, the minimum sphere is not as well-defined as it is for an isolated antenna — given that the simulated array structure is infinite in extent, the definition of the minimum sphere becomes an approximation that captures the major electromagnetic interaction of the unit cell element and its neighbours. This only becomes significantly detrimental to the model if the dominant modes occur for high mode numbers or j-indices. This concern is further addressed later in this chapter, for several far-field modelling examples of antenna elements in PBC unit cells.

4.2 Characteristic Basis Function Patterns

The Characteristic Basis Function Pattern (CBFP) method is an orthogonal basis function decomposition technique originally developed to analyse the embedded element patterns and scanned beam patterns of antenna arrays [86, 87], and further applied to modelling perturbations in reflector antenna patterns due to temporary displacements and deformations of the reflector structure [88]. While the initial modelling focus of the CBFP method was for calibration purposes, [74] further developed CBFPs to model antenna radiation patterns over multivariate parameter spaces for design and optimisation tasks.

Much like the SWE, the CBFP method decomposes antenna far-fields into an orthogonal set of weighted basis functions. The choice of basis is the key difference — whereas SWE draws it basis from the solutions to the vector wave equation, the CBFP method uses an orthogonalised set of far-fields sampled from the design space as its basis. This choice of basis is effective when a suitable set of design points (and corresponding CBFPs) are selected that

span the space of all radiation patterns occurring within the design space, allowing any far-field in the space to be accurately reconstructed as a linear combination of the CBFPs.

4.2.1 Attaining CBFP Coefficients

Given a target electric (or magnetic) vector far-field $\overrightarrow{E}(\Omega)$, with θ- and ϕ-components denoted as E_θ and E_ϕ respectively, its CBFP expansion is given by

$$E_\theta(\Omega) = \sum_{n=1}^{N_{CBFP}} w_{\theta,n} f_{\theta,n}(\Omega) \tag{4.20a}$$

$$E_\phi(\Omega) = \sum_{n=1}^{N_{CBFP}} w_{\phi,n} f_{\phi,n}(\Omega), \tag{4.20b}$$

where $f_{\theta,n}$ and $f_{\phi,n}$ are the θ- and ϕ-components of the n^{th} CBFP vector far-field $\overrightarrow{f}_n(\theta,\phi)$ in a set of N_{CBFP} basis functions, and w denotes the corresponding complex scalar CBFP coefficients. If it is assumed that the target far-field is measured or simulated at N_p different spherical angles $S_p = \{\Omega_k\}_{k=1}^{N_p}$, such that its θ- and ϕ-components can be represented as two complex $N_p \times 1$ column vectors

$$\mathbf{E}_\theta(\Omega) = \begin{bmatrix} E_{\theta,\Omega_1} & \cdots & E_{\theta,\Omega_{N_p}} \end{bmatrix}^T \tag{4.21a}$$

$$\mathbf{E}_\phi(\Omega) = \begin{bmatrix} E_{\phi,\Omega_1} & \cdots & E_{\phi,\Omega_{N_p}} \end{bmatrix}^T. \tag{4.21b}$$

The θ- and ϕ-components of each CBFP far-field $\overrightarrow{f}_n$, also simulated or measured over S_p, may similarly be expressed as

$$\mathbf{f}_{\theta,n}(\Omega) = \begin{bmatrix} f_{\theta,\Omega_1} & \cdots & f_{\theta,\Omega_{N_p}} \end{bmatrix}^T \tag{4.22a}$$

$$\mathbf{f}_{\phi,n}(\Omega) = \begin{bmatrix} f_{\phi,\Omega_1} & \cdots & f_{\phi,\Omega_{N_p}} \end{bmatrix}^T. \tag{4.22b}$$

For the moment, assume that a finite set of N_{CBFP} CBFPs are sufficient to fully represent the target field, and that these CBFPs form an orthogonal set of basis functions. Equation (4.20) may then be rewritten in matrix form as

$$\mathbf{E}_\theta = \mathbf{F}_\theta \mathbf{w}_\theta = [\mathbf{f}_{\theta,1}, \ \cdots \ \mathbf{f}_{\theta,N_{CBFP}}] \, [w_{\theta,1}, \ \cdots \ w_{\theta,N_{CBFP}}]^T \tag{4.23a}$$

$$\mathbf{E}_\phi = \mathbf{F}_\phi \mathbf{w}_\phi = [\mathbf{f}_{\phi,1}, \ \cdots \ \mathbf{f}_{\phi,N_{CBFP}}] \, [w_{\phi,1}, \ \cdots \ w_{\phi,N_{CBFP}}]^T. \tag{4.23b}$$

Equation (4.23) represents two systems of linear equations, for which the CBFP coefficient vectors $\mathbf{w}_\theta$ and $\mathbf{w}_\phi$ can generally be solved as

$$\mathbf{w}_\theta = \mathbf{F}_\theta^\dagger \mathbf{E}_\theta \tag{4.24a}$$
$$\mathbf{w}_\phi = \mathbf{F}_\phi^\dagger \mathbf{E}_\phi. \tag{4.24b}$$

However, it is generally not guaranteed that the CBFPs form an orthogonal basis, necessitating an additional orthogonalisation step. This is realised by performing singular value decomposition (SVD) on $\mathbf{F}_\theta$ and $\mathbf{F}_\phi$ to obtain

$$\mathbf{F}_\theta = \mathbf{U}_\theta \mathbf{\Sigma}_\theta \mathbf{V}_\theta^* \tag{4.25a}$$
$$\mathbf{F}_\phi = \mathbf{U}_\phi \mathbf{\Sigma}_\phi \mathbf{V}_\phi^*, \tag{4.25b}$$

where $\cdot^*$ denotes the matrix conjugate transpose. $\mathbf{U}_\theta$ and $\mathbf{U}_\phi$ now form orthonormal bases for the respective column spaces of $\mathbf{F}_\theta$ and $\mathbf{F}_\phi$, and the CBFP coefficients are then given by

$$\mathbf{w}_\theta = \mathbf{U}_\theta^\dagger \mathbf{E}_\theta \tag{4.26a}$$
$$\mathbf{w}_\phi = \mathbf{U}_\phi^\dagger \mathbf{E}_\phi. \tag{4.26b}$$

The target field may then be reconstructed by using (4.23) and substituting $\mathbf{U}_\theta$ and $\mathbf{U}_\phi$ for their corresponding $\mathbf{F}$-matrices.

Note that this solution is specific to S_p; that is to say, the far-field reconstruction only produces field values at the discrete set of spherical pointing angles contained in S_p. Although it is assumed in this dissertation that the desired far-fields are described in sufficient detail over S_p, it is also possible to reconstruct the fields with $\mathbf{w}_\theta$ and $\mathbf{w}_\phi$ over an alternate set of N_a spherical pointing angles $S_a = \{(\theta_i, \phi_i)\}_{i=1}^{N_a}$ — this is a situation that arises, for instance, in reflector antenna calibration where one is restricted to a limited set of far-field measurements, yet the far-field is desired over a broader angular range [89]. In this case, an alternate CBFP matrix must be defined as [89]

$$\mathbf{F}_{a\theta} = [\mathbf{f}_{a\theta,1}, \mathbf{f}_{a\theta,2} \ \cdots \mathbf{f}_{a\theta,N_{CBFP}}] \tag{4.27a}$$
$$\mathbf{F}_{a\phi} = [\mathbf{f}_{a\phi,1}, \mathbf{f}_{a\phi,2} \ \cdots \mathbf{f}_{a\phi,N_{CBFP}}], \tag{4.27b}$$

where the alternate CBFP vectors are

$$\mathbf{f}_{a\theta,n}(\Omega) = \begin{bmatrix} f_{a\theta,\Omega_1} & \cdots & f_{a\theta\Omega_{N_a}} \end{bmatrix}^T \tag{4.28a}$$
$$\mathbf{f}_{a\phi,n}(\Omega) = \begin{bmatrix} f_{a\phi,\Omega_1} & \cdots & f_{a\phi,\Omega_{N_a}} \end{bmatrix}^T. \tag{4.28b}$$

The far-field pattern may now be reconstructed over Ω_a as

$$\mathbf{E}_{a\theta} = \mathbf{R}_\theta \mathbf{w}_\theta = [\mathbf{r}_{\theta,1} \ \cdots \ \mathbf{r}_{\theta,N_{CBFP}}]\, \mathbf{w}_\theta \tag{4.29a}$$

$$\mathbf{E}_{a\phi} = \mathbf{R}_\phi \mathbf{w}_\phi = [\mathbf{r}_{\phi,1} \ \cdots \ \mathbf{r}_{\phi,N_{CBFP}}]\, \mathbf{w}_\phi, \tag{4.29b}$$

where $\mathbf{R}_\theta$ and $\mathbf{R}_\phi$ are $N_a \times N_{CBFP}$ matrices whose k^{th} columns are given by

$$\mathbf{r}_{\theta,k} = \frac{1}{\sigma_{\theta,k}} \mathbf{F}_{a\theta} \mathbf{v}_{\theta,k} \tag{4.30a}$$

$$\mathbf{r}_{\phi,k} = \frac{1}{\sigma_{\phi,k}} \mathbf{F}_{a\phi} \mathbf{v}_{\phi,k}, \tag{4.30b}$$

where $\sigma_{\theta,k}$ and $\sigma_{\phi,k}$ denote the k^{th} singular values on the diagonals of $\mathbf{\Sigma}_\theta$ and $\mathbf{\Sigma}_\phi$, while $\mathbf{v}_{\theta,k}$ and $\mathbf{v}_{\phi,k}$ denote the k^{th} corresponding right-singular vectors. Note these reconstructed far-fields are not guaranteed to be as accurate as those reconstructed over S_p, given that $\mathbf{w}_\theta$ and $\mathbf{w}_\phi$ are specific solutions for CBFP matrices generated over S_p.

4.2.2 Spanning the Design Space

Unlike the SWE, the basis set of the CBFP is intrinsically linked to the parameter space over which the desired far-fields must be modelled. The SVD step in the generation of the CBFPs may guarantee that they are orthonormal, but it does not ensure that all far-fields in the parameter space are contained in the column spaces of $\mathbf{F}$ or $\mathbf{U}$.

Whether or not a set of CBFPs actually spans the full design space of far-fields depends on whether the set actually captures the functional behaviour of all far-fields in the design space, requiring a sufficient number of CBFPs as well as careful selection of the design points from which to sample them [74]. By comparison, the SWE only needs a large enough minimum sphere defined to ensure that its basis set spans the design space (although this may be somewhat less straightforward for elements in a PBC unit cell, as already mentioned).

This trait may be considered as a drawback of the CBFP method, as it adds an additional level of complexity that is not present in the SWE. However, this is also a possible advantage over the SWE since the CBFPs are not only physics-based patterns but specific to the design space and antenna under consideration, potentially requiring fewer basis functions (and corresponding interpolants) to generate accurate far-field models.

4.3 Interpolating Model Coefficients

In this dissertation, the goal of using either the SWE or CBFP method is to build accurate and efficient global models for AA element unit cell far-fields

across a three-dimensional parameter space of frequency and scan angle. While global model construction and interpolation is usually much less computationally expensive than performing a full-wave EM simulation of an antenna, it may still become inefficient in terms of processing time and storage if many interpolants are required. In place of interpolating hundreds or thousands of field points, a smaller set of expansion coefficients that contain full information about the far-fields are interpolated.

For the general modelling problem of an antenna far-field response across a D-dimensional space of design and/or operational parameters $x_1 \in [x_{1,min}, x_{1,max}]$, $x_2 \in [x_{2,min}, x_{2,max}]$, $\cdots$ $x_D \in [x_{D,min}, x_{D,max}]$, the modelling process is initiated by nominating a set of sample points $X_s = \{\mathbf{x}_i\}_{i=1}^{N_s} = \{(x_{1,i}, x_{2,i} \cdots x_{D,i})\}_{i=1}^{N_s}$, which serve as interpolation abscissae for the coefficient models. At each sample point in X_s, a full-wave EM simulation of the antenna is performed to yield a high-fidelity far-field response vector $\mathbf{E_i}$ over N_p spherical pointing angles and of the same form as (4.15).

4.3.1 SWE Model

If SWE is used to decompose the far-fields, the Q-coefficient vector $\mathbf{Q}_i = [Q_{i,1}Q_{i,2} \cdots Q_{i,N_j}]^T$ for each $\mathbf{x}_i$ is calculated with (4.18), subsituting $\mathbf{Q}_i$ and $\mathbf{E}_i$ for $\mathbf{Q}$ and $\mathbf{E}$, respectively. Every Q-coefficient j-index and sample point $\mathbf{x}_i$ now has exactly one scalar complex Q-coefficient value associated with it, yielding N_j scattered support sets each of N_s abscissa-ordinate pairs to be interpolated.

In most cases, the choice of N_{max} following (4.19) retains numerous Q-coefficients even for electrically small antennas, many of which have negligible magnitude. To sensibly limit the number of interpolants without losing accuracy during far-field reconstruction, the Q-coefficients may be ranked in terms of their influence on the far-fields by considering the maximum radiated power of each mode observed across X_s,

$$P_{j,max} = \max_i \frac{|Q_{i,j}|^2}{2}. \tag{4.31}$$

The $P_{j,max}$ terms may now be ranked in descending order and normalised to the maximum modal power P_{max}, with only the first N_R corresponding Q-coefficients retained for interpolation and the remaining coefficients set to zero.

A simple example of SWE decomposition is now considered for a 1 GHz half-wave dipole directed along the z-axis in free space, analysed in the 0.5–3.5 GHz frequency range. The dipole's fundamental resonant mode occurs at 1 GHz, while the next higher-order mode occurs near 3 GHz — the radiation characteristics of the former are mostly captured by the f_4 spherical mode-function, while f_{24} mostly accounts for the latter. This can be seen in Figures

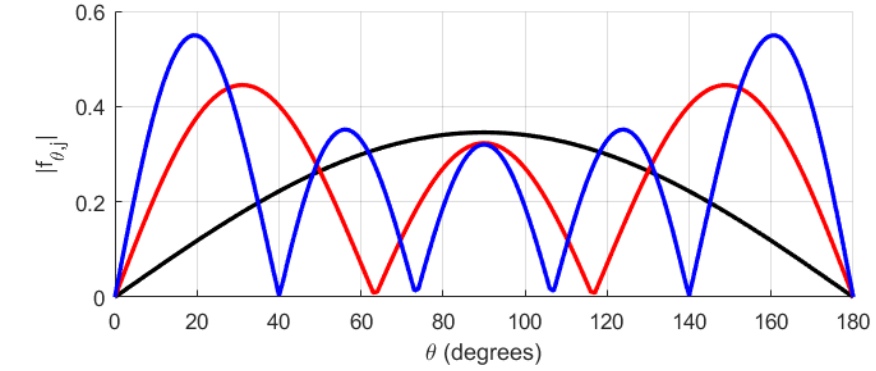

(a)

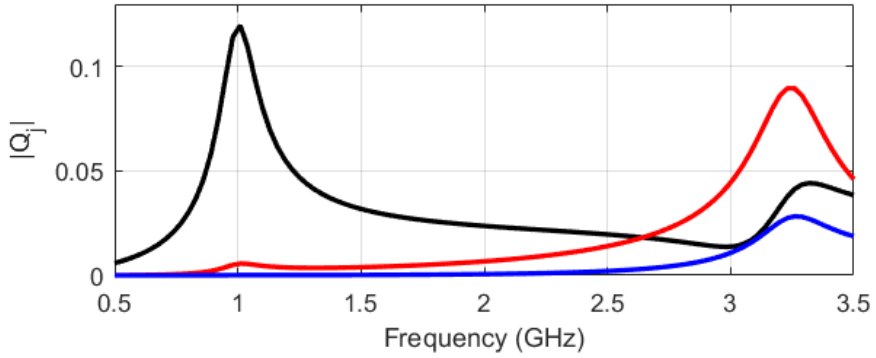

(b)

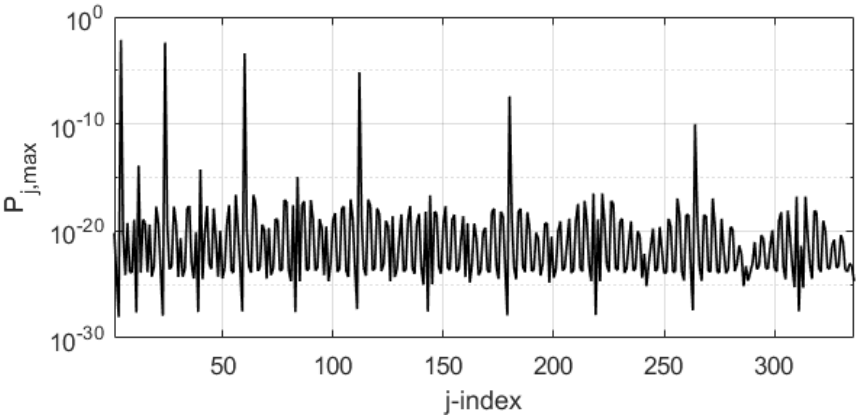

(c)

Figure 4.2: SWE decomposition of a 1 GHz half-wave z-directed dipole, analysed at 101 equidistant points across the 0.5–3.5 GHz frequency range: a) dominant $f_j(\theta)$ modal functions, b) dominant Q-coefficients, c) $P_{j,max}$.

4.2a and 4.2b, while Figure 4.2c shows the predominance of radiated power in the f_4, f_{24} and f_{60} Q-modes. The fundamental radiating modes of the half-wave dipole are very similar to the SWE modes symmetric about the z-axis ($m = 0$), allowing the far-fields to be well-approximated by only a few modal

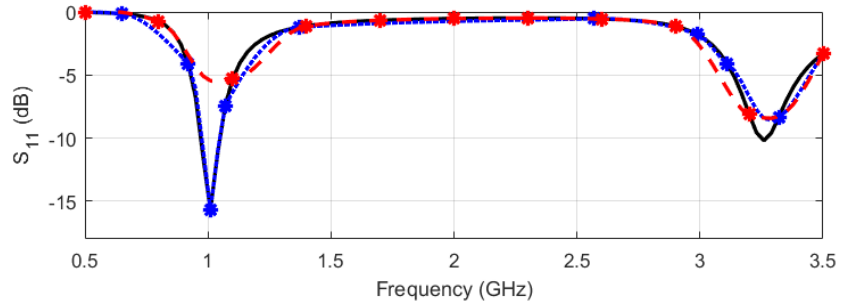

(a)

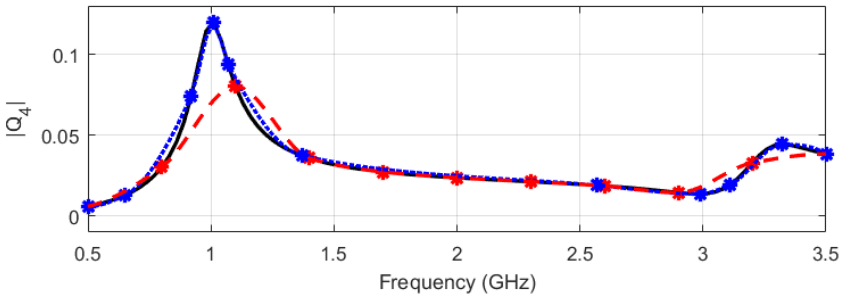

(b)

Figure 4.3: Interpolation of the 1 GHz half-wave dipole example's a) S_{11} and b) Q_4 coefficient, using sample sets of 11 equidistant sample points (- - -) and 11 hand-selected points (·····). Stars mark the locations of the sample sets, while (——) shows validation responses.

functions.

Figure 4.3 shows two frequency interpolants of the 1 GHz half-wave dipole's S_{11} the dominant Q_4 coefficient, each generated with 11 sample points and using piecewise cubic interpolation. It can be seen that the interpolants with hand-selected sample points produce a significantly more accurate result than equidistant sampling, and that the major functional variation of Q_4 occur at the same frequencies as for S_{11}. While hand-selection of sampling points is impractical for design and optimisation tasks, adaptive sampling techniques such as those considered in Chapter 3 are to be considered instead, using similar sampling schemes as in Chapter 3 with the antenna impedance response used to drive the selection of new sample points.

4.3.2 CBFP Model

If the CBFP method is used to decompose the far-fields, a set of N_s far-fields are available at the sample points with which to construct the $N_p \times N_{CBFP}$ $\mathbf{U}_\theta$ and $\mathbf{U}_\phi$ CBFP matrices ($N_{CBFP} \leq N_s$). At this point, it may be elected to retain only the first $N_R \leq N_{CBFP}$ columns of $\mathbf{U}_\theta$ and $\mathbf{U}_\phi$ and reduce the number of CBFP coefficients to interpolate — N_R is typically determined by

choosing some tolerance value ϵ and discarding all left-singular vectors whose singular values relative to the largest singular value σ_{max} are smaller than ϵ. This truncation yields the $N_p \times N_R$ $\mathbf{U}_{\mathbf{R}\theta}$ and $\mathbf{U}_{\mathbf{R}\phi}$ matrices, which are then used in place of $\mathbf{U}_\theta$ and $\mathbf{U}_\phi$.

Aside from the benefit of reducing computational burden, truncation of the $\mathbf{U}$-matrices is sensible when the major underlying behaviour of the modelled far-fields are captured with fewer CBFPs than there are sample points, causing many of the CBFPs to have negligible contribution to the far-fields or even degrade the overall accuracy of the reconstructed patterns by adding unwanted numerical noise [90].

Following the formation of $\mathbf{U}_{\mathbf{R}\theta}$ and $\mathbf{U}_{\mathbf{R}\phi}$, the CBFP coefficient vectors $\mathbf{w}_{\theta,i}$ and $\mathbf{w}_{\phi,i}$ are calculated with (4.26), subsituting $\mathbf{w}_{\theta,i}$, $\mathbf{w}_{\phi,i}$, $E_{\theta,i}$ and $E_{\phi,i}$ for $\mathbf{w}_\theta$, $\mathbf{w}_\phi$, E_θ and E_ϕ, respectively. Every CBFP coefficient n-index and sample point $\mathbf{x}_i$ now has exactly one scalar complex CBFP coefficient value associated with it, yielding N_R scattered support sets each of N_s abscissa-ordinate pairs to be interpolated.

The example of the 1 GHz half-wave dipole in free space is now considered again, for the CBFP method. Similar variation of the CBFP coefficients is seen to occur across frequency as with the SWE Q-coefficients, although the CBFPs have more significant influence at both resonant frequencies where the Q-coefficients each dominate one resonant mode. Like the SWE, only a few CBFP modes are required to capture the major far-field functional behaviour in this example.

Figure 4.5 shows two frequency interpolants of the dominant $W_{\theta,1}$ coefficient, generated with the same sample sets and piecewise cubic interpolation as in Figure 4.3. Similar results are observed as for the SWE Q-coefficient interpolation.

4.4 Comparison of Techniques

This section is composed of a set of examples for which the SWE and CBFP methods are formally compared in terms of their ability to accurately model simulated antenna far-fields over a variety of element geometries and parameter spaces. A set of free-space isolated antenna geometries are considered first, drawn from the set of antennas analysed in [74], followed by the AA-specific situation of antenna elements in a PBC unit cell (with frequency and scan angle comprising the parameter space). The isolated antennas are considered to generalise the comparison beyond the AA modelling problem specific to this dissertation and provide some verification of [74]'s work versus SWE, although the ultimate goal is to determine whether the SWE or CBFP method is most suitable for modelling scan-dependent AA element far-fields.

For all of the modelling examples that follow, it is assumed that the far-fields are to be globally modelled as part of a sequential design including the

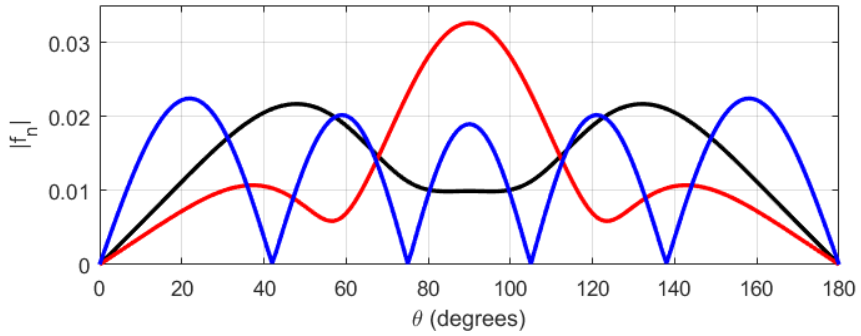

(a)

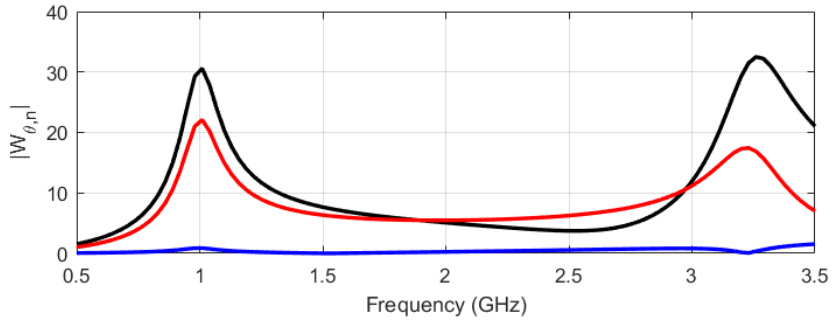

(b)

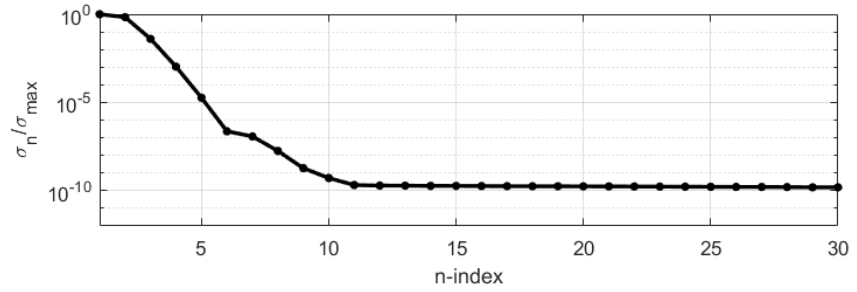

(c)

Figure 4.4: CBFP decomposition of a 1 GHz half-wave z-directed dipole, analysed at 101 equidistant points across the 0.5–3.5 GHz frequency range: a) dominant CBFPs, b) dominant CBFP coefficients, c) σ_n/σ_{max}.

global adaptive modelling of the antenna reflection coefficient $\Gamma(x_1 \cdots x_D)$ (or $\Gamma_{act}(x_1 \cdots x_D)$, in the case of PBC unit cell antenna elements). While it is possible to drive the adaptive modelling scheme with an aggregation of impedance and radiation response exploitation criteria [74], this adds additional modelling complexity and computational expense that is preferably avoided. Instead, the adaptive sampling scheme is driven by the LOLA-Voronoi algorithm trained on the (active) reflection coefficient of the antenna element, and the far-field model errors are evaluated at a few specific values of N_s where the impedance response modelling error has converged below a certain threshold. For the

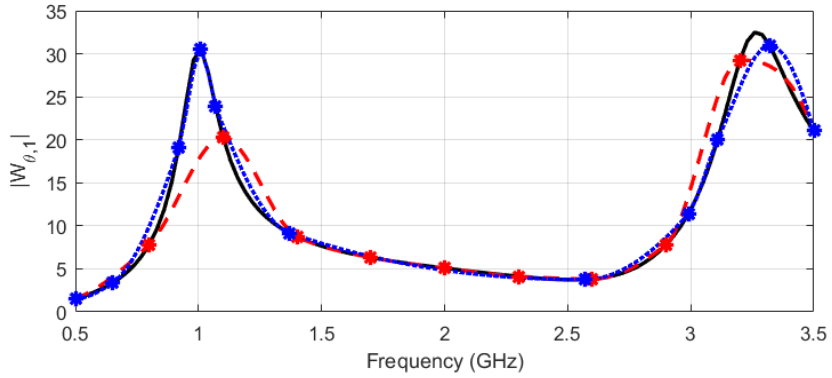

Figure 4.5: Interpolation of the 1 GHz half-wave dipole example's $W_{\theta,1}$ coefficient, using sample sets of 11 equidistant sample points (- - -) and 11 hand-selected points (·····). Stars mark the locations of the sample sets, while (——) shows the validation response.

examples drawn from [74], the far-field modelling errors can then be compared to those obtained in [74] to assess the effectiveness of driving the adaptive sampling with only the impedance response model.

As in Chapter 3, global surrogate modelling is employed to construct the response models, using Ordinary Kriging with the Matérn $(\frac{3}{2})$ correlation function. Kriging hyperparameters are set using maximum likelihood estimation and tuned to minimise the 5-fold cross-validation (CV) score of the model. For each antenna example, mean model error for the far-field responses is quantified over N_v validation points $\mathbf{x}_v = [x_{v,1} \ \cdots \ x_{v,D}]^T$, $v \in \{1, 2 \ \cdots \ N_v\}$ by the root relative mean-squared error (RRMSE) [63]

$$\epsilon_{\psi,RRMSE}(N_s) = \sqrt{\frac{\sum_{v=1}^{N_v}\sum_{p=1}^{N_p}\left|E_\psi(\mathbf{x}_v,\Omega_p) - \widetilde{E}_{\psi,N_s}(\mathbf{x}_v,\Omega_p)\right|^2}{\sum_{v=1}^{N_v}\sum_{p=1}^{N_p}\left|E_\psi(\mathbf{x}_v,\Omega_p) - \bar{E}_\psi(\mathbf{x}_v)\right|^2}}, \tag{4.32}$$

where E is the validation far-field, $\widetilde{E}$ is the far-field reconstructed with the SWE or CBFP coefficients globally modelled with N_s high-fidelity sample points, and $\bar{E}$ is the validation far-field averaged over all spherical pointing angles and validation points, and the subscript ψ denotes the ψ-component of the far-field (acting as a placeholder for either θ or ϕ).

4.4.1 Isolated Antenna Elements

4.4.1.1 Axially Corrugated Horn

The first isolated element example considers a horn antenna with a circular aperture and three axial corrugations, as depicted in Figure 4.6. The antenna

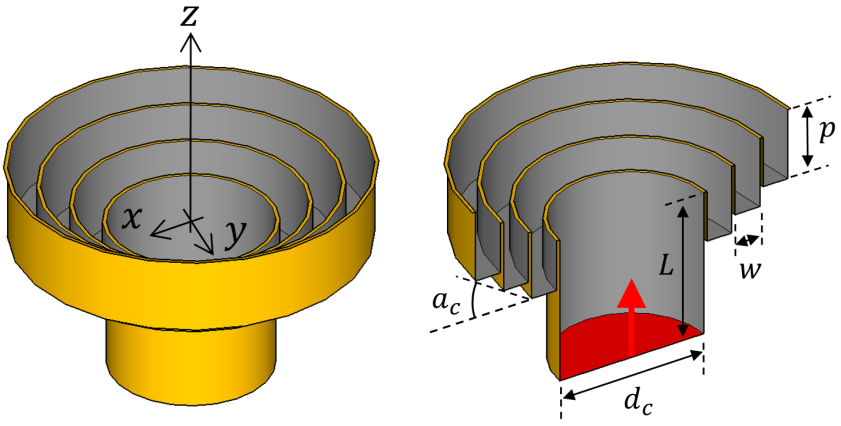

Figure 4.6: Axially corrugated horn geometry isometric view (left) and cross-section (right), with the waveguide feed port marked in red.

is parametrised by the corrugation flare angle a_c, corrugation width w, corrugation depth p, horn waveguide feed length L and horn aperture diameter d_c. The input reflection coefficient Γ is defined at the waveguide port marked in red in Figure 4.6. The antenna is simulated in FEKO MoM, in free space.

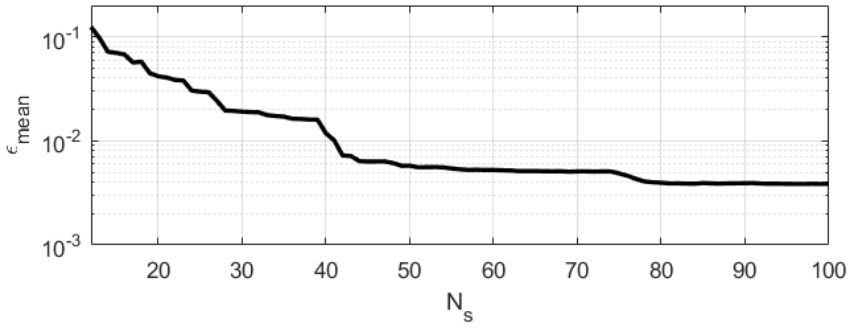

Figure 4.7: Axially corrugated horn ϵ_{mean} score for the Γ model.

In this example, a two-dimensional parameter space is considered, consisting of $x_1 = a_c \in [0°, 7°]$ and $x_2 = f \in [0.95, 1.2]$ GHz, while the remaining parameters are fixed as $w = 24$ mm, $p = 54.6$ mm, $L = 218$ mm, and $d_c = 190$ mm. The modelling process is started with a latin hypercube initial design of 10 points, as in [74], and allowed to iteratively progress until $N_s = 100$. As can be seen in Figure 4.7, the ϵ_{mean} error for Γ steadily decreases until it is 3.873×10^{-3} at $N_s = 100$. It should be noted that the curve flattens considerably for $N_s > 50$, indicating that the model is near convergence well before the maximum number of samples is reached.

Figure 4.8 shows ϵ_{RRMSE} for both field components, using SWE and CBFP. The errors are considered at $N_s = 50$, where the Γ model is near convergence, and at the maximum $N_s = 100$ — both models are seen to converge towards

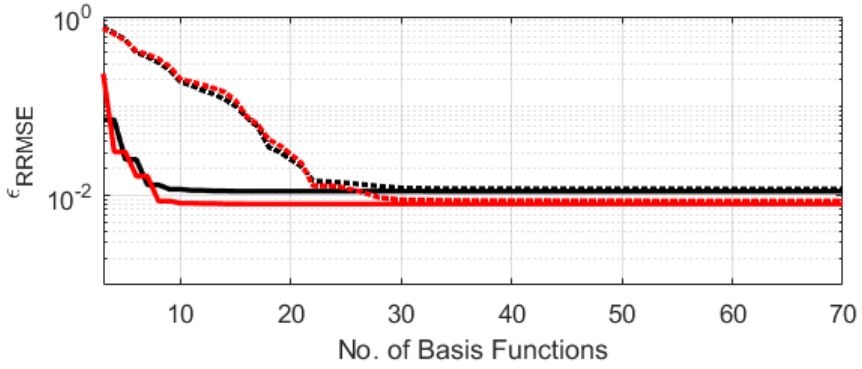

(a)

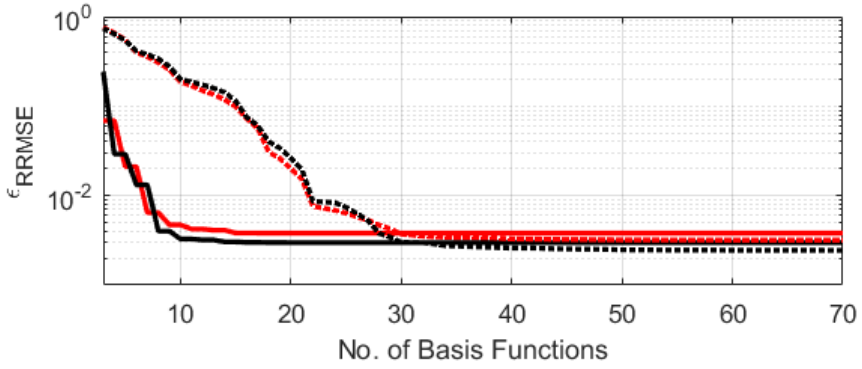

(b)

Figure 4.8: Axially corrugated horn far-field model error scores — a) ϵ_{RRMSE} ($N_s = 50$), and b) ϵ_{RRMSE} ($N_s = 100$). For both plots: (—) CBFP E_θ, (—) CBFP E_ϕ, (·····) SWE E_θ, (·····) SWE E_ϕ.

significantly lower minimum ϵ_{RRMSE} at $N_s = 100$, showing that the far-field model error decreases proportionally to the impedance response model error. For $N_s = 50$, ϵ_{RRMSE} converges around 15 basis functions for CBFP, and near 30 basis functions for SWE — considering that two interpolants must be generated per basis function for CBFP while SWE only requires one per basis function, it is evident that the two methods are roughly equal here in terms of modelling accuracy and computational expense.

Similar results are observed for $N_s = 100$, although the CBFP ϵ_{RRMSE} in this instance converges with fewer than 10 basis functions and requiring no more than 20 CBFP coefficient interpolants for accurate far-field models versus the 30+ required for SWE.

The normalised CBFP singular values and SWE $P_{j,max}$ terms for $N_s = 100$ are plotted in Figure 4.9, with $P_{j,max}$ shown both in its natural j-indexing order and sorted in descending order of magnitude. Note that although the CBFP singular values and SWE $P_{j,max}$ terms are not directly equivalent terms and should not be compared as though they were, the general trends of these terms with respect to their basis function indices provide insight into which (and how

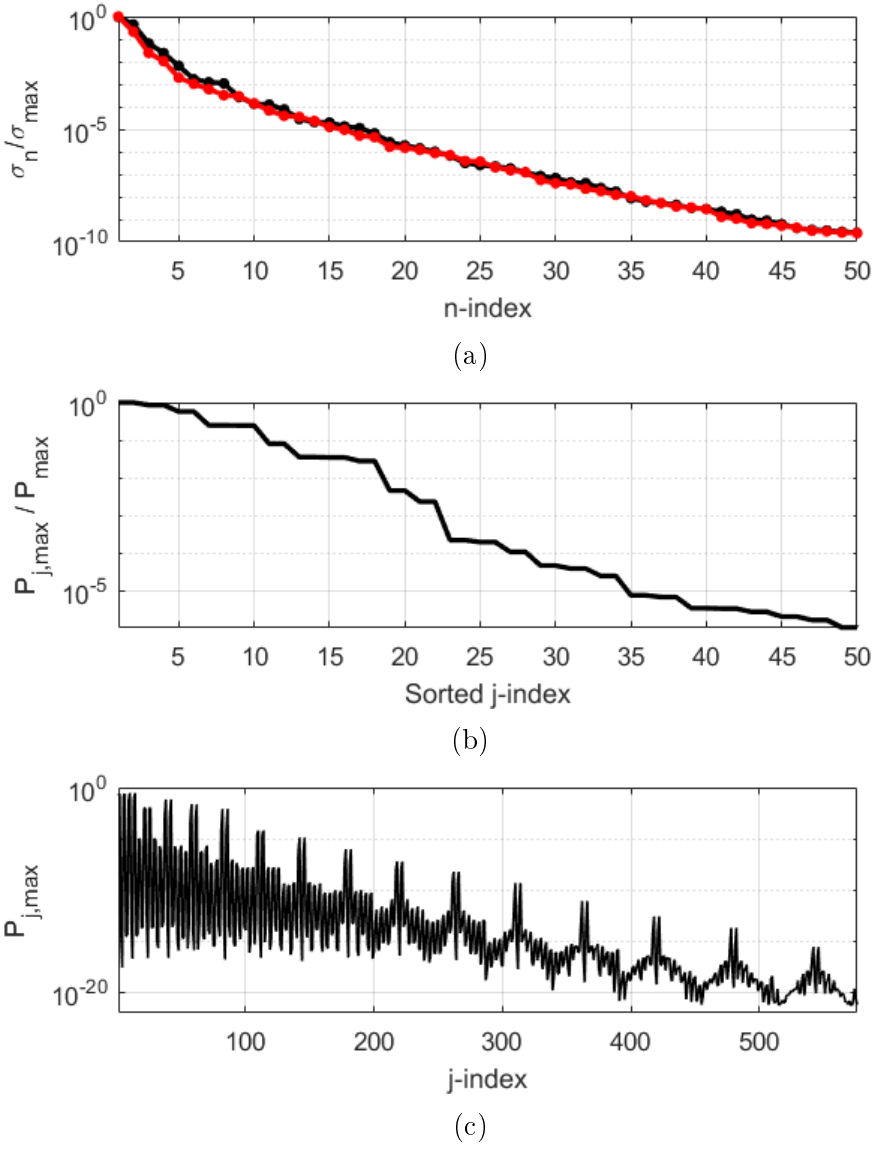

Figure 4.9: Axially corrugated horn basis function dominance for $N_s = 100$: a) $\frac{\sigma_n}{\sigma_{max}}$, b) Power-sorted $\frac{P_{j,max}}{P_{max}}$, and b) $P_{j,max}$. For a): (—) θ-component, (—) ϕ-component.

many) basis functions significantly contribute to the reconstructed far-fields. It can be seen that σ_n rapidly declines for increasing n, with only 6 CBFPs per field component having normalised singular values above 10^{-3}. The sorted and normalised SWE $P_{j,max}$ terms, on the other hand, decrease in magnitude at a significantly slower rate, suggesting that more spherical modes (and interpolants) are required to create accurate far-field reconstructions across the parameter space.

Considering that the modelled Γ response is used to train the model and obtain new adaptively sampled points, it should be verified that the CBFP

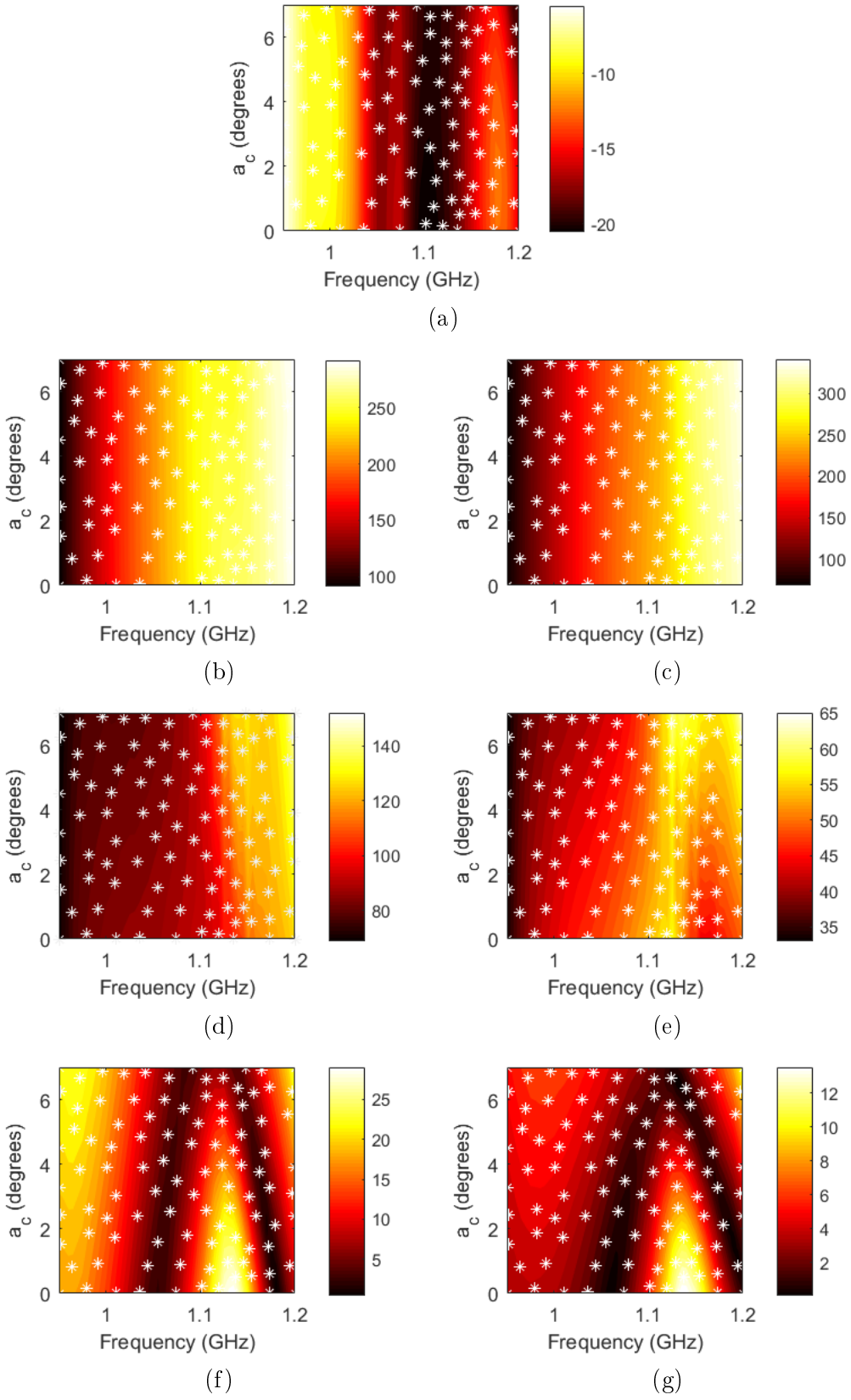

Figure 4.10: Axially corrugated horn response surface contour plots: a) $|\Gamma|$ in dB, b) $|w_{\theta,1}|$, c) $|w_{\phi,1}|$, d) $|w_{\theta,2}|$, e) $|w_{\phi,2}|$, f) $|w_{\theta,3}|$, g) $|w_{\phi,3}|$. White stars mark sample points.

coefficient response surfaces vary similarly — note that the aim of this is to determine whether the sample set, obtained from adaptive sampling trained solely on Γ, is also suitable support for the CBFP coefficient models, which are used to model the antenna far-fields. Figure 4.10 shows the modelled response surface magnitudes for $|\Gamma|$ as well as the first 3 CBFP coefficients; it is evident that all of the plotted coefficients vary smoothly enough such that the sample set obtained from adaptively sampling Γ provides sufficient support.

4.4.1.2 Aperture-Coupled Patch

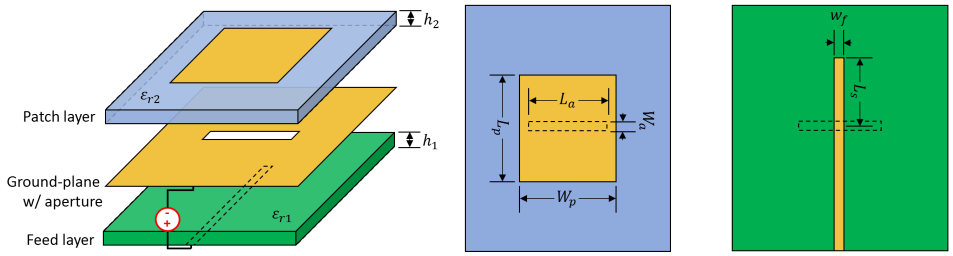

Figure 4.11: Aperture coupled patch geometry, with the discrete wire feed port marked in red.

Figure 4.11 shows the geometry of the second isolated antenna example — an aperture-coupled patch antenna designed for operation around a centre frequency of 2 GHz. A rectangular patch of length L_p and width W_p is fed through a rectangular aperture with length L_a and width W_a in the ground plane, located beneath the patch centre, which couples through to a feed line of width W_f on the opposite side of the ground plane. The feed line and radiating patch are thus separated, allowing the feed to be placed on a thin substrate of height h_1 with a high dielectric constant ε_{r1} to prevent unwanted feed-line radiation, while the patch is placed on a thick substrate of height h_2 with lower dielectric constant ε_{r2} to promote radiation at the patch edges. The aperture coupling also provides a wider impedance matching bandwidth than a pin or edge-fed patch, with the feed terminated in an open-circuit stub whose length L_s can be varied to adjust the input reactance.

In this example, a six-dimensional parameter space is considered, consisting of $x_1 = W_a \in [1.2, 1.8]$ mm, $x_2 = L_a \in [35, 46.5]$ mm, $x_3 = L_s \in [6, 8]$ mm, $x_4 = L_p \in [50, 60]$ mm, $x_5 = W_p \in [65, 80]$ mm, and $x_6 = f \in [0.95, 1.2]$ GHz. The remaining design parameters are fixed as $h_1 = 1.5$ mm, $h_2 = 12$ mm, $\varepsilon_{r1} = 4.3$, $\varepsilon_{r2} = 1$, and $W_f = 3$ mm. The modelling process is started with a latin hypercube initial design of 75 points, as in [74], and allowed to iteratively progress until $N_s = 625$. As can be seen in Figure 4.12, the ϵ_{mean} error for Γ steadily decreases until it is 1.71×10^{-2} at $N_s = 625$.

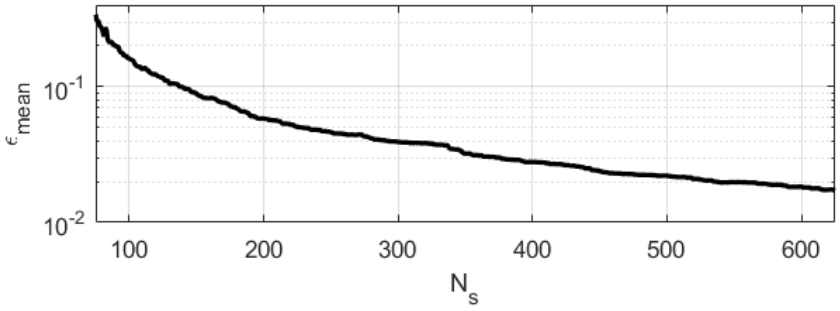

Figure 4.12: Aperture coupled patch ϵ_{mean} score for the Γ model.

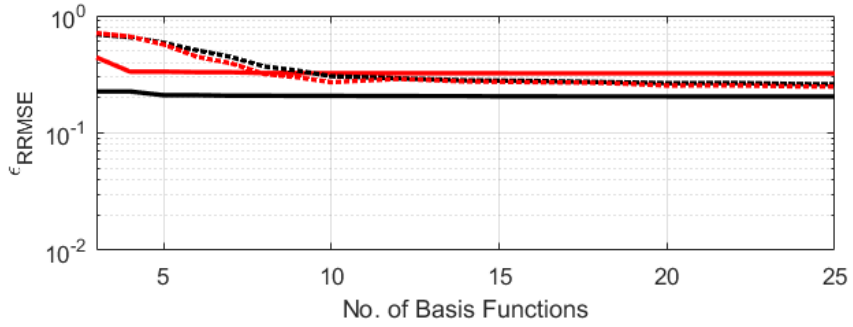

(a)

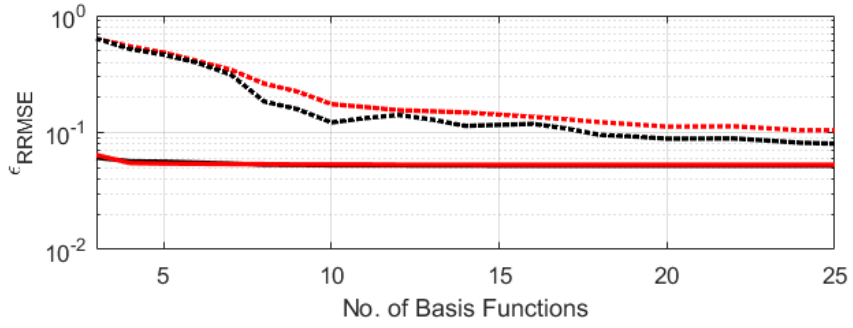

(b)

Figure 4.13: Aperture-coupled patch far-field model error scores — a) ϵ_{RRMSE} ($N_s = 139$), and b) ϵ_{RRMSE} ($N_s = 625$). For both plots: (—) CBFP E_θ, (—) CBFP E_ϕ, (·····) SWE E_θ, (·····) SWE E_ϕ.

Figure 4.13 shows ϵ_{RRMSE} for both field components, using SWE and CBFP. The errors are considered at $N_s = 139$ where the Γ model's ϵ_{mean} score first drops below 10^{-1}, and at the maximum $N_s = 625$. At $N_s = 139$, the CBFP field error converges at around 5 basis functions per field component while SWE requires 10 total basis functions and with minimum error different to those of the CBFP far-field components. The ϵ_{RRMSE} scores for both methods are above 10^{-1} for both decomposition techniques here, showing poor overall modelling ability for so few high-fidelity samples.

A significantly improved CBFP ϵ_{RRMSE} is observed for $N_s = 625$, however, and is clearly superior to SWE in terms of the converged error scores and the total number of basis functions required for convergence.

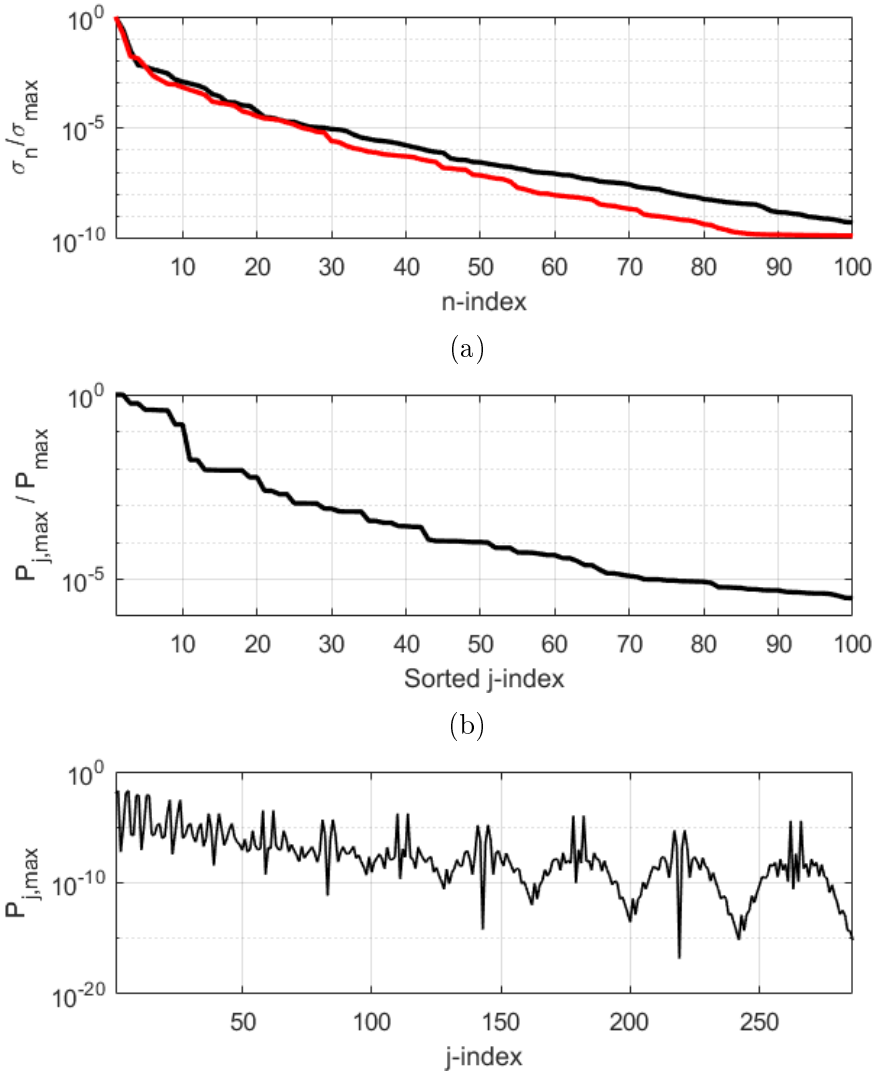

Figure 4.14: Aperture coupled patch basis function dominance for $N_s = 625$: a) $\frac{\sigma_n}{\sigma_{max}}$, b) Power-sorted $\frac{P_{j,max}}{P_{max}}$, and b) $P_{j,max}$. For a): (—) θ-component, (—) ϕ-component.

The normalised CBFP singular values and SWE $P_{j,max}$ terms for $N_s = 625$ are plotted in Figure 4.14, with $P_{j,max}$ shown both in its natural j-indexing order and sorted in descending order of magnitude. For this example, 10 CBFPs per field component have normalised singular values above 10^{-3}, indicating a more complex far-field pattern variation across the parameter space than

for the axially corrugated horn — this is expected, given the global coverage of a six-dimensional parameter space for this problem. Most of the power in the SWE Q-coefficients are seen to occur for lower j-indices, with about 10 coefficients being within 10 percent of P_{max}.

4.4.1.3 Discussion of Results

For the isolated antenna examples considered in this chapter, consistent effects can be observed that suggest general properties of the SWE and CBFP. Firstly, the far-field modelling errors of the two isolated antenna examples show that both the SWE and CBFP models converge towards some minimum far-field modelling error; for both examples, the CBFP holds a minimum error equal to or lower than SWE, putting the former forth as the preferred far-field modelling technique. Both of the antennas analysed here can be considered to be electrically large structures (including the feed-line, ground plane and substrate for the aperture-coupled patch), whose radiation characteristics are not easily captured by just a few SWE modal functions, and it is for this reason that the CBFP is understood to have an advantage, with a more versatile and problem-specific set of basis functions that are suited to the antenna problem at hand.

It is not particularly surprising that there exists a minimum model error for either SWE or CBFP, given that every model is built on a finite sample set that directly limits the quality of the coefficient interpolants. Furthermore, it is expected that CBFP would exhibit some minimum error when all of the CBFPs are used to reconstruct the field pattern, given that there are only as many CBFPs as there are sample points. The number of SWE basis functions, conversely, is potentially infinite and is practically only limited by numerical aspects, such as maintaining a well-conditioned $\mathbf{F}$-matrix to ensure that the system of equations does not become under-determined. Despite having access to more basis functions, the SWE ϵ_{RRMSE} score converges very closely to the CBFP converged ϵ_{RRMSE} in both examples.

Finally, it can be seen that more sample points not only lower the converged CBFP ϵ_{RRMSE} score, but also cause it to converge with fewer basis functions. SWE sees a proportional decrease in ϵ_{RRMSE}, but its convergence rate is roughly the same for different values of N_s.

4.4.2 PBC Unit Cell Antenna Elements

While the previous subsection gives some indication of the strengths and weaknesses of the SWE and CBFP methods, it still remains to be seen how these techniques perform for modelling scan- and frequency-dependent far-fields $\overrightarrow{E}_{uc-\Omega_0}(\theta, \phi)$ for antenna elements in a PBC unit cell.

To illustrate the variation of the unit cell far-fields with scan angle, Figure 4.15 shows two FEKO-simulated sets of $G_{uc-\Omega_0}$ E-plane ϕ-cuts, for two differ-

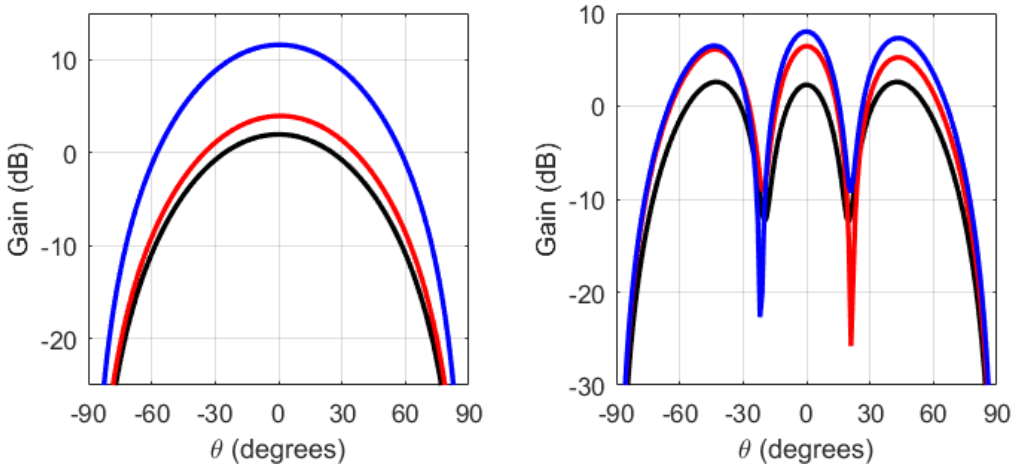

(a) (b)

Figure 4.15: E-plane ϕ-cuts of the gain patterns of various dipole elements in PBC unit cells: a) half-wave dipole ($d = \frac{\lambda}{2}$)), and b) long dipole ($d = \frac{3\lambda}{2}$)). For both plots: (—) $\Omega_0 = (0°, 0°)$, (—) $\Omega_0 = (30°, 0°)$, (—) $\Omega_0 = (60°, 0°)$.

ent dipoles (a half-wave dipole with $L = \frac{\lambda}{2}$ and a long dipole with $L = \frac{3\lambda}{2}$) in unit cells backed with an infinite ground plane and varying inter-element spacing d. While the half-wave dipole's gain patterns only change in magnitude across scan angle, the long dipole's pattern clearly varies in overall shape as well; this pattern shift across scan angle affects the value of $\overrightarrow{E}_{uc-\Omega_0}(\theta_0, \phi_0)$, which must be accurately determined in order to derive radiometric figures-of-merit. To this end, the SWE and CBFP techniques are investigated as efficient modelling techniques for the scan-dependent unit cell far-fields.

Three PBC unit cell antenna element examples are considered in this subsection: firstly, a dense-regular narrowband patch antenna array, followed by two wideband sparse-regular AA elements. These examples represent different array and element mutual coupling environments for which the SWE and CBFP methods are to be assessed. For all examples, the antennas are placed in a square array layout with inter-element spacing d. For all of the examples, a minimum sphere of $r_0 = d$ is selected to approximately capture the major electromagnetic behaviour of the array element and its closest neighbouring elements. It is to be determined through these examples whether this choice of minimum sphere is sufficient for these types of unit cell antenna elements.

4.4.2.1 Dense-Regular Patch Element

The first unit cell element example considers a pin-fed rectangular PEC patch above a PEC ground plane, as depicted in Figure 4.6. The substrate between the patch and ground plane is assumed to have a dielectric constant ε_{r1}. The antenna is parametrised by the patch length L, patch width W, substrate

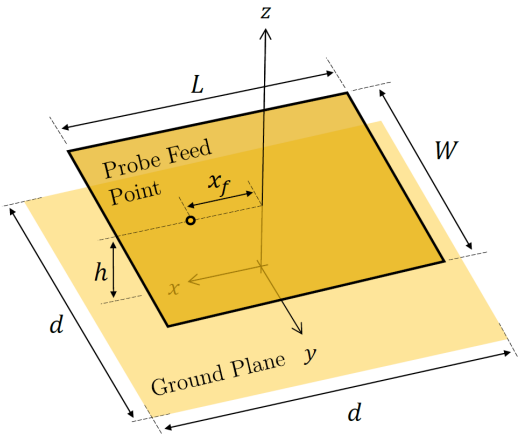

Figure 4.16: Patch antenna element in a dense-regular phased array unit cell.

height h, and feeding pin position x_f. The antenna is designed for narrowband operation at $f_0 = 1$ GHz (with λ_0 denoting the corresponding wavelength) and is simulated in FEKO PBC-MoM.

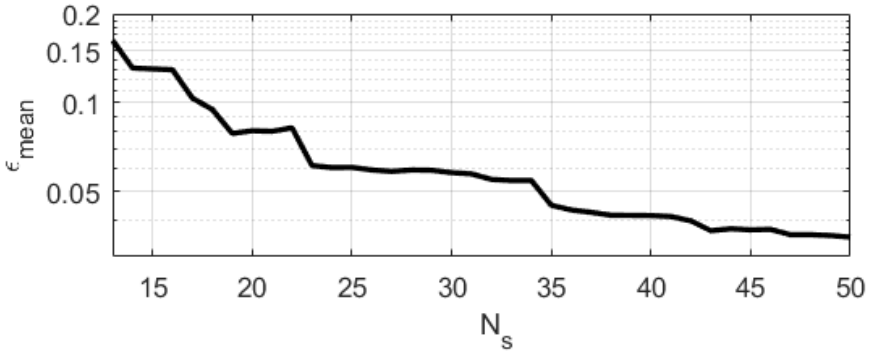

Figure 4.17: Patch unit cell ϵ_{mean} score for the Γ_{act} model.

In this example, a two-dimensional parameter space is considered, consisting of $x_1 = \theta_0 \in [0°, 85°]$ and $x_2 = \phi_0 \in [0°, 90°]$, while the remaining parameters are fixed as $L = 0.47\lambda_0$, $W = 0.9L$ mm, $h = 4$ mm, $x_f = \frac{L}{4}$ mm and $d = \frac{\lambda_0}{2}$. A dense-regular array configuration is chosen in this first unit cell example to observe a case free of grating lobes in visible space. The modelling process is started with a latin hypercube initial design of 13 points and allowed to iteratively progress until $N_s = 50$. As can be seen in Figure 4.17, the ϵ_{mean} error for Γ_{act} steadily decreases to 3.492×10^{-2} at $N_s = 50$.

Figure 4.18 shows ϵ_{RRMSE} for both field components, using SWE and CBFP. The errors are considered at $N_s = 25$ and at the maximum $N_s = 50$. For $N_s = 25$, ϵ_{RRMSE} converges around 10 basis functions per field component for CBFP, and near 30 total basis functions for SWE. Similar results are observed for $N_s = 50$, although the CBFP ϵ_{RRMSE} in this instance converges

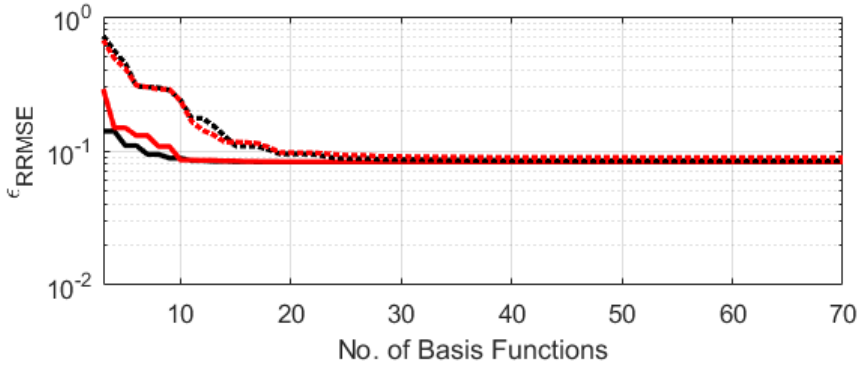

(a)

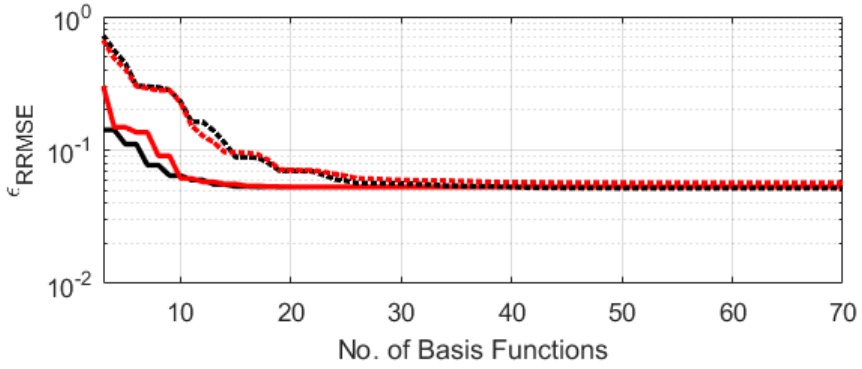

(b)

Figure 4.18: Patch unit cell Far-field model error scores — a) ϵ_{RRMSE} ($N_s = 25$), and b) ϵ_{RRMSE} ($N_s = 50$). For all plots: (—) CBFP E_θ, (—) CBFP E_ϕ, (·····) SWE E_θ, (·····) SWE E_ϕ.

at around 15 basis functions per field component whereas SWE still converges at around 30 total basis functions. It can therefore be concluded that, in this example, CBFP and SWE have close to the same level of computational efficiency in terms of model interpolants.

The normalised CBFP singular values and SWE $P_{j,max}$ terms for $N_s = 50$ are plotted in Figure 4.19, with $P_{j,max}$ shown both in its natural j-indexing order and sorted in descending order of magnitude. For this example, around 10 CBFPs per field component have normalised singular values above 10^{-3}. The radiated power of the SWE Q-coefficients is strongest for lower j-indices, decreasing steadily as the mode number increases. In this case, the ordering of the power-sorted j-indices are almost the same as that of the standard j-indices, showing the dominant spherical modes to occur well within the maximum number of modes set by the choice of minimum sphere.

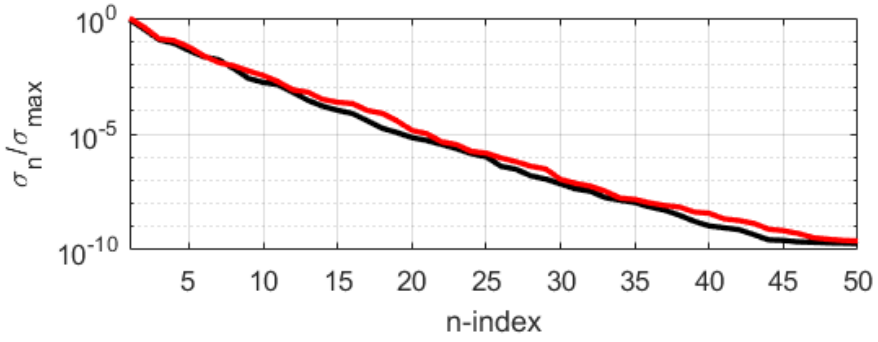

(a)

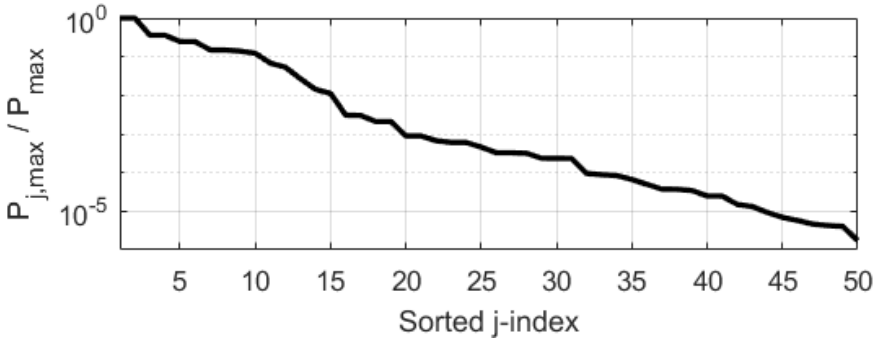

(b)

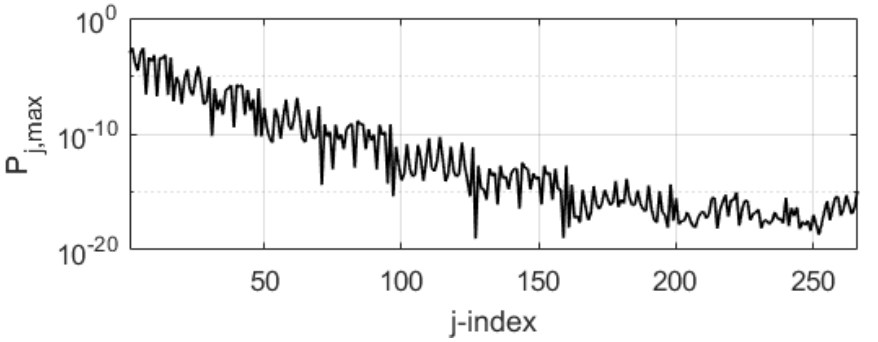

(c)

Figure 4.19: Patch unit cell basis function dominance for $N_s = 50$: a) $\frac{\sigma_n}{\sigma_{max}}$, b) Power-sorted $\frac{P_{j,max}}{P_{max}}$, and b) $P_{j,max}$. For a): (—) θ-component, (—) ϕ-component.

4.4.2.2 Sparse-Regular Dipole Element

Figure 4.20 shows a half-wave dipole element above a ground plane, in a sparse-regular PBC unit cell. The main purpose of this experiment is to gain insight on the variation of basis function coefficients across the parameter space, particularly to see whether they are similarly affected by the onset of grating lobes as the active reflection coefficient has been shown to be in Chapter 3.

The antenna is parametrised by the dipole length L and height above the

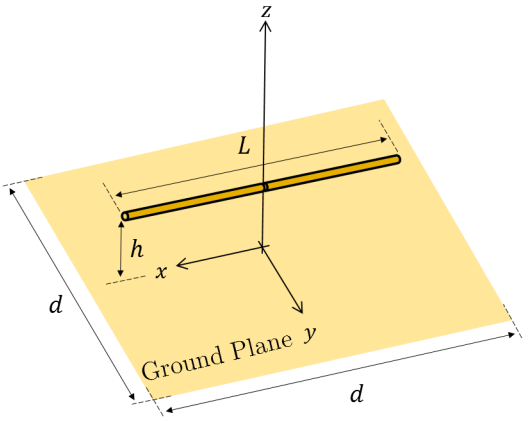

Figure 4.20: Dipole antenna element in a sparse-regular phased array unit cell.

ground plane h, designed for narrowband operation at $f_0 = 1$ GHz (with λ_0 denoting the corresponding wavelength). The dipole unit cell is simulated in FEKO PBC-MoM.

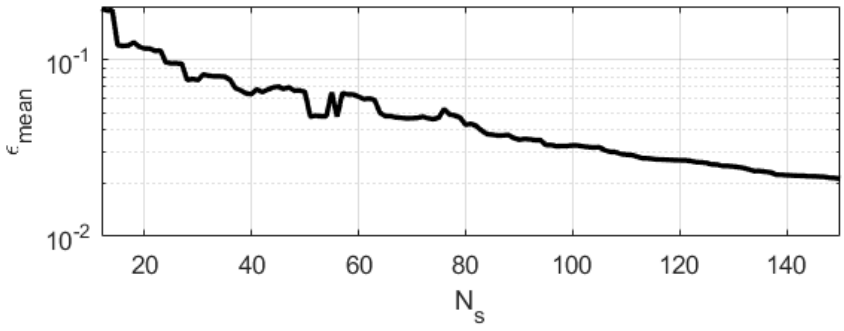

Figure 4.21: Dipole unit cell ϵ_{mean} score for the Γ_{act} model.

In this example, a two-dimensional parameter space is considered, consisting of $x_1 = \theta_0 \in [0°, 85°]$ and $x_2 = \phi_0 \in [0°, 90°]$, while the remaining parameters are fixed to those of the first dipole experiment in Chapter 3. The modelling process is started with a latin hypercube initial design of 12 points and allowed to iteratively progress until $N_s = 150$. As can be seen in Figure 4.21, the ϵ_{mean} error for Γ_{act} steadily decreases until it is 2.12×10^{-2} at $N_s = 150$.

Figure 4.22 shows ϵ_{RRMSE} for both field components, using SWE and CBFP. The errors are considered at $N_s = 60$ (where ϵ_{mean} is roughly half of its value at the initial $N_s = 12$), and at the maximum $N_s = 150$. Both SWE and CBFP converge to similar scores in both cases, a trait consistent with every other example considered in this chapter. The improvement in the converged error seen between $N_s = 60$ and $N_s = 150$ indicates that the far-field model improves proportionally to the Γ_{act} model.

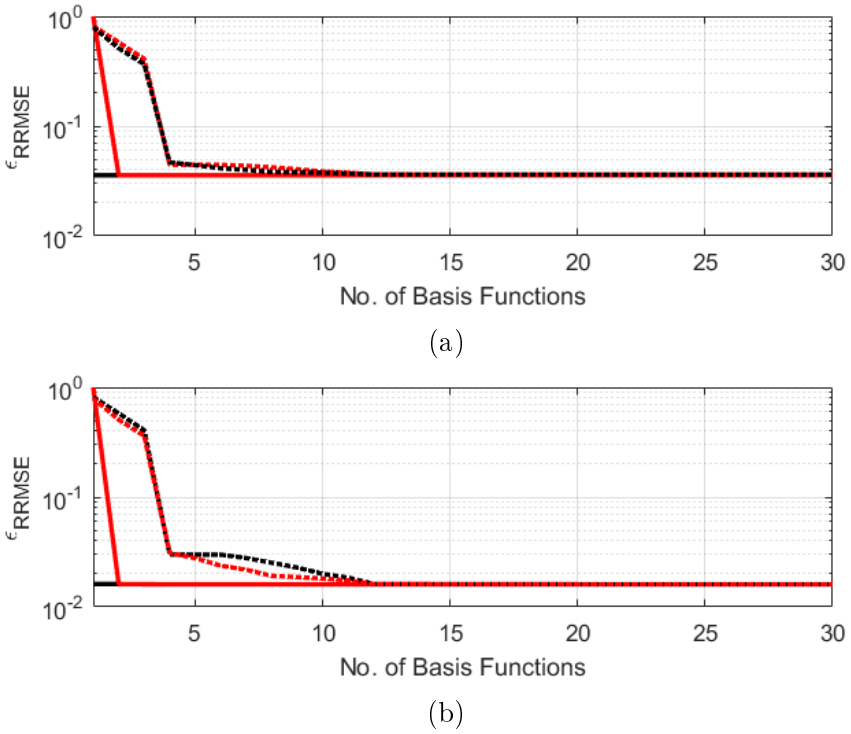

Figure 4.22: Dipole unit cell far-field model error scores — a) ϵ_{RRMSE} ($N_s = 60$), and b) ϵ_{RRMSE} ($N_s = 150$). For all plots: (—) CBFP E_θ, (—) CBFP E_ϕ, (·····) SWE E_θ, (·····) SWE E_ϕ.

For both cases of N_s, the CBFP ϵ_{RRMSE} score converges for both field-components with only 2 basis functions, suggesting that the unit cell far-field has mostly the same shape across the scanning space. This is expected for a half-wave dipole, as indicated by Figure 4.15. SWE, however, requires more than 10 basis functions to converge to the same minimum error. A distinct advantage in the CBFP is thus observed for this type of modelling problem.

The normalised CBFP singular values and SWE $P_{j,max}$ terms for $N_s = 150$ are plotted in Figure 4.23, with $P_{j,max}$ shown both in its natural j-indexing order and sorted in descending order of magnitude. A particularly rapid decrease in the normalised singular values is seen for increasing n, which is consistent with the ϵ_{RRMSE} convergence at only 2 basis functions. The SWE's ranked and normalised $P_{j,max}$ terms show that a near-constant power distribution occurs in the 4 most dominant spherical modes, followed by another near-constant power range for the next 6 modes that allow the SWE far-field reconstruction to converge to the same ϵ_{RRMSE} as the CBFP method. While the dominant spherical modes are clearly limited to the lowest j-indices, the fact that several are required for accurate far-field reconstruction makes the SWE computationally inefficient here in comparison to CBFP.

Figure 4.24 shows the modelled response surface magnitudes for $|\Gamma_{act}|$ as well as the first 3 CBFP coefficients. As with the axially corrugated horn ex-

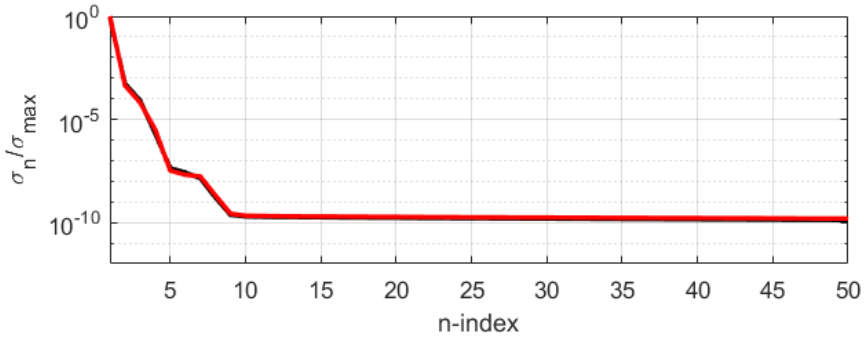

(a)

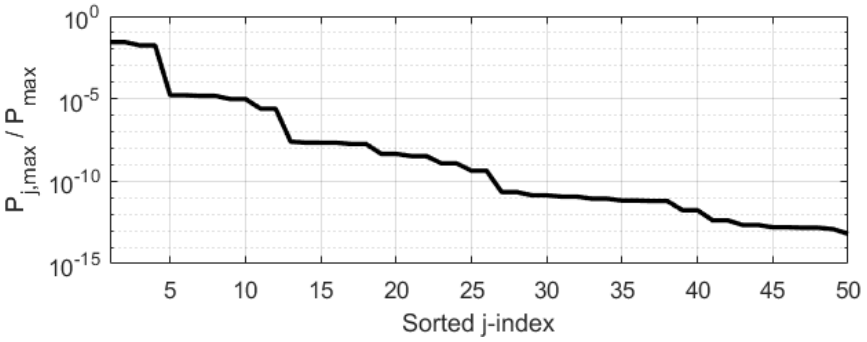

(b)

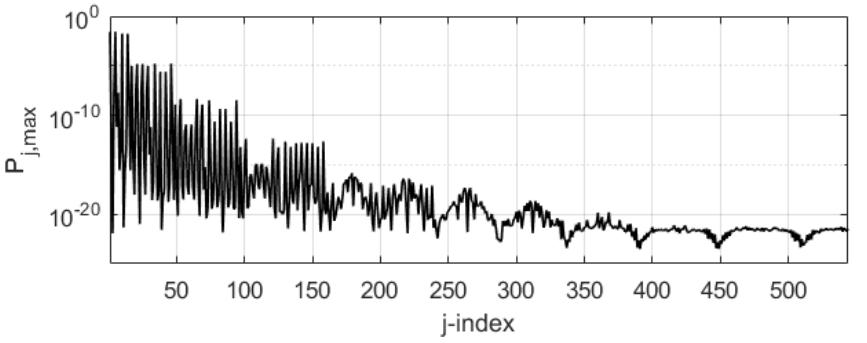

(c)

Figure 4.23: Dipole unit cell basis function dominance for $N_s = 150$: a) $\frac{\sigma_n}{\sigma_{max}}$, b) Power-sorted $\frac{P_{j,max}}{P_{max}}$, and b) $P_{j,max}$. For a): (—) θ-component, (—) ϕ-component.

ample, the first CBFP coefficient varies in the broadest and smoothest manner, while the others vary more rapidly. It can also be seen that the coefficients vary almost identically between the $\theta-$ and $\phi-$components, except for a difference in magnitude. The first two CBFP coefficient surfaces are considerably smoother than $|\Gamma_{act}|$ and thereby easier to interpolate, and although the distribution of high-fidelity samples is not optimally placed for either of their response surfaces, there are enough points selected by the Γ_{act}-driven adaptive

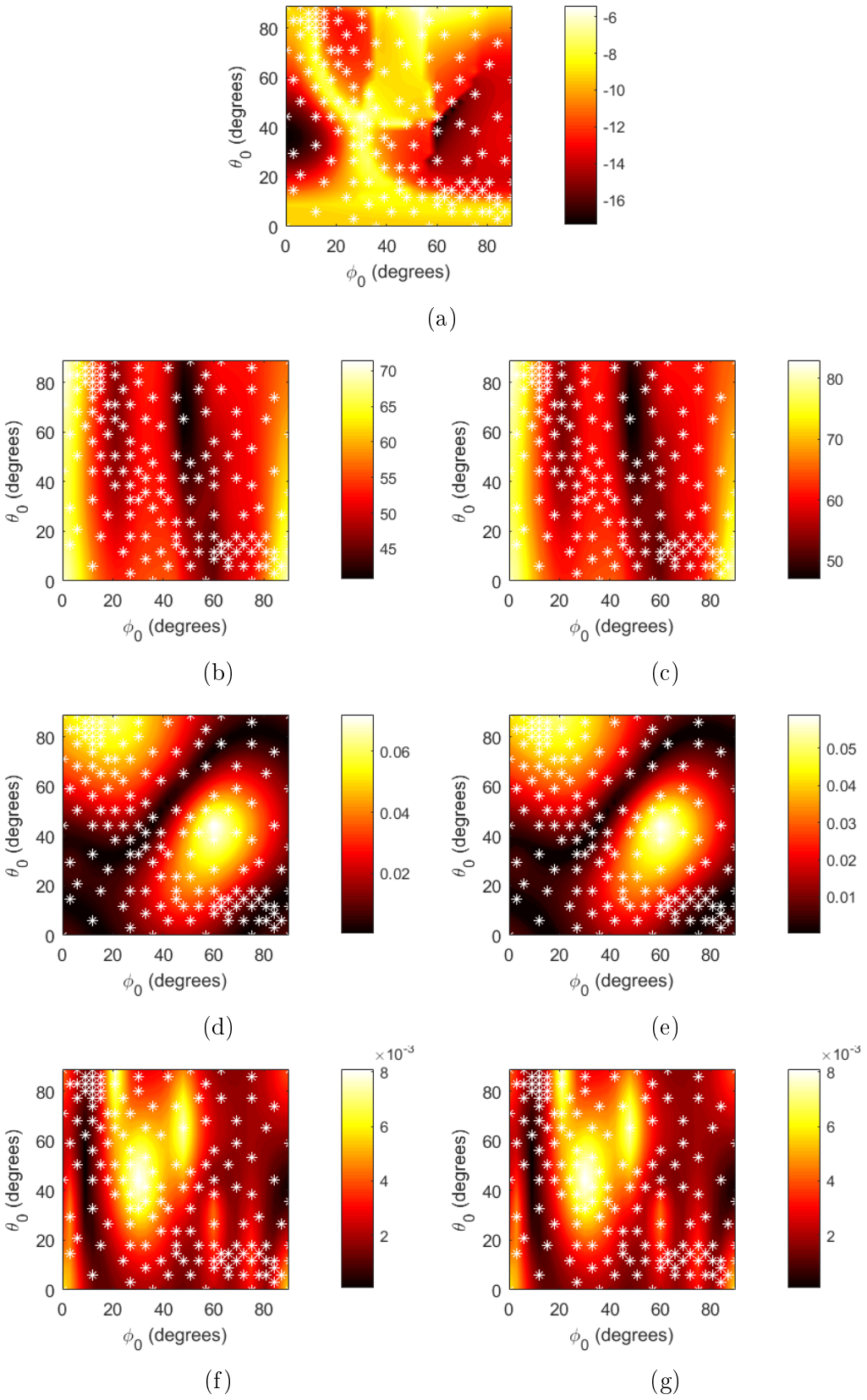

Figure 4.24: Dipole unit cell response surface contour plots: a) $|\Gamma_{act}|$ in dB, b) $|w_{\theta,1}|$, c) $|w_{\phi,1}|$, d) $|w_{\theta,2}|$, e) $|w_{\phi,2}|$, f) $|w_{\theta,3}|$, g) $|w_{\phi,3}|$. White stars mark sample points.

sampler to provide adequate interpolation support for the smoothly varying surfaces.

4.4.2.3 Sparse-Regular BLU Element

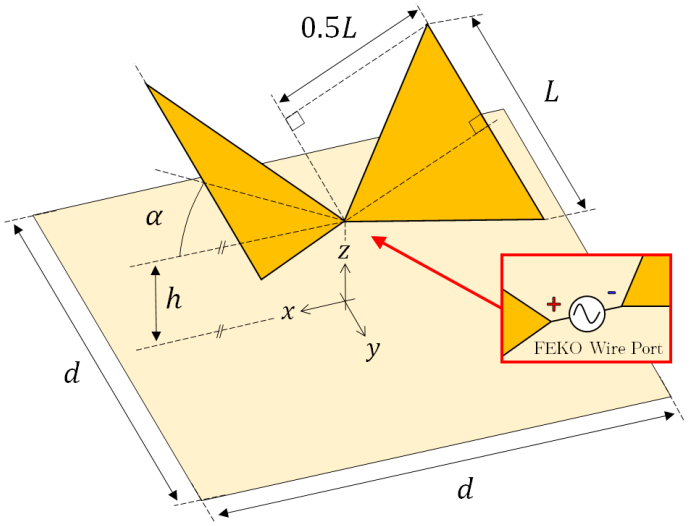

Figure 4.25: BLU antenna element in a sparse-regular phased array unit cell.

The second unit cell element example considers the BLU element analysed in Chapters 2 and 3, as depicted in Figure 4.25. The element is simulated in CST MWS with a PBC bounding box and an infinite ground plane.

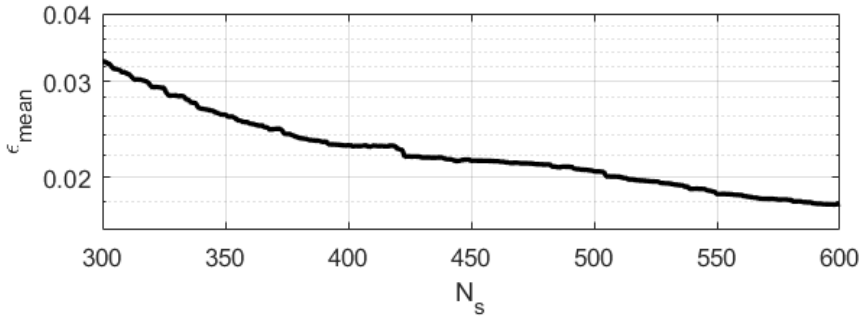

Figure 4.26: BLU unit cell ϵ_{mean} score for the Γ_{act} model.

In this example, a three-dimensional parameter space is considered, consisting of $x_1 = \theta_0 \in [0°, 60°]$, $x_2 = \phi_0 \in [0°, 90°]$ and $x_3 = f \in [100, 450]$ MHz, with the element geometry identical to the BLU element analysed in Chapter 3. The modelling process is started with Chapter 3's S_3 initial design of 300 points, and allowed to iteratively progress until $N_s = 600$. As can be seen

in Figure 4.26, the ϵ_{mean} error for Γ_{act} steadily decreases to 1.787×10^{-2} at $N_s = 600$.

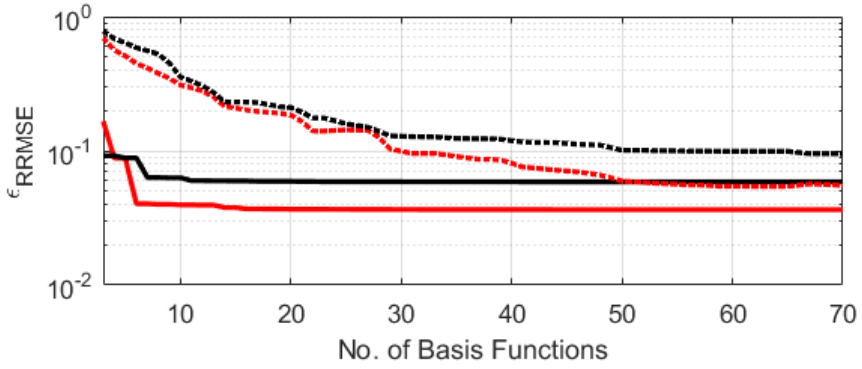

(a)

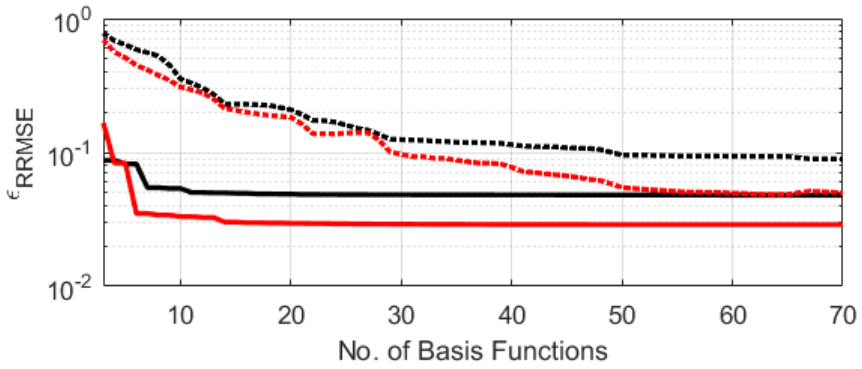

(b)

Figure 4.27: BLU element far-field model error scores — a) ϵ_{RRMSE} ($N_s = 300$), and b) ϵ_{RRMSE} ($N_s = 600$). For both plots: (—) CBFP E_θ, (—) CBFP E_ϕ, (·····) SWE E_θ, (·····) SWE E_ϕ.

Figure 4.27 shows ϵ_{RRMSE} for both field components, using CBFP. The errors are considered at $N_s = 300$, when the initial design is built, and at the maximum $N_s = 600$. For $N_s = 300$, ϵ_{RRMSE} converges around 5 basis functions per field component for CBFP, and near 50 basis functions for SWE. Similar convergence rates are observed for ϵ_{max}, with SWE only converging near 70 basis functions. The CBFP ϵ_{RRMSE} and ϵ_{max} scores are seen to converge at significantly lower scores than for SWE. The same general behaviour is also seen for $N_s = 600$.

The normalised CBFP singular values and SWE $P_{j,max}$ terms for $N_s = 600$ are plotted in Figure 4.28, with $P_{j,max}$ shown both in its natural j-indexing order and sorted in descending order of magnitude. In this case, 34 θ-CBFPs and 22 ϕ-CBFPs have normalised singular values above 10^{-3}. SWE, however, has $P_{j,max} > 10^{-2}$ for over 250 basis functions, and while the highest values are

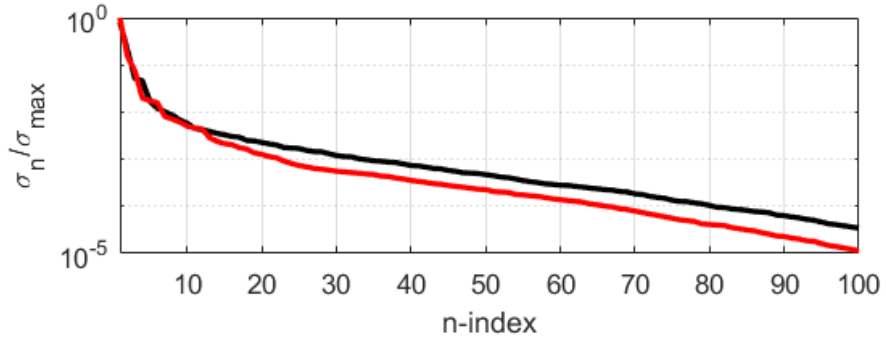

(a)

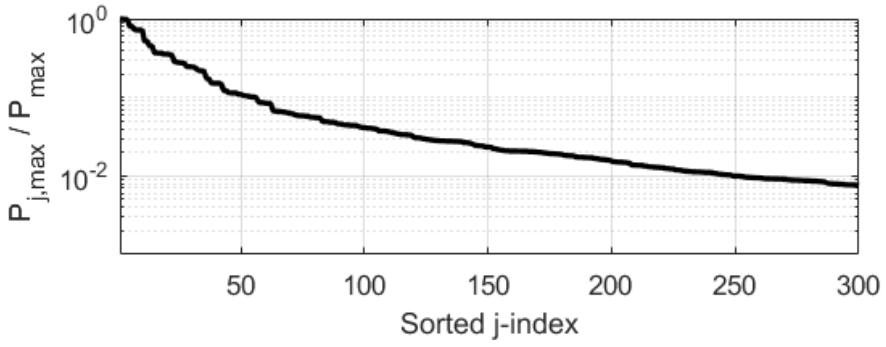

(b)

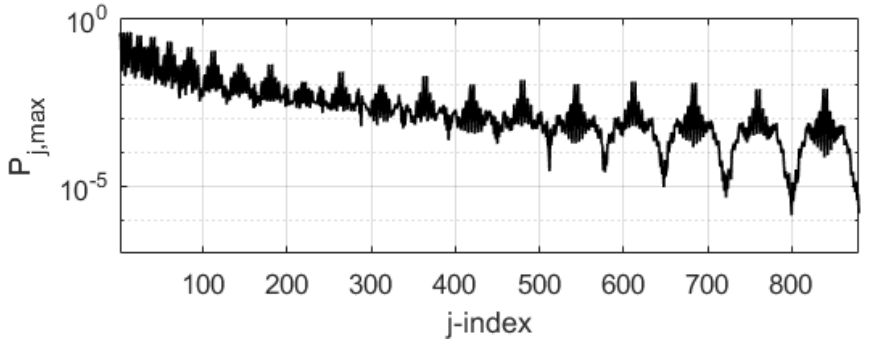

(c)

Figure 4.28: BLU unit cell basis function dominance for $N_s = 600$: a) $\frac{\sigma_n}{\sigma_{max}}$, b) Power-sorted $\frac{P_{j,max}}{P_{max}}$, and b) $P_{j,max}$. For a): (—) θ-component, (—) ϕ-component.

seen for low j-indices, it is still clear that the total radiated power is spread across many distinct spherical modes and therefore requires many interpolants for accurate far-field reconstruction. Note that the dominance of the lower-order modes, with consistent decrease in $P_{j,max}$ with increasing j shows that the choice of SWE minimum sphere is more than adequate to accommodate for the modelling problem at hand.

For both sampling sets considered, CBFP clearly performs best of the two

decomposition methods. This is attributed, again, to the fact that the SWE's modal functions are not as readily adapted to the scanning variation of the BLU unit cell as the CBFPs, especially at the higher frequency ranges where the antenna appears electrically large.

4.4.2.4 Discussion of Results

It can be seen from the unit cell examples that the CBFP method does not behave much differently than for isolated antenna elements. The ability of the CBFPs to sample far-field basis functions from the design space gives it a clear advantage in the sparse-regular examples, where the SWE requires numerous modal functions to capture the same pattern behaviour. For the sparse-regular examples, the CBFP provides a far-field modelling error equal to or better than the SWE with one-third or fewer coefficients and interpolants — furthermore, CBFP is significantly more effective than SWE for the electrically large broadband BLU element, supporting the conclusions drawn in the discussion of the isolated antenna element examples. In light of the results put forth by these examples, The CBFP method is recommended to efficiently model the far-fields of sparse-regular AA unit cell elements.

It can also be seen in each example that ϵ_{RRMSE} decreases as N_s increases as the far-field models improve in unison with the impedance response model. Should the designer require the magnitude of ϵ_{RRMSE} to be lower, more high-fidelity samples can be added with the adaptive sampling techniques of Chapter 3 to simultaneously reduce the impedance and radiation response model error.

4.5 Conclusion

In this chapter, two contemporary orthogonal basis decomposition techniques were investigated for use in the global surrogate modelling of AA unit cell far-field responses. A parallel approach was adopted to construct the basis function coefficient models from samples obtained in the adaptive sampling of the element impedance response, allowing these models to be easily integrated with the Γ_{act} modelling process detailed in Chapter 3. Altogether, the complete impedance and radiation behaviour can be approximately obtained across a full three-dimensional parameter space of scan angle and frequency in an efficient manner, giving insight into the full operational behaviour of AA antenna elements.

The main contribution of this chapter was the first formal comparison of the SWE and CBFP techniques for parametrised antenna modelling, as well as the extension of the modelling framework from Chapter 3 to include models for the unit cell far-fields of sparse-regular AA elements. Part of the content of Section 4.4.2 was published in the proceedings of the 2018 Asia-Pacific Microwave Conference (APMC) [30].

The following chapter focuses on obtaining efficient models of radiometric figures-of-merit for antenna elements in sparse-regular AAs, focusing on the analysis of elements for SKA Mid-Frequency Aperture Array.

Chapter 5

Optimisation-driven Modelling for Radiometric Figures-of-Merit

For broadband antenna elements in sparse-regular aperture arrays, antenna element design is an important task with multiple challenges arising from the environment of the sparse-regular AA regime. Stringent goals are stipulated by the key requirements of MFAA [33], necessitating careful design and optimisation of a suitable antenna element across a wide frequency bandwidth and scanning range. Chapters 3 and 4 have provided several sparse-regular AA element examples in which response degradation can occur at scan angles outside of the principal antenna E- and H-planes, requiring characterisation of the responses across the full space of operating parameters.

The techniques explored in Chapters 3 and 4 have been focused towards generating accurate models of sparse-regular AA element responses, for the purposes of analysis and to gain insight into how effectively the attainment of these response surfaces may be expedited by use of global surrogate models. However, in a full element optimisation procedure, the focus is not primarily on accurate global modelling but obtaining a scalar figure-of-merit that concisely quantifies the antenna's performance over its operating parameters. In this chapter, the techniques and observations of the previous chapters are now considered altogether to synthesise *optimisation-driven* global models for the receiving sensitivity of sparse-regular AA elements, which may then be used in a suitable objective function to assess the performance of a given element design in a larger optimisation loop. Particular attention is paid to the design of a sparse-regular AA element for the SKA Mid-Frequency Aperture Array (MFAA), which is used as the primary modelling study in this chapter.

Section 5.1 discusses sparse-regular AA antenna elements for MFAA, and explores the pyramidal sinuous antenna design as a possible candidate element. Section 5.2 investigates the construction of global models for the pyramidal sinuous AA element using the techniques developed in the previous two chapters, with the intent of attaining accurate impedance and radiation response models from which radiometric figures-of-merit may be derived. Section 5.3 proposes

Table 5.1: Key MFAA System Requirements.

Feature	Requirement	Unit	Notes
Frequency Range	450 - 1450	MHz	-
Instantaneous Sensitivity	$\geq 10^4$	m^2/K	At zenith, per polarisation
Optical FoV	≥ 200	$deg.^2$	At 1 GHz
Scan Angle	≥ 45	deg.	From zenith
Imaging Dynamic Range	≥ 70	dB	After calibration
Polarisation Capability	Full Stokes	-	-
Polarisation Purity	-40/-25	dB	On-/Off-axis

an alternate, expedited modelling method for assessing sparse-regular AA element performance and the design of a suitable objective function to complement the model. Section 5.4 provides a discussion of the overall results of the modelling techniques considered in this chapter, and Section 5.5 concludes.

5.1 Sparse-regular AAs for Mid-Frequency Aperture Array

In this section, AA elements for MFAA are considered in the sparse-regular array regime. A sparse-regular AA concept has not hitherto been proposed for MFAA, and thus no antenna elements have yet been designed for this particular type of AA.

Table 5.1 shows a number of key requirements for MFAA, including specifications for the receiving sensitivity and polarisation purity [33]. These requirements are stated for the responses of an entire aperture array, for which terms such as receiving sensitivity may be found from the unit cell element responses [43]. Besides these requirements, [33] goes further to stipulate that *sensitivity degradation away from zenith will remain within 5 percent of the theoretical performance loss of the system due to the changing geometric foreshortening of the aperture*. This requires a broad element beam pattern and low receiver noise temperature at all scan angles.

The sparse-regular array environment consists of a regularly spaced (grid lattice) array layout, with an inter-element spacing d that is seen at most or all operating frequencies to be greater than half of the wavelength λ. Antenna elements for this array configuration ideally exhibit minimal mutual coupling [24] and therefore cannot be connnected, necessitating large physical dimensions to support broadband operation. For the sparse-regular MFAA elements in

Table 5.2: Sparse-regular Vivaldi element geometric parameters.

Parameter	Value
h_f	33 mm
h_c	42 mm
L_f	63 mm
L_s	1.2 mm
w_s	0.4 mm
d_c	12 mm
Taper factor	5

this chapter, it is henceforth assumed that $d = \lambda$ at $f = 450$ MHz in order to accommodate the size of the elements under consideration. It should be noted that for this choice of d, grating lobes are present in visible space at all operating frequencies.

In the following subsections, two different antenna elements are investigated for use in a sparse-regular MFAA aperture array. The antenna responses in this section are all obtained from frequency-domain EM simulations of the antenna in transmit mode and with PBC, in CST Microwave Studio.

5.1.1 Vivaldi Element

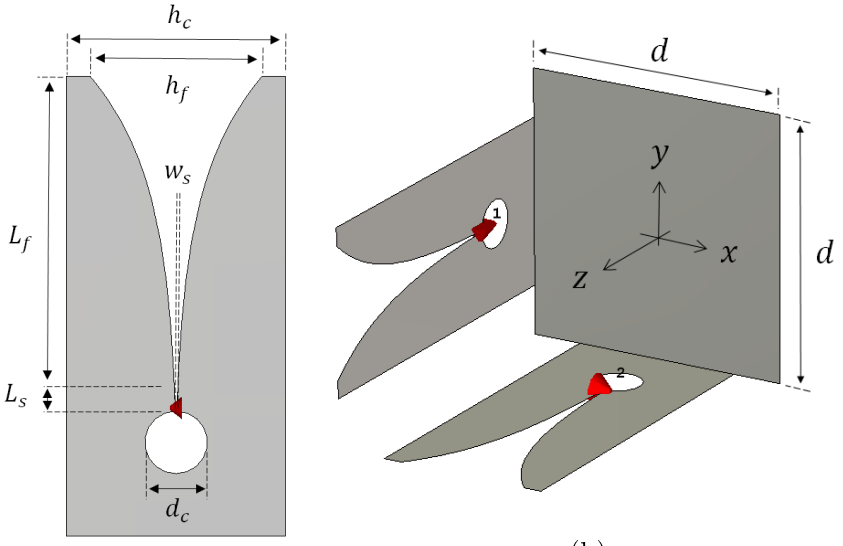

Figure 5.1: Geometry of the Vivaldi element above a ground plane: a) element profile, and b) element in an AA unit cell.

Table 5.3: Sparse-regular pyramidal sinuous element geometric parameters.

Parameter	Value
α	24.85°
δ	14.95°
τ	0.842
h	22.2 mm
θ_{pyr}	56.48°

Figure 5.1 shows the geometry and unit cell configuration of dual-linearly polarised Vivaldi elements over an infinite PEC ground plane, designed for operation in the 450–1450 MHz frequency range. The antenna geometric parameters, as annotated on the figure, are summarised in Table 5.2. The elements are fed with 150 Ω discrete ports. The Vivaldi element has seen successful use in several aperture array concepts [18,91], and is thus considered as a natural first option to explore.

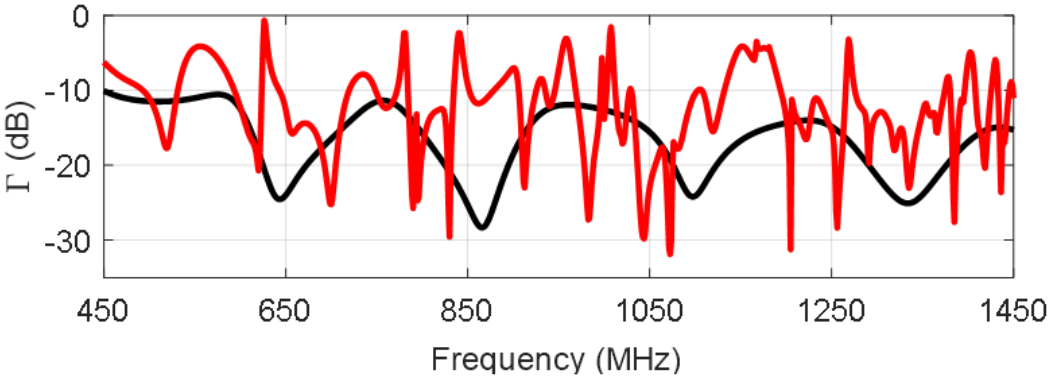

Figure 5.2: Vivaldi element reflection coefficients: — isolated element Γ, and — PBC Port 1 Γ_{act} for $\Omega_0 = (0°, \phi)$. Note that Γ_{act} at Port 2 is identical to that of Port 1.

From Figure 5.2, it is seen that the element reflection coefficient is well-matched in isolation but seriously degraded when placed in the infinite array environment. It is clear that the Vivaldi element considered here is highly susceptible to mutual coupling in this array environment, and cannot be used as an MFAA sparse-regular element. Similar results have also been reported for an LPDA element in a sparse-regular AA layout [92].

5.1.2 Pyramidal Sinuous Element

The pyramidal sinuous antenna, shown in Figure 5.3, is also proposed here as a sparse-regular AA element. The antenna consists of four planar sinuous arms projected onto a pyramidal surface and suspended a height h above

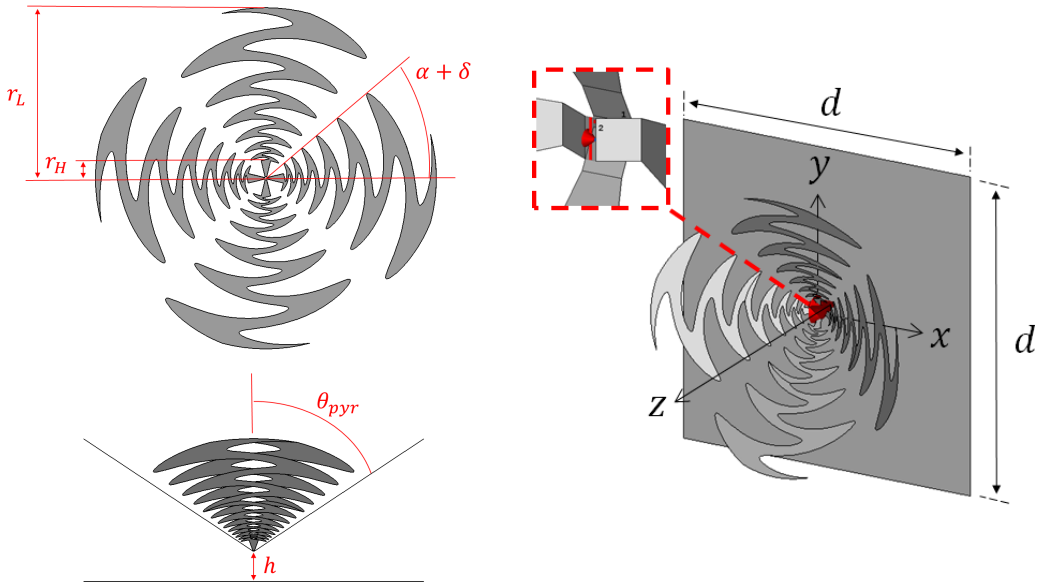

(a) (b)

Figure 5.3: Geometry of the pyramidal sinuous element above a ground plane: a) orthographic views, and b) element in an AA unit cell.

a ground plane to enhance the bandwidth and radiation characteristics of standard planar sinuous antenna. The particular element considered here has exactly the same geometry and parametrisation as that of the sinuous element in [93] over an infinite ground plane, scaled to operate in the MFAA frequency band and differentially fed across the opposite arms with 300 Ω discrete ports for dual linear polarisation. The antenna element's geometric parameters are summarised in Table 5.3.

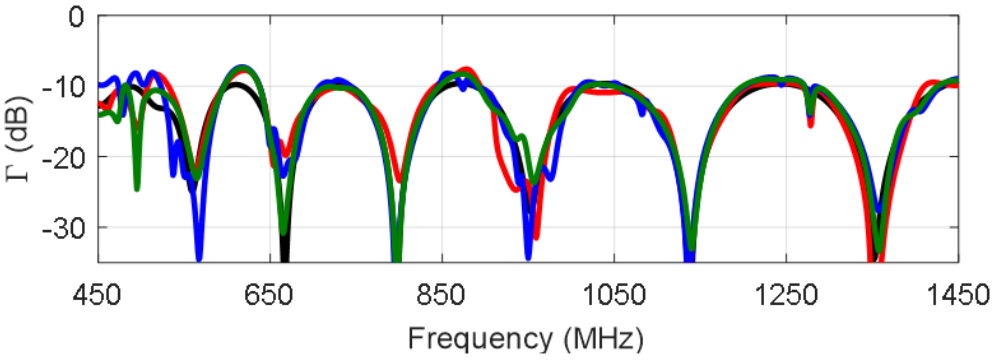

Figure 5.4: Pyramidal sinuous element reflection coefficients: — Port 1 isolated Γ, — PBC Port 1 Γ_{act} for $\Omega_0 = (0°, \phi)$, — PBC Port 1 Γ_{act} for $\Omega_0 = (45°, 0°)$, and — PBC Port 1 Γ_{act} for $\Omega_0 = (45°, 90°)$. Note that Γ_{act} at Port 2 is identical to that of Port 1.

Figure 5.4 shows the isolated reflection coefficient Γ as well as the PBC active reflection coefficient Γ_{act} when $\Omega_0 = (0°, \phi)$. While Γ_{act} is somewhat altered by mutual coupling at certain frequencies, it is largely unchanged and suggests that the element's impedance properties are resilient to the sparse-regular AA regime. Similar results are seen at three distinct scan angles, further indicating the element's impedance stability over scan angle and frequency. A full optimisation of the antenna geometry is still to be performed for this element design in future work, in which Γ_{act} should be minimised across the range of operating parameters, but this first iteration of the design still demonstrates desirable response qualities that warrant its further investigation as a sparse-regular AA candidate element.

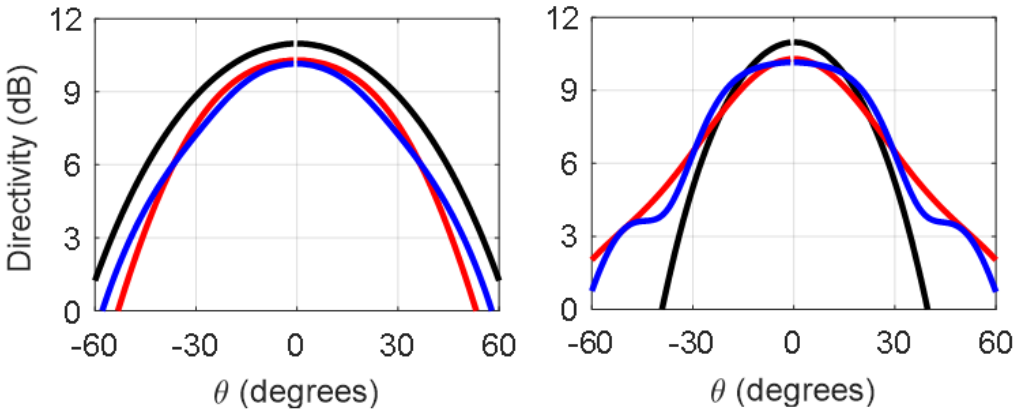

Figure 5.5: Directivity cuts for the isolated pyramidal sinuous element at $\phi = 0°$ (left) and $\phi = 90°$ (right), when stimulated at Port 1. For both plots, - - - $f = 450$ MHz, — $f = 950$ MHz, and — $f = 1450$ MHz.

The pyramidal sinuous element's isolated far-field directivity patterns are plotted in Figure 5.5, which are reasonably constant in amplitude across frequency. The patterns' half-power beamwidths (HPBW) are, however, narrower than desired for MFAA's wide scanning requirements, and broadening of the patterns should be a design goal during future geometric optimisation of the element.

5.1.3 Scan Responses

In this subsection, the scan performance of the pyramidal sinuous AA element is investigated at three distinct operating frequencies (450 MHz, 950 MHz and 1450 MHz). In all cases, a scan range of $\theta_0 \in [0°, 45°]$, $\phi_0 \in [0°, 360°]$ is analysed, on a rectangular grid with 5° spacing between adjacent samples.

Figure 5.6 shows Γ_{act} at the three considered frequencies, with the loci of grating lobe incursion superimposed. The scan response complexity increases with frequency as a result of more grating lobes entering visible space, although

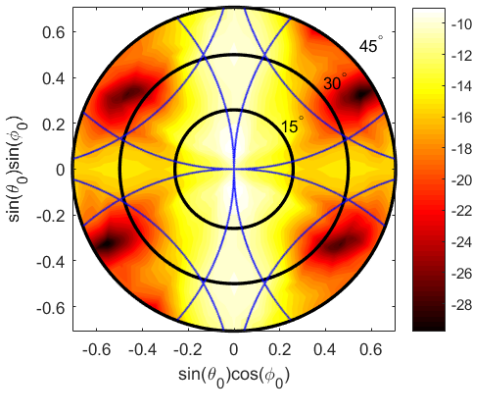

(a)

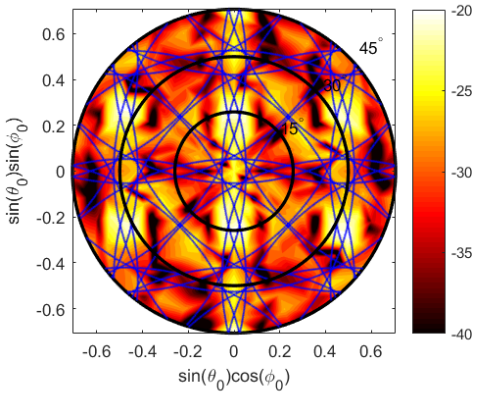

(b)

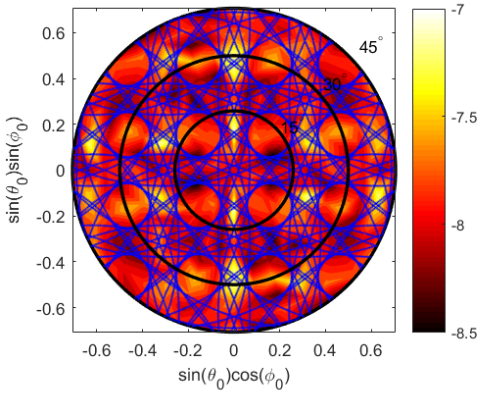

(c)

Figure 5.6: Pyramidal sinuous AA element $|\Gamma_{act}|$ at a) 450 MHz, b) 950 MHz, and c) 1450 MHz. Blue lines (—) mark the loci of grating lobe incursion.

it can be seen that Γ_{act} is not strongly perturbed by grating lobe incursion in comparison to the elements analysed in Chapter 3 and further indicates that the pyramidal sinuous element possesses stable enough impedance response behaviour to be seriously considered as a sparse-regular candidate element for MFAA.

Two key radiometric figures-of-merit are to be quantified. The first is the per-element receiving sensitivity $\frac{A_e}{T_{sys}}(\Omega_0, f)$, as defined in Chapter 2, which depends on Γ_{act}, the element radiation pattern and the impedance interaction between the antenna and the low-noise amplifier (LNA) at the first stage of the receiver chain. At present, the antenna feed and LNA are modelled ideally, with constant LNA noise parameters of $F_{min} = 0.4$ dB, $R_n = 10\ \Omega$ and $\Gamma_{opt} = 0.3$ across the frequency band. As with the initial design study of Chapter 2, the model proposed here is readily extensible to include more realistic feeding networks and LNA models, which can be simultaneously designed with the antenna element for an optimum practical receiver front-end.

Figure 5.7 shows the scan-dependent $\frac{A_e}{T_{sys}}$ at the three considered frequencies. The decrease in sensitivity with increasing frequency is expected for the sparse AA regime, where the effective area $A_e \approx \lambda^2/2$ [94]. Smooth variation of the sensitivity is observed at 450 MHz, with increasing nonlinear behaviour at the higher frequencies. At all frequencies, the sensitivity is seen to drop off with increasing θ_0 at the same rate that the isolated directivity patterns drop off with increasing θ.

The second figure-of-merit is the intrinsic cross-polarisation $\mathrm{IXR}(\Omega_0, f)$ [77]. Similar to [95], the Jones matrix required to calculate IXR is

$$J(\Omega_0, f) = \begin{bmatrix} E_{\Omega_0-\theta,1}(\Omega_0, f) & E_{\Omega_0-\phi,1}(\Omega_0, f) \\ E_{\Omega_0-\theta,2}(\Omega_0, f) & E_{\Omega_0-\phi,2}(\Omega_0, f) \end{bmatrix}, \tag{5.1}$$

where $E_{\Omega_0-\theta,k}$, $E_{\Omega_0-\phi,k}$ respectively denote the orthogonal θ- and ϕ-components of the unit cell electric far-field when the array is scanned to Ω_0.

The pyramidal sinuous AA element's IXR is shown at the three considered frequencies in Figure 5.7. At all three frequencies, abnormal variation occurs in multiple scanning regions with nulls forming close to zenith scan. It is thus evident that the IXR must be carefully considered and included in future optimisation of the element.

5.2 Impedance and Radiation Response Models

The modelling framework developed in Chapters 3 and 4 of this dissertation are now applied to estimating the impedance and radiation response behaviour of the MFAA sparse-regular pyramidal sinuous AA element. Given the rotational similarity of the responses shown in Figures 5.8 and 5.7, a parameter space of $\theta_0 \in [0°, 45°]$, $\phi_0 \in [0°, 180°]$, $f \in [450, 1450]$ MHz is selected. Γ_{act} at Port 1 is

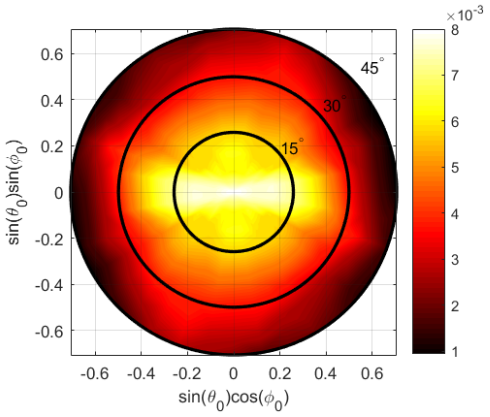

(a)

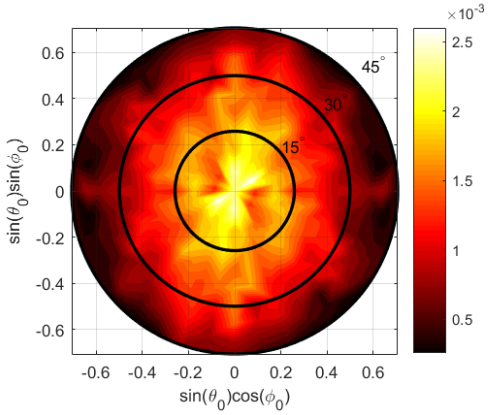

(b)

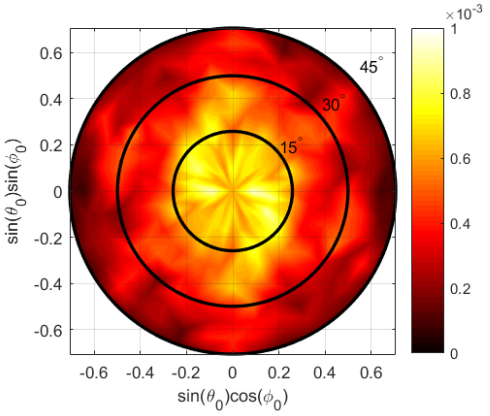

(c)

Figure 5.7: Pyramidal sinuous AA element $\frac{A_e}{T_{sys}}$ in (m^2/K) at a) 450 MHz, b) 950 MHz, and c) 1450 MHz.

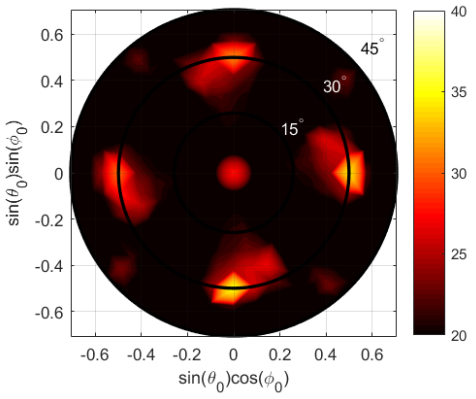

(a)

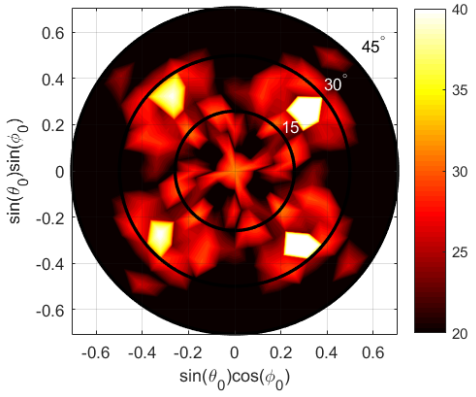

(b)

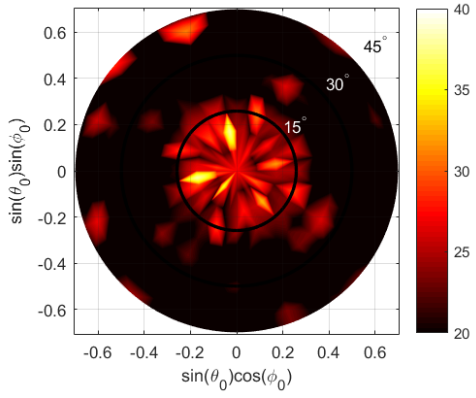

(c)

Figure 5.8: Pyramidal sinuous AA element IXR in dB, at a) 450 MHz, b) 950 MHz, and c) 1450 MHz.

used to drive the LOLA-Voronoi adaptive sampler, which is initiated with a 69-point latin hypercube plus 106 points throughout frequency and scan angle where multiple grating lobes in the array factor simultaneously enter visible space (following the S_3 sampling scheme in Chapter 3).

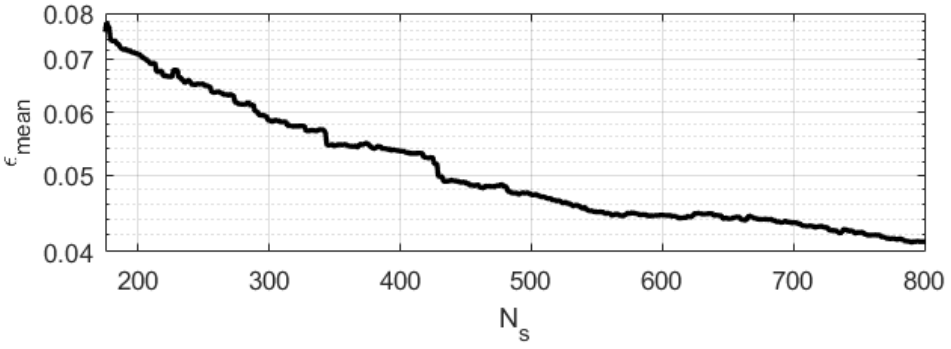

Figure 5.9: Pyramidal sinuous AA element ϵ_{mean} score for the Γ_{act} model.

The ϵ_{mean} score for the pyramidal sinuous AA element is plotted in Figure 5.9, showing a gradual decrease in the general impedance response modelling error as N_s increases. At $N_s = 800$, $\epsilon_{mean} = 4.12 \times 10^{-2}$; this is a somewhat larger general model error than the other Γ_{act} modelling examples explored in Chapter 3, which can be expected for a broadband AA element with a higher possibility of Γ_{act} scan variation due to mutual coupling between the physically large elements.

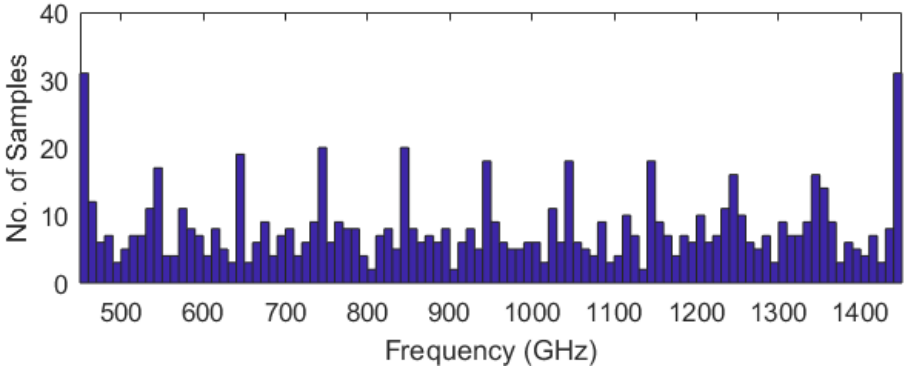

Figure 5.10: Histogram of validation point distribution for the pyramidal sinuous AA element model, at $N_s = 800$.

Figure 5.10 plots the distribution of validation points across frequency for $N_s = 800$, showing that the sample distribution is mostly evenly placed (note that the regular bars of high sample density arise from the points of grating lobe incursion chosen in the initial design). Given the increasing response complexity with frequency observed in Figure 5.6, more samples should be

assigned as frequencies increases. If a maximum number of sample points is selected before model construction commences, it may be effective to split the design space into multiple frequency regions and assign more samples to high-frequency regions.

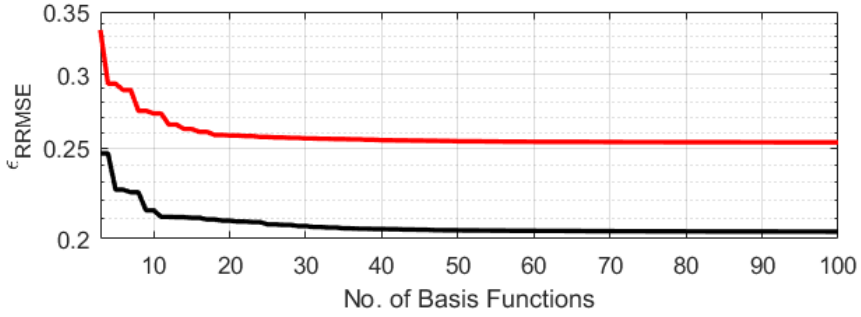

Figure 5.11: Pyramidal sinuous AA element far-field ϵ_{RRMSE}, at $N_s = 800$: — CBFP E_θ, — CBFP E_ϕ.

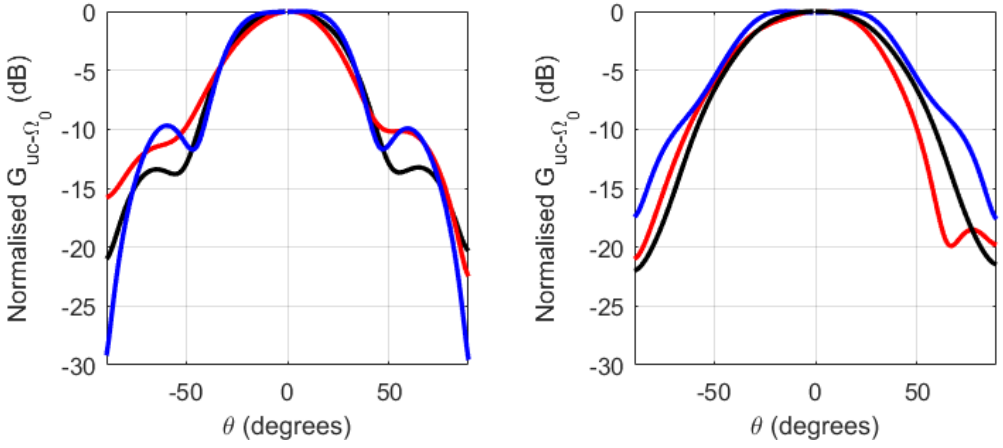

Figure 5.12: Pyramidal sinuous AA element normalised $G_{uc-\Omega_0}$ at $f = 950$ MHz and stimulated at Port 1, for a) $\phi = 0°$, and b) $\phi = 90°$. For both plots: — $\Omega_0 = (0°, \phi)$, — $\Omega_0 = (22.5°, 90°)$, and — $\Omega_0 = (45°, 90°)$.

Figure 4.18 shows the CBFP ϵ_{RRMSE} for both field components of $\overrightarrow{E}_{uc-\Omega_0}$, considered at $N_s = 800$. The ϵ_{RRMSE} scores converge around 30 basis functions per field component, yet they are significantly higher than the converged modelling errors found for the sparse-regular AA elements analysed in Chapter 3, suggesting a greater and more rapid scan variation in $\overrightarrow{E}_{uc-\Omega_0}$ for this particular element. Figure 5.12 shows the normalised $G_{uc-\Omega_0}$ at $f = 950$ MHz for a set of differing scan angles, demonstrating how the far-field changes as

the array is scanned away from zenith. It is clear that more high-fidelity samples are required to accurately reconstruct the far-fields across the parameter space.

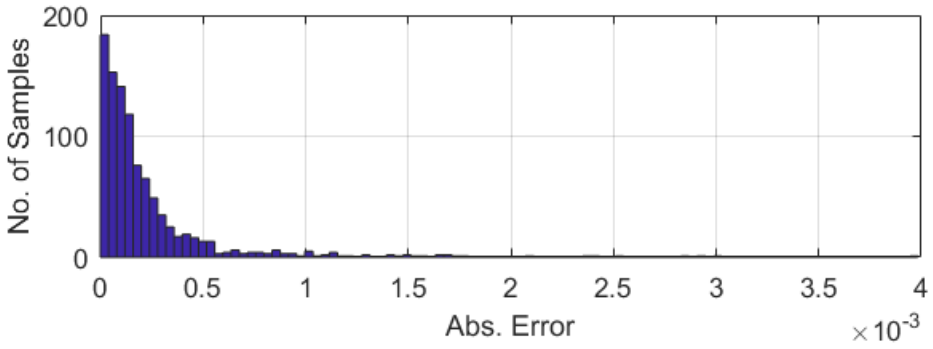

(a)

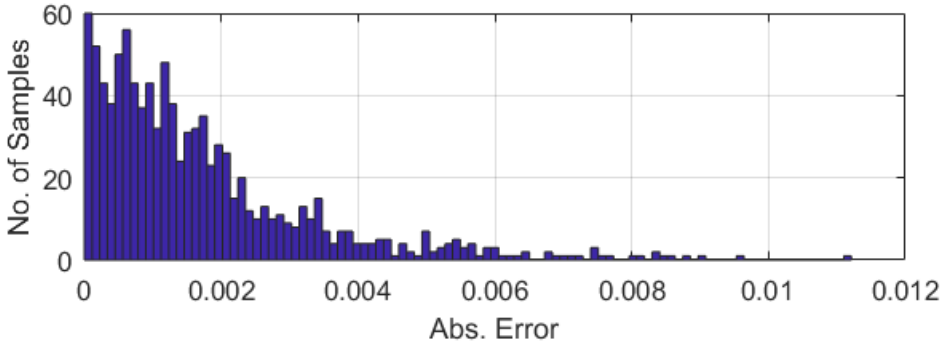

(b)

Figure 5.13: Histogram of the pyramidal sinuous AA element absolute model errors, at $N_s = 800$: a) $\frac{A_e}{T_{sys}}$, b) $\frac{G_{uc-\Omega_0}}{T_{sys}}$.

With global models for the impedance and radiation responses available, an estimate of the receiving sensitivity across the entire parameter space can now be acquired. Figure 5.13a shows a histogram of the absolute difference error between the validation $\frac{A_e}{T_{sys}}$ and the $\frac{A_e}{T_{sys}}$ obtained with the global Γ_{act} and $\overrightarrow{E}_{uc-\Omega_0}$ models, showing that the vast majority of errors lie below 0.5×10^{-3} m^2/K, with a few larger errors appearing as outliers. Indeed, the mean absolute error across the validation set is 2.28×10^{-4} — it is difficult to interpret this error score, however, given that receiving sensitivity naturally decreases with increasing frequency, making the error seem small in comparison with the zenith sensitivity at the lower frequencies yet unacceptably high in the upper frequency band. To better assess the modelling error, a histogram of the absolute difference modelling error of the $\frac{G_{uc-\Omega_0}}{T_{sys}}$ is also plotted in 5.13b, which is the receiving sensitivity with the λ^2 factor negated. Most response errors fall below $2{\times}10^{-3}$, with a mean absolute error of $1.7{\times}10^{-3}$; this constitutes roughly

10% error when compared to the zenith-scan validation $\frac{G_{uc-\Omega_0}}{T_{sys}}$ of 1.8×10^{-2} at $f = 450$ MHz and 1.46×10^{-2} at $f = 1450$ MHz.

Although the global surrogate model does provide a full view of the responses across the entire scan and frequency range with a degree of accuracy that steadily improves as more high-fidelity samples are added, this analysis illustrates the inherent modelling difficulty of broadband sparse-regular AA elements. Even with a high number of samples, the construction of a global surrogate model is challenged by the highly nonlinear nature of the response caused by the sparse-regular array environment. The geometry of the pyramidal sinuous element also requires a larger scanning space to be modelled than the axially symmetric dipoles and BLU element of Chapters 3 and 4 (although this is somewhat counteracted by the choice of a smaller range of θ_0), which unavoidably comes with higher modelling complexity.

5.3 Fast Sensitivity Performance Models

The framework proposed in this dissertation provides efficient estimates of the fundamental impedance and radiations responses of AA unit cell elements, with a level of accuracy that is reliably controlled by the number of high-fidelity samples used. While this is effective for general modelling purposes such as the analysis of a single design, the computational expense may be too high for design and optimisation where many element geometries are iteratively evaluated to find an optimal element.

Considering that the pyramidal sinuous MFAA element (or indeed, any sparse-regular candidate element for MFAA) must still be optimised to meet all system requirements, the evaluation of the element responses are now approached from an optimisation driven viewpoint to assess overall performance with even fewer high-fidelity samples than are typically invested into the general modelling framework. This section proposes a method to rapidly estimate the overall sensitivity performance of a sparse-regular AA element over frequency and scan angle, and applies this method to the pyramidal sinuous AA element.

5.3.0.1 Objective Function Design

For design objectives involving the maximisation of receiving sensitivity across frequency and scan angle, an intuitive objective function (to be maximised) can be formulated as

$$U_1 = \min_{\Omega_0, f} \left(\frac{\frac{A_e}{T_{sys}}(\Omega_0, f)}{\cos(\theta_0)} \right), \tag{5.2}$$

with the $\cos(\theta_0)$ factor applied to negate the angular foreshortening of the unit cell aperture. This formulation does not, however, take into account the smoothness of the sensitivity as the operating parameters are varied, which is a generally desirable quality in AAs and eases calibration and imaging procedures [94]. The response smoothness is assessed by fitting a 3$^{\text{rd}}$-order polynomial curve to a discrete set of (simulated or modelled) sensitivity response points, and finding the curve's coefficient of determination R^2 against the response points. The real coefficient $R^2 \in [0, 1]$, where higher values indicate a better fit of the sensitivity response points to the smooth polynomial curve (and therefore a desirably smooth sensitivity response).

With R^2 used to penalise U_1, an augmented objective function to be maximised during optimisation is formulated as

$$U_2 = U_1 R^2. \tag{5.3}$$

The augmented function of (5.3) now takes U_1 as a base score and penalises it by the smoothness of the response surface, represented by R^2. This fitting method is similar to the design of $U_{f,2}$ in Chapter 2's initial design study, although U_2 operates over the full scan and frequency range of the AA element and penalises the base objective score with the general sensitivity smoothness rather than by the worst deviation below the polynomial curve.

If desired, stricter penalisation for low R^2 scores may be implemented with additional terms such as barrier functions [96]. A suggested formulation is

$$U_3 = \frac{U_1}{\pi} B(R^2), \tag{5.4}$$

where

$$B(x) = \arctan\left(C_1 \pi (x - C_2)\right). \tag{5.5}$$

The modified arctangent term $B(R^2)$ strongly penalises sensitivity response surfaces exhibiting $R^2 < C_2$, where C_1 and C_2 are constants. The constant C_1 controls the steepness of the arctangent function and thereby how sharply the barrier function transitions from 0 (response completely rejected) to 1 (response completely unpenalised). Figure 5.14 shows examples of U_3 to illustrate the effect of choosing different sets of constants.

The U_1 and R^2 terms now form two scalar measures of the per-element receiving sensitivity response, quantifying the suitability of the element for use in an AA system; namely, the worst-case (minimum) sensitivity and the overall smoothness of the sensitivity over scan angle and frequency.

In the remainder of this section, a set of numerical examples are conducted in which global surrogate models of the per-element receiving sensitivity are built, with the intent of attaining accurate estimates of the U_1 and R^2 response features. The aim of focusing on accurate U_1 and R^2 estimation rather than

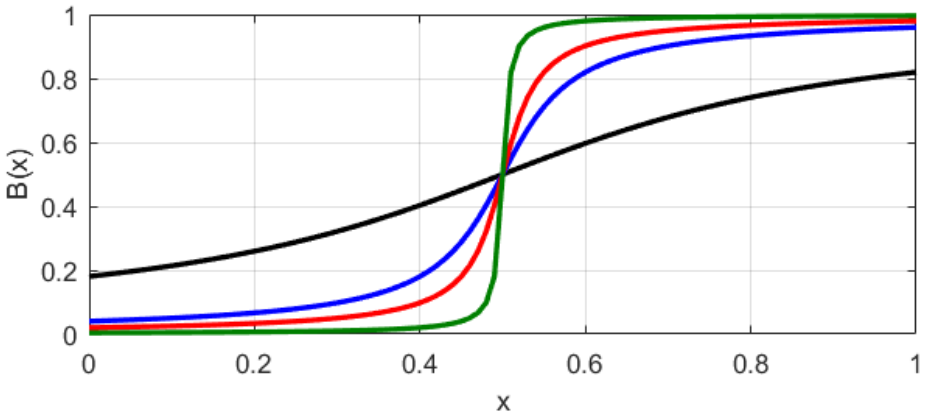

Figure 5.14: Modified arctangent barrier functions with $C_2 = 0.5$ and $C_1 = 1$ (—), $C_1 = 5$ (—), $C_1 = 10$ (—) and $C_1 = 50$ (—).

having an accurate general model of the receiving sensitivity is that it may require significantly fewer high-fidelity samples for the former, while still characterising the sensitivity performance sufficiently for design and optimisation purposes.

5.3.1 Narrowband Sensitivity Modelling

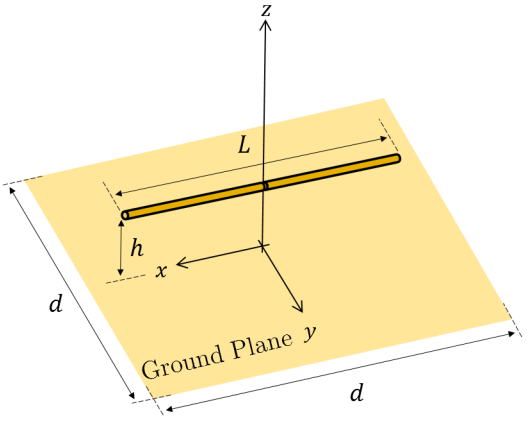

Figure 5.15: Dipole antenna element in a sparse-regular AA unit cell.

Before attempting the proposed performance modelling technique on a broadband element, two narrowband examples are considered over a two-dimensional parameter space $\theta_0 \in [0°, 85°]$, $\phi_0 \in [0°, 90°]$. Both examples consider a dipole element above a PEC ground plane in a sparse-regular AA unit cell, as depicted by Figure 5.15; the first example is a half-wave dipole with $L = 0.475\lambda$ and $d = 0.85\lambda$, while the second example is a long dipole with $L = \frac{3\lambda}{2}$ and $d = 1.5\lambda$. The second example, in particular, resembles a

sparse-regular AA element operating at its higher frequency range in a scenario where a large portion of the unit cell is spanned by the antenna geometry, such as for the sparse-regular MFAA elements considered in this chapter.

For both of the examples that follow, two global surrogate models are constructed which are labelled Model 1 and Model 2 respectively. These are adaptively sampled LOLA-Voronoi models, where Model 1's initial design is an N_i-point latin hypercube while Model 2's is an N_i-point combination of a latin hypercube and a set of points sampled at the grating lobe incursion points (similar to the S_3 sampling scheme in Chapter 3).

For Models 1 and 2, the LOLA-Voronoi algorithm selects new samples based on a Kriging model constructed on the $\frac{A_e}{T_{sys}}$ response; Ordinary Kriging with the Matérn $(\frac{3}{2})$ correlation function is chosen as the model type, while the Kriging hyperparameters are set by maximum likelihood estimation and iteratively adjusted to minimise the 5-fold cross-validation of the model's root relative mean-squared error (RRMSE). For the determination of the R^2 error as a function of N_s, each of the models are built 5 times and averaged to reduce the random nature of the latin hypercube distributions.

The models are validated in both examples on a regular 31×31 grid spanning the scanning space. While the receiving sensitivity is the radiometric response of interest, the aim of these experiments are not to assess the modelling accuracy of the modelled $\frac{A_e}{T_{sys}}$ response surface, but rather the accuracy of the R^2 response features based on $\frac{A_e}{T_{sys}}$. It is re-emphasised here that this is done in the interest of computational efficiency — from the models built in Section 5.2, it is apparent that many high-fidelity samples are required to obtain a model with a low sensitivity model error. By building a model for which the accuracy of pertinent response features (such as response surface smoothness) are of primary interest, significantly fewer high-fidelity samples may be required to provide sufficient information with which the overall performance of the antenna element can be quantified.

Although it is not straightforward to determine what range of errors between the modelled and validation R^2 might be considered acceptably low, a nominal target error value of 10^{-2} is chosen for the narrowband examples. Surfaces whose R^2 scores differ on the order of 10^{-2} are not considerably different in terms of smoothness, and is not likely to shift an objective function score between regions of low and high penalty if the U_3 objective is utilised.

5.3.1.1 Half-wave Dipole Element

Figure 5.16 shows the validation surfaces of $|\Gamma_{act}|$ and the normalised $G_{uc-\Omega_0}(\Omega_0)$, illustrating how the two responses perform across the scanning space and influence $\frac{A_e}{T_{sys}}$. It is clear that the highest sensitivity occurs only where the antenna element is both well matched and exhibits peak gain in the scan direction Ω_0. Discontinuities occur in the same scan locations for $\frac{A_e}{T_{sys}}$ as

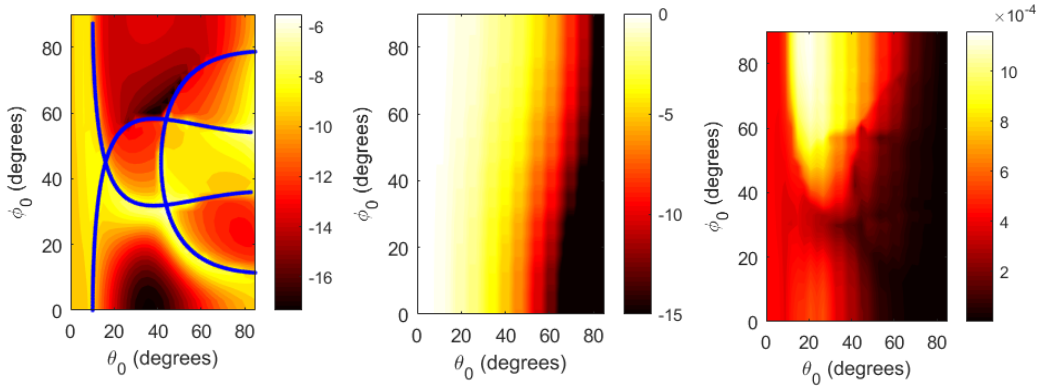

(a) (b) (c)

Figure 5.16: Validation response surfaces for the half-wave dipole AA unit cell: a) $|\Gamma_{act}|$ with grating lobe incursion loci superimposed (—), b) normalised $G_{uc-\Omega_0}(\Omega_0)$, and c) $\frac{A_e}{T_{sys}}$.

they do for Γ_{act}, albeit with less sharp variation. For the validation set, $U_1 = 1.704 \times 10^{-7}$ at $\Omega_0 = (85°, 0°)$ and $R^2 = 0.903$. Given that the minimum sensitivity occurs at a corner of the scanning space, which is always sampled by the latin hypercube's corner points, the U_1 response feature will have zero error for both models and is thus not considered here.

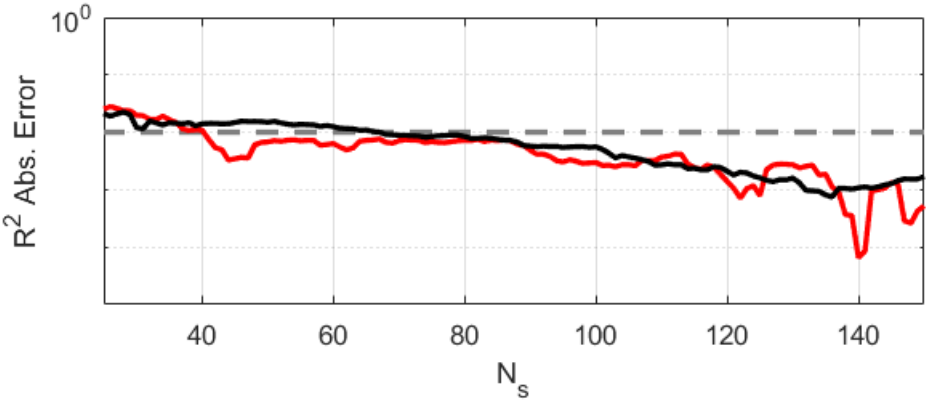

Figure 5.17: R^2 of the sensitivity response for the half-wave dipole AA unit cell, with - - - 10^{-2} target score, — Model 1, and — Model 2.

Figure 5.17 shows the averaged absolute error between the modelled and validation R^2 scores for the three models. The general behaviour of both models are quite similar with a general convergent trend towards lower error values, although Model 2 reaches the target score of 10^{-2} with 41 samples while Model 1 requires 67 samples to do the same. In both cases, the number of high-fidelity samples required to reach the target score is reasonably low.

5.3.1.2 Long Dipole Element

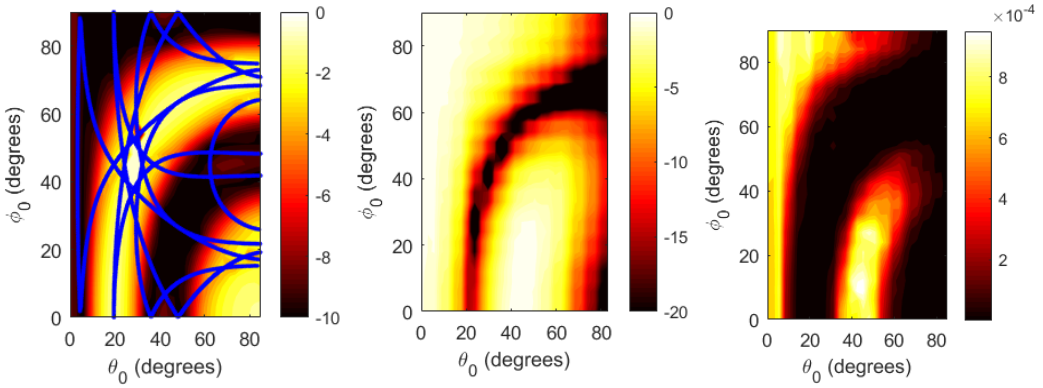

(a) (b) (c)

Figure 5.18: Validation response surfaces for the long dipole AA unit cell: a) Γ_{act} with grating lobe incursion loci superimposed (—), b) normalised $G_{uc-\Omega_0}(\Omega_0)$, and b) $\frac{A_e}{T_{sys}}$.

Figure 5.18 shows the validation surfaces of $|\Gamma_{act}|$ and the normalised $G_{uc-\Omega_0}(\Omega_0)$, as well as $\frac{A_e}{T_{sys}}$. An interesting feature of $|\Gamma_{act}|$ here is that, compared to the second dipole example of Chapter 3, the degradation of Γ_{act} is more broadly spread around the intersection of the grating lobe loci, based on the heightened mutual coupling between long dipole elements. The $\frac{A_e}{T_{sys}}$ response surface is decidedly less smooth than that of the half-wave dipole, bearing a broad null region close to zenith scan. For the validation set, $U_1 = 1.704 \times 10^{-7}$ at $\Omega_0 = (28.3°, 42°)$ and $R^2 = 0.537$, reflecting the non-smooth variation of the sensitivity as the AA is scanned away from zenith.

The absolute error between the validation and modelled U_1 scores is 1.577×10^{-7} for Model 1 and 1.536×10^{-7} for Model 2, both of which are attained with the initial design set and do not change as N_s increases. The two models' ability to predict the U_1 response minimum are therefore nearly identical for this example.

Figure 5.19 shows the absolute error between the modelled and validation R^2 scores for the two models. In this case, Model 2 requires 92 samples to converge below the target R^2 score and consistently decreases thereafter, while Model 1's absolute error wavers around 10^{-2} without converging below the target score. It can thus be seen that Model 2 outperforms Model 1 to approximate the validation R^2 with a minimal set of high-fidelity samples.

5.3.2 Broadband Sensitivity Modelling

The full-wave simulation of responses for ultrawideband AA elements is most often a computationally expensive task to be performed over a

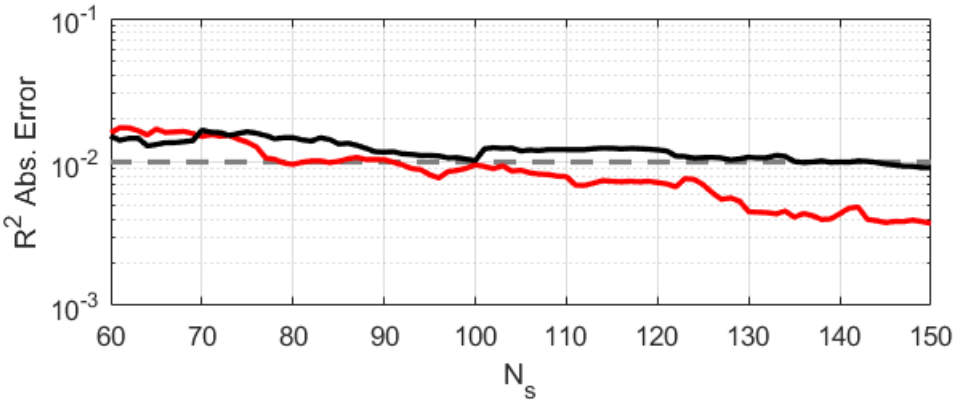

Figure 5.19: R^2 of the sensitivity response for the long dipole AA unit cell, with - - - 10^{-2} target score, — Model 1, and — Model 2.

three-dimensional operating parameter space (θ_0, ϕ_0, f). For an iterative optimisation of the antenna geometry or material parameters, it is desirable to accurately and efficiently assess a given element design's performance for one or multiple design criteria, which may be succinctly described by a suitable objective function.

5.3.2.1 Surrogate Model

The aim of the global surrogate model here is to attain an accurate estimate of the minima and overall smoothness of $\frac{A_e}{T_{sys}}$ over scan angle and frequency, with a minimal number of high-fidelity EM simulations used as sample points. The same modelling techniques used for the narrowband examples are applied here — it is expected that the method will be significantly more challenged by a full three-dimensional parameter space where the array environment grows extremely sparse with increasing frequency.

Three different modelling strategies are to be compared, leading to the construction of three separate global models. The first two models follow exactly the same principle as with the narrowband dipole models — the first initial design (Model 1) is a 175-point latin hypercube, while Model 2's initial design is composed of a 69-point latin hypercube plus 106 points throughout frequency and scan angle where multiple grating lobes in the array factor simultaneously enter visible space (following the S_3 sampling scheme in Chapter 3). Model 2 biases the global model construction towards points where rapid response variation may occur — the aim of this comparison is to assess which initial design provides a more accurate estimate of the response smoothness through the R^2 score.

Model 3 uses the same sampling scheme as Model 2, but instead of driving the LOLA-Voronoi adaptive sampler with $\frac{A_e}{T_{sys}}$, the $\frac{G_{uc-\Omega_0}}{T_{sys}}$ response surface is used instead. This is done because of the f^{-2} profile present in the definition

Table 5.4: R^2 scores for validation set and global models built with 350 samples.

f (MHz)	R^2			
	Validation	Model 1	Model 2	Model 3
450	0.94	0.99	0.97	0.84
950	0.88	0.99	0.87	0.84
1450	0.86	0.95	0.93	0.85

of A_e, which is expected to cause response variations at lower frequencies to vary with larger magnitude and effectively bias the adaptive sampler away from placing samples at higher frequencies. The choice of modelling on $\frac{G_{uc-\Omega_0}}{T_{sys}}$ rather than $\frac{A_e}{T_{sys}}$ negates the f^{-2} profile and aims to provide a more even response surface across frequency. However, it is also possible that for a sparse-regular array environment, this strategy will result in most samples clustering towards the higher frequencies, given that the response surface complexity increases with array sparseness (since more grating lobes enter visible space as the array becomes more sparse), which may lower the model accuracy at the lower frequencies.

5.3.2.2 Numerical Results

Across the validation set, $U_1 = 8.96 \times 10^{-5}$ at $\theta_0 = 45°$, $\phi_0 = 320°$, $f = 1450$ MHz, near several loci of GL incursion. The absolute error between this and the modelled U_1 scores is 6×10^{-5} for Model 1 and 7.45×10^{-6} for Models 2 and 3, all of which are attained with the initial design set and do not change as N_s increases. The superiority of Model 2 and Model 3's ability to predict the response minimum over Model 1 is evident.

Table 5.4 summarises the R^2 scores at three discrete frequencies, for validation sets built from the sampling set used in Section 5.1.3, as well as for Models 1, 2 and 3 built with 350 samples each. It can be seen that Model 2 more accurately predicts R^2 than Model 1 at all three frequencies, to a high degree of accuracy at 450 MHz and 950 MHz. Both models overestimate R^2 by more than 0.05 at 1450 MHz, suggesting that more uniform broadband model accuracy can be achieved with more samples allocated at the higher frequencies. Model 3, with more samples concentrated towards the higher frequencies, exhibits the lowest R^2 error at 1450 MHz, although it is seen to underestimate R^2 at 450 MHz and 950 MHz. This is in contrast with Models 1 and 2, which tend to overestimate R^2 where they are the least accurate. In general, Model 3's underestimation would yield a more conservative objective score than the high-fidelity response surface, which would be better for optimisation tasks than overestimating and returning a falsely optimistic objective score.

Figure 5.21 shows the absolute error between the validation and modelled

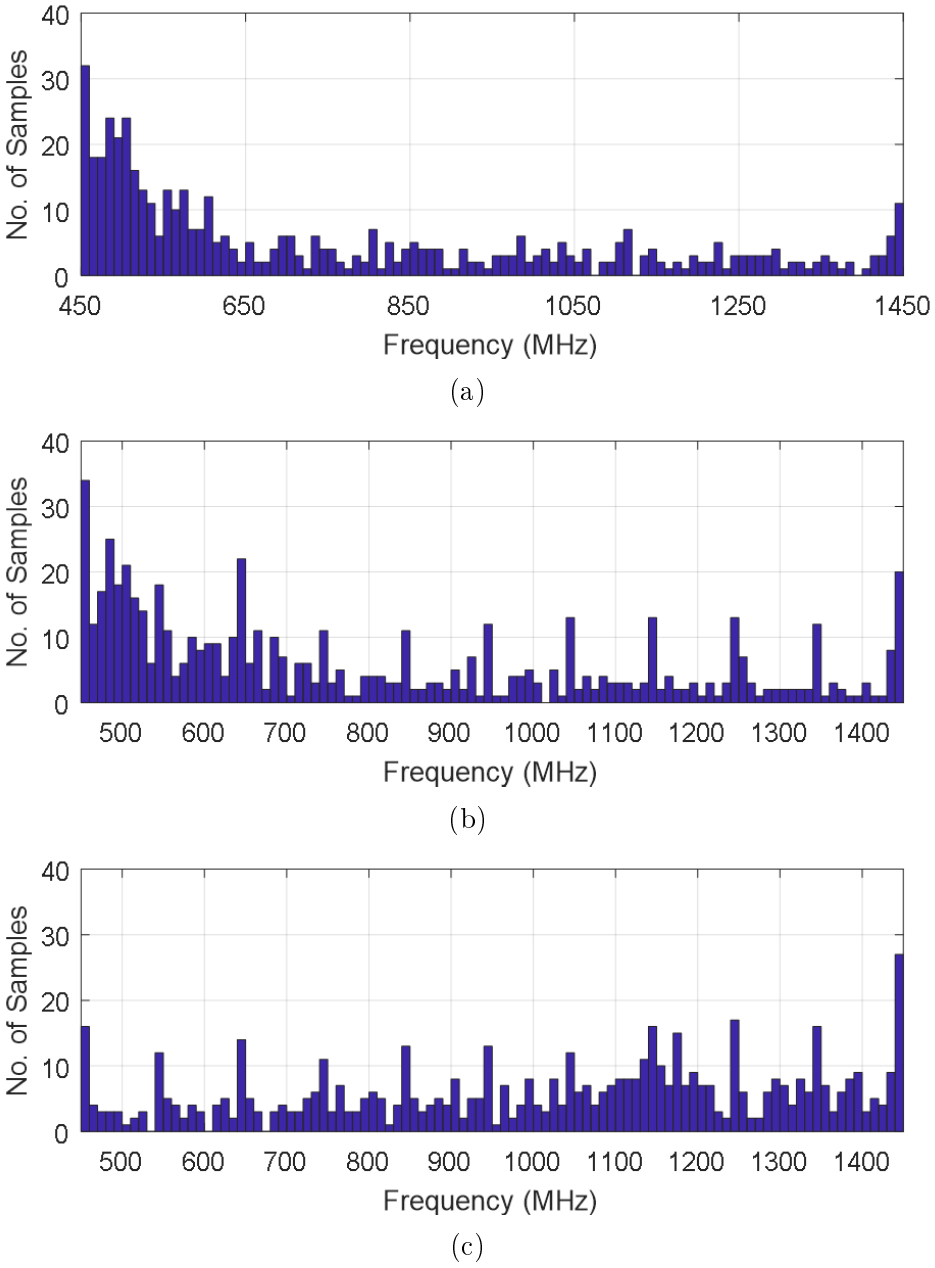

Figure 5.20: Histograms of sample allocation across frequency: a) Model 1, b) Model 2, and c) Model 3.

R^2 as a function of the number of samples used to build Models 1, 2 and 3. At 450 MHz and 950 MHz, Model 2 exhibits consistently lower error than Model 1. At 1450 MHz, however, it is clear that neither model has consistently improved beyond the initial prediction at 175 samples, further indicating that a larger number of samples should be focused towards the higher frequencies where the sensitivity is less smooth. Greater sampling density at the higher frequencies is achieved by Model 3, which has significantly lower R^2 error than

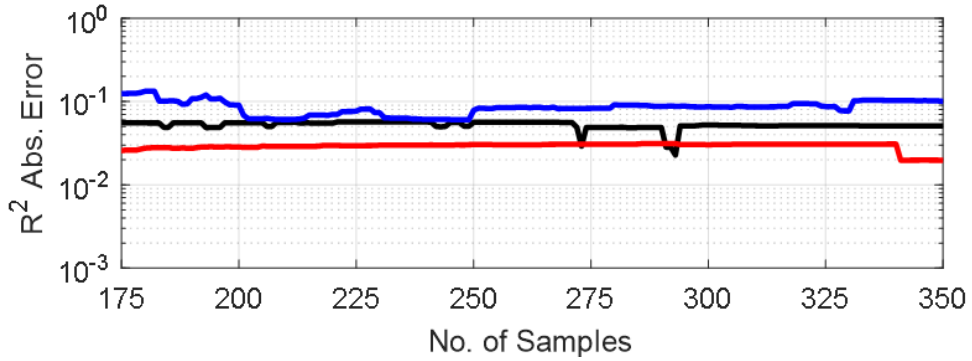

(a)

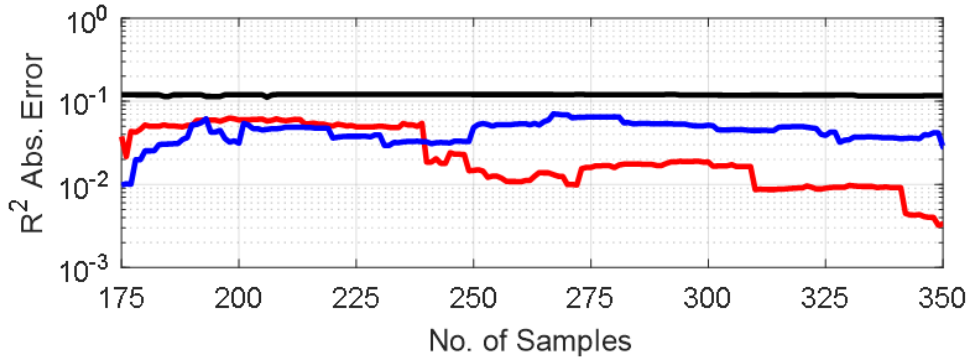

(b)

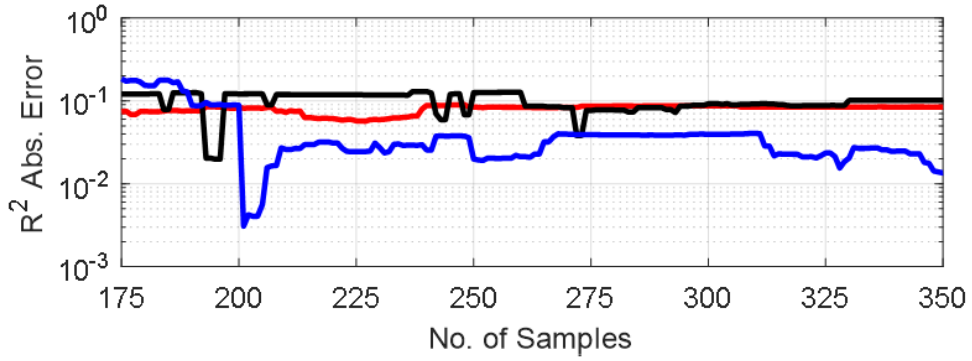

(c)

Figure 5.21: Absolute error between model and validation R^2 scores vs. number of model samples, at a) $f = 450$ MHz, b) $f = 950$ MHz , and c) $f = 1450$ MHz. For all plots, — Model 1, — Model 2, and — Model 3.

Models 1 and 2 at 1450 MHz, albeit at the cost of degraded accuracy for the lower frequencies.

It should be noted again that, in the sparse-regular array regime, sensitivity decreases with a f^{-2} profile, causing response variations at lower frequencies to vary with larger magnitude and effectively biasing the adaptive sampler away from placing samples at higher frequencies. This effect can be seen in Figure

5.20 for Models 1 and 2, where the majority of samples occur for $f < 600$ MHz. For Model 3, however, the highest concentration of samples is seen to occur in the higher frequency range, confirming the expectation that the adaptive sampler is drawn towards placing more samples where the $\frac{G_{uc-\Omega_0}}{T_{sys}}$ response surface is most nonlinear — that is, at frequencies where the most grating lobes enter visible space.

It can be seen from the results of this optimisation-driven modelling example that broadband model construction is, expectedly, more challenging than scan modelling at a single frequency. If an R^2 modelling accuracy of 10^{-2} is necessary, then it is clear that more high-fidelity samples are required to achieve acceptable accuracy across the entire MFAA frequency range. However, it is expected that even an R^2 error of 5×10^{-2} can provide a useful estimate of the sensitivity smoothness for optimisation purposes, which Models 2 and 3 are able to meet for two of the three observed frequencies. In this case, some hybridisation of the Model 2 and 3 sampling schemes may be useful to achieve a 5×10^{-2} R^2 model error across the whole frequency bandwidth. Additionally, splitting the parameter space into distinct frequency ranges and building separate models for each partition may help to avoid the clustering effects observed in Models 1, 2 and 3. Details such as the number of partitions to use, sample allocation per partition and the choice of sampling scheme in each partition should be carefully considered and developed, given the highly nonlinear nature of the sensitivity response surfaces prevalent in sparse-regular AAs.

5.4 Discussion of Results

It is important, at this point, to consider the development of the modelling techniques throughout this dissertation. In Chapter 2, it was shown that contemporary AA element designs are performed with response evaluation only at a few scan angles, or with high computational cost on a regular grid of scan angles — the former is not sufficient for the characterisation of sparse-regular AAs, while the latter is computationally exorbitant. Adaptively sampled global surrogate models developed in Chapters 3 and 4 have provided a means to evaluate the full scan- and frequency-dependent AA element responses with very few high-fidelity samples compared to conventional grid sampling, yet with high enough accuracy that the designer may assess the AA element's response performance with a reasonable degree of insight into the element's behaviour at more than just a few scan angles.

With the pyramidal sinuous AA element in this chapter, it has been shown that the modelling framework can be successfully applied to broadband designs in a highly sparse array environment, albeit with more high-fidelity samples than observed for the examples of Chapters 3 and 4. This is still favourable compared to response evaluation by regular grid sampling (in the case of the

pyramidal sinuous AA element, even a coarse grid with 5° scan resolution and 20 MHz frequency resolution constitutes 18870 high-fidelity samples) or pure latin hypercube sampling (due to the pre-sampling of grating lobe incursions as well as the use of LOLA-Voronoi), but nonetheless it would be advantageous in a full, iterative element optimisation procedure to reduce the model cost as much as possible. To this end, optimisation-driven sensitivity performance models have been developed and tested for narrowband and broadband AA elements.

Whereas the narrowband optimisation-driven models yield accurate results with few high-fidelity samples, the broadband case is naturally a more challenging problem over a higher-dimension parameter space, and with subtleties that only appear when broadband elements are analysed (such as the clustering of samples to either the lower or higher frequencies in the sparse-regular AA environment, when LOLA-Voronoi is trained either on $\frac{A_e}{T_{sys}}$ or $\frac{G_{uc-\Omega_0}}{T_{sys}}$). Even so, the broadband optimisation-driven models still provide a physics-based estimate of the complete AA element performance that has hitherto been unattainable with as few as 350 high-fidelity samples. While the response modelling framework of Chapters 3 and 4 is already considered to fulfil the requirements formulated in Chapter 2, the optimisation-driven approach provides a more efficient, alternate solution designed to be directly applied to AA element optimisation.

5.5 Conclusion

In this chapter, a pyramidal sinuous antenna element was proposed for a sparse-regular array, for the SKA Mid-Frequency Aperture Array, forming the primary contribution of this chapter. The element active reflection coefficient was shown to behave stably over a broad frequency and scanning range, and the element's scan-dependent radiometric figures-of-merit were analysed at discrete frequencies with a per-element modelling scheme in a PBC unit cell. It is clear from the scan analysis that this initial element design must be carefully designed and optimised for multiple design goals. Future work on the element includes the implementation of a full and efficient iterative optimisation, as well as the inclusion of components such as the antenna feeding structure and first-stage LNA.

A global surrogate model was constructed across the scan and frequency range of the pyramidal sinuous AA element, demonstrating the challenges of modelling a large, broadband AA element in a sparse-regular AA environment. As a step towards realising an optimisation procedure for sparse-regular AA antenna elements, a broadband global modelling procedure was outlined to rapidly estimate relevant response feature behaviour of the per-element receiving sensitivity, constituting the secondary contribution of this chapter. Accu-

rate estimates of the sensitivity minima and smoothness were obtained with a minimal set of full-wave EM simulations, with different response modelling methods considered in the broadband case. Ways to improve the uniformity of the model accuracy are of interest for future work, with a frequency-dependent trade-off of accuracy observed in the three broadband sensitivity models built for the pyramidal sinuous AA element.

Part of the work in this chapter was accepted for publication in the proceedings of the 2019 European Conference on Antennas and Propagation (EuCAP) [31].

Chapter 6

Conclusion

This dissertation presented a set of efficient techniques for modelling the multivariate responses of antenna elements in sparse-regular aperture arrays, addressing the particular challenges of the sparse-regular array regime and providing more comprehensive insight into the electrical behaviour of AA elements than is available with currently accepted design methods.

In terms of general AA element design and optimisation, global surrogate models were applied for the first time to the design of a BLU antenna element in the 100–450 MHz frequency range in an infinite array approximating the AA station environment, demonstrating the effectiveness of the surrogate modelling paradigm over parameter sweeps and brute-force optimisation. Through the design study performed to this end, it was also shown where current AA design methods analysing antenna responses at a discrete set of frequencies and scan angles may miss critical response features in a given antenna design, necessitating the development of more thorough techniques to analyse AA elements across scan angle and frequency in a computationally efficient manner.

To obtain efficient global response information over a multivariate range of operating parameters, a general modelling framework was developed by which the impedance and radiation responses are simultaneously modelled. Complications imposed by the incursion of grating lobes into visible space were addressed and a detailed pre-sampling scheme was developed from fundamental antenna array theory, requiring no *a priori* information of the electromagnetic behaviour of the AA element and increasing the model's ability to estimate the worst-case scan performance without sacrificing general modelling accuracy.

In terms of radiation responses, a formal comparison of two contemporary orthogonal basis function decomposition techniques was performed to be used in building efficient global response models of the AA element unit cell far-fields — as a result, the Characteristic Basis Function Pattern method was adopted into the modelling framework for the radiation response models.

Focusing on a relevant current design problem, antenna elements were considered for a sparse-regular AA for use in the SKA Mid-Frequency Aperture

Array. A pyramidal sinuous antenna element was proposed that was shown to exhibit notably stable impedance response behaviour over scan angle and frequency in the sparse-regular AA environment, leading to its consideration as a candidate AA element for further study and geometric optimisation. It was also shown through applying the global modelling framework that reasonably accurate results can be attained for the per-element receiving sensitivity, albeit with a large number of high-fidelity samples.

To accelerate the assessment of radiometric performance of broadband sparse-regular AA elements, an optimisation-driven, feature-based modelling technique was proposed that combined measures of the worst-case per-element sensitivity and overall sensitivity smoothness into a single objective function. In an application of the technique to the pyramidal sinuous AA element, it was found that driving the adaptive sampler with the receiving sensitivity biased the sample selection towards the lower frequencies; as a solution, an alternate model was built that trained the adaptive sampler on the ratio of the unit cell far-field gain to the element system temperature. The expectedly high level of nonlinearity in the higher frequency range (where many grating lobes enter visible space) focused most samples towards the high frequencies, providing excellent model accuracy of the smoothness score there at the detriment of model accuracy at the lower frequencies. Between the two model-building schemes, a trade-off of smoothness model accuracy was thus observed that should be carefully balanced in future work to obtain even estimates of the sensitivity smoothness score across frequency.

Across Chapters 3, 4 and 5, a modelling framework has been presented that analyses AA element response performance across a global space of scan angles and frequencies, with additional considerations for acceleration and use in element optimisation procedures. For each aspect of the framework, multiple options were implemented and compared for several design examples and the strengths as well as the limitations of each technique were presented to realistically evaluate the proposed methods as well as the general modelling problem of sparse-regular AA elements.

This dissertation presents several directions in which the work may be expanded and further researched:

- The modelling framework developed throughout this dissertation is directly applicable to a larger, iterative optimisation procedure — at each iteration, the optimiser varies the element geometry and requests an assessment of the current design's overall performance in the form of an objective function score, which must include information of the design across some required scanning and frequency range and is determined by invoking the modelling framework of this dissertation. In this sense, the modelling framework can be seen as the first step in realising a larger design and optimisation procedure for antenna elements in sparse-regular AAs.

- The pyramidal sinuous AA element, as presented in Chapter 5, requires further design and optimisation efforts to fully meet MFAA requirements. Given the previous point in this list, the pyramidal sinuous AA element presents itself as the ideal problem with which a full sparse-regular AA optimisation procedure can be tested.

- While this work focused on modelling antenna elements in an infinite array environment, the same general modelling framework is readily adaptable to smaller, finite antenna arrays. In this case, the scattering matrix and embedded element patterns would be modelled in place of the unit cell responses, and the response models reduce to one-dimensional interpolants across frequency. This strategy may be particularly useful for focal plane arrays in radio astronomy applications, although extensions of the work are required to incorporate array beamforming for focal plane arrays, which typically vary with amplitude and phase.

Bibliography

[1] M. Ryle and D. Vonberg, "Solar radiation on 175 Mc./s," *Nature*, vol. 158, no. 4010, pp. 339–340, Sep. 1946.

[2] "Astronomers to Mark 20th Anniversary of the Very Large Array," [Online], 2000, Available: https://www.nrao.edu/pr/2000/vla20/.

[3] "MeerKAT Radio Telescope," 2016. [Online]. Available: https://www.ska.ac.za/science-engineering/meerkat/

[4] K. F. Warnick, R. Maaskant, M. V. Ivashina, D. B. Davidson, and B. D. Jeffs, *Phased Arrays for Radio Astronomy, Remote Sensing and Satellite Communications*. UK: Cambridge University Press, 2018.

[5] J. bij de Vaate, A. J. Faulkner, and A. Gunst, "SKA AA concept descriptions," SKA Aperture Array Verification Program, Tech. Rep., 2011.

[6] P. E. Dewdney, P. J. Hall, R. T. Schilizzi, T. Joseph, and L. W. Lazio, "The Square Kilometre Array," *Proc. IEEE*, vol. 97, no. 8, pp. 1482–1496, Aug. 2009.

[7] M. de Vos, A. W. Gunst, and R. Nijboer, "The LOFAR telescope: System architecture and signal processing," *Proc. IEEE*, vol. 97, no. 8, pp. 1431–1437, Aug. 2009.

[8] C. J. Lonsdale, R. J. Cappallo, M. F. Morales, F. H. Briggs, L. Benkevitch, J. D. Bowman, J. D. Bunton, S. Burns, B. E. Corey, L. deSouza, S. S. Doeleman, M. Derome, A. Deshpande, M. R. Gopala, L. J. Greenhill, D. E. Herne, J. N. Hewitt, P. A. Kamini, J. C. Kasper, B. B. Kincaid, J. Kocz, E. Kowald, E. Kratzenberg, D. Kumar, M. J. Lynch, S. Madhavi, M. Matejek, D. A. Mitchell, E. Morgan, D. Oberoi, S. Ord, J. Pathikulangara, T. Prabu, A. E. E. Rogers, A. Roshi, J. E. Salah, R. J. Sault, N. U. Shankar, K. S. Srivani, J. Stevens, S. Tingay, A. Vaccarella, M. Waterson, R. B. Wayth, R. L. Webster, A. R. Whitney, A. Williams, and C. Williams, "The Murchison Widefield Array: The Square Kilometre Array precursor at low radio frequencies," *Proc. IEEE*, vol. 97, no. 8, pp. 1497–1506, Aug. 2009.

[9] "First SKA-Low Prototype Station Completed On Site," May 2018. [Online]. Available: https://www.skatelescope.org/news/first-ska-low-prototype-station-completed/

[10] J. G. bij de Vaate, S. A. Torchinsky, A. J. Faulkner, Y. Zhang, A. Gunst, P. Benthem, I. M. van Bemmel, and G. Kenfack, "SKA Mid Frequency Aperture Arrays: Technology for the ultimate survey machine," in *Proc. 31st URSI Gen. Assembly Sci. Symp.*, Beijing, China, Aug. 2014.

[11] A. van Ardenne, J. D. Bregman, W. A. Capellen, G. W. Kant, and J. G. bij de Vaate, "Extending the field of view with phased array techniques: Results of European SKA research," *Proc. IEEE*, vol. 97, no. 8, pp. 1531–1542, Aug. 2009.

[12] A. J. Faulkner, "Memo 122- the aperture arrays for the SKA," SKA, The SKADS White Paper, 2010.

[13] J. G. bij de Vaate and D. Kant, "The phased array approach to SKA, results of a demonstrator project," in *32nd European Microw. Conf.*, Milan, Italy, Sep. 2002.

[14] M. Ruiter and E. van der Wal, "EMBRACE, a 10,000 element next generation aperture array telescope," in *39th European Microw. Conf.*, Rome, Italy, Sep. 2009.

[15] R. P. Armstrong, J. Hickish, K. Z. Adami, and M. E. Jones, "Polarisation performance and calibration of the digital beamforming system for 2-PAD," in *IEEE Int. Symp. Phased Array Systems and Technology*, Waltham, USA, Oct. 2010.

[16] "Mid Frequency Aperture Array," 2016. [Online]. Available: https://www.skatelescope.org/mfaa/

[17] W. A. van Cappellen, M. Santos, J. P. Macquart, F. Abdalla, E. Petroff, A. Siemion, R. Taylor, O. Smirnov, D. B. Davidson, J. Broderick, J. van Leeuwen, P. Woudt, M. A. Garrett, A. J. Faulkner, S. A. Torchinsky, I. M. van Bemmel, and J. Hessels, "MANTIS: The Mid-Frequency Aperture Array Transient and Intensity-mapping System," AAMID Consortium, Tech. Rep., Dec. 2016.

[18] G. W. Kant, P. D. Partel, S. J. Wijnholds, M. Ruiter, and E. van der Wal, "EMBRACE: A multi-beam 20,000-element radio astronomical phased array antenna demonstrator," *IEEE Trans. Antennas Propag.*, vol. 59, no. 6, pp. 1990–2003, Jun. 2011.

[19] Y. Zhang and A. K. Brown, "Octagonal ring array for a compact dual-polarized aperture array," *IEEE Trans. Antennas Propag.*, vol. 59, no. 10, pp. 3927–3932, Oct. 2011.

[20] J. Gilmore and D. B. Davidson, "Progress on the development of a dual-polarized dense dipole array for the SKA Mid-Frequency Aperture Array," in *10th European Conf. Antennas Propag. (EuCAP)*, Davos, Switzerland, Apr. 2016.

[21] J. Abraham, E. Colin-Beltran, E. de Lara Acedo, and A. J. Faulkner, "A 16-element LPDA random sparse prototype array for the SKA AA-mid instrument," in *10th European Conf. Antennas Propag. (EuCAP)*, Davos, Switzerland, Apr. 2016.

[22] A. J. Faulkner, "Dense aperture arrays for the Square Kilometre Array," in *30th URSI Gen. Assbly. Scientific Symp.*, Istanbul, Turkey, Aug. 2011.

[23] C. A. Balanis, *Antenna Theory: Analysis and Design*, 3rd ed. New Jersey, USA: John Wiley and Sons, Inc., 2009.

[24] J. G. bij de Vaate, D. B. Davidson, and P. Benthem, "Expanding the field of view: Design considerations for a sparse-regular FFT SKA radio telescope," in *11th European Conf. Antennas Propag. (EuCAP)*, Paris, France, Mar. 2017.

[25] M. Tegmark and M. Zaldarriaga, "The Fast Fourier Transform Telescope," *Phys.Rev.D*, vol. 79, no. 8, May 2008.

[26] P. S. Kildal, *Foundations of Antenna Engineering: A Unified Approach for Line-of-Sight and Multipath.* Gothenburg, Sweden: Kildal Antenn AB, 2015.

[27] R. C. Hansen, *Phased Array Antennas*, 2nd ed. New Jersey, USA: John Wiley and Sons, Inc., 2009.

[28] B. Klopper and D. I. L. de Villiers, "Surrogate-based antenna element optimization for regularly spaced aperture arrays," in *Int. Conf. Electromagn. Advanced Applications (ICEAA)*, Sep. 2017.

[29] ——, "Efficient Impedance Response Modeling of Broadband Antenna Elements in Large Sparse-Regular Phased Arrays," *IEEE Trans. Antennas Propag.*, Sep. 2018, submitted.

[30] ——, "Efficient antenna scan response models for large phased arrays," in *Asia-Pacific Microwave Conference (APMC)*, Kyoto, Japan, Nov. 2019.

[31] ——, "Efficient performance modelling of a broadband sparse-regular aperture array antenna element," in *13th European Conf. Antennas Propag. (EuCAP)*, Krakow, Poland, March 2019.

[32] J. bij de Vaate, D. Davidson, and N. Razavi-Ghods, "Sparse-regular aperture array SKA telescope concept," in *Progress In Electromagnetics Research Symposium (PIERS)*, St. Petersburg, Russia, May 2017.

[33] S. Torchinsky, J. Broderick, A. Gunst, and A. Faulkner, "SKA-AAMID science requirements," Aperture Array MID Frequency Consortium, Tech. Rep., 2017.

[34] J. Gilmore, "Design of a dual-polarized dense dipole array for the SKA Mid-Frequency Aperture Array," Ph.D. dissertation, Stellenbosch University, Stellenbosch, South Africa, March 2016.

[35] E. de Lera Acedo, N. Razavi-Ghods, L. E. Garcia, P. Duffett-Smith, and P. Alexander, "Ultra-wideband aperture array element design for low frequency radio astronomy," *IEEE Trans. Antennas Propag.*, vol. 59, no. 6, pp. 1808–1816, Jun. 2011.

[36] Altair Hyperworks FEKO 2018. Altair Development - S.A. (Pty) Ltd, South Africa. [Online]. Available: http://www.feko.info

[37] G. Kant, A. Gunst, and M. Drost, "LOFAR High Band Antenna architectural design document," ASTRON, Tech. Rep., 2007.

[38] R. Lehmensiek, "Efficient adaptive sampling applied to multivariate, multiple output rational interpolation models, with applications in electromagnetics-based device modelling," Ph.D. dissertation, University of Stellenbosch, 2001.

[39] N. Nutonkole, "Modelling of antenna responses," Ph.D. dissertation, University of Stellenbosch, 2016.

[40] K. F. Warnick, R. Maaskant, M. V. Ivashina, D. B. Davidson, and B. D. Jeffs, "High-sensitivity phased array receivers for radio astronomy," *Proc. IEEE*, vol. 104, no. 3, Mar. 2016.

[41] A. K. Bhattacharyya, *Phased Array Antennas: Floquet Analysis, Synthesis, BFNs, and Active Array Systems.* New Jersey, USA: John Wiley and Sons, Inc., 2006.

[42] CST Microwave Studio 2018. Computer Simulation Technology. Darmstadt, Germany. [Online]. Available: www.cst.com

[43] C. Craeye, B. Parvais, and X. Dardenne, "MoM simulation of signal-to-noise patterns in infinite and finite receiving antenna arrays," *IEEE Trans. Antennas Propag.*, vol. 52, no. 12, pp. 3245–33 256, Dec. 2004.

[44] K. F. Warnick, M. V. Ivashina, R. Maaskant, and B. Woestenburg, "Unified definitions of efficiencies and system temperatures for receiving antenna arrays," *IEEE Trans. Antennas Propag.*, vol. 58, no. 5, pp. 2121–2125, Jun. 2011.

[45] K. F. Warnick and B. D. Jeffs, "Efficiencies and system temperature for a beamforming array," *IEEE Trans. Wireless Commun.*, vol. 7, pp. 565–568, Jun. 2008.

[46] K. F. Warnick, B. Woestenburg, L. Belostotski, and P. Russer, "Minimizing the noise penalty due to mutual coupling for a receiving array," *IEEE Trans. Antennas Propag.*, vol. 57, no. 6, pp. 1634–1644, Jun. 2009.

[47] M. V. Ivashina, R. Maaskant, and B. Woestenburg, "Equivalent system representation to model the beam sensitivity of receiving antenna arrays," *IEEE Antennas Wirel. Propag. Lett.*, vol. 7, pp. 733–737, Oct. 2008.

[48] R. Maaskant and E. E. M. Woestenburg, "Applying the active antenna impedance to achieve noise match in receiving array antennas," in *Proc. IEEE Antennas Propag. Soc. Symp.*, Honolulu, USA, Jun. 2007.

[49] D. M. Pozar, *Microwave Engineering*. New Jersey, USA: John Wiley and Sons, Inc., 2012.

[50] "Astronomy 534: Radiometers," 2016. [Online]. Available: http://www.cv.nrao.edu/course/astr534/Radiometers.html/

[51] B. D. Jeffs, K. F. Warnick, J. Landon, J. Waldron, D. Jones, J. R. Fisher, and R. D. Norrod, "Signal processing for phased array feeds in radio astronomical telescopes," *IEEE J. Sel. Top. Signal Process.*, vol. 2, no. 5, pp. 635–645, Oct. 2008.

[52] G. Cortes, "Antenna noise temperature calculations," SKA, SKA Memo 95, Jul. 2007.

[53] D. I. L. de Villiers and R. Lehmensiek, "Rapid calculation of antenna noise temperature in offset gregorian reflector systems," *IEEE Trans. Antennas Propag.*, vol. 63, no. 4, pp. 1564–1571, Apr. 2015.

[54] A. P. Chippendale, D. B. Hayman, and S. G. Hay, "Measuring noise temperatures of phased-array antennas for astronomy at CSIRO," *Publications of the Astronomical Society of Australia*, vol. 31, no. 19, Jan. 2014.

[55] M. B. Yelten, T. Zhu, S. Koziel, P. D. Franzon, and M. B. Steer, "Demystifying surrogate modeling for circuits and systems," *IEEE Circuits Syst. Mag.*, pp. 45–63, First quarter 2012.

[56] L. Lebensztajn, C. A. R. Marretto, M. C. Costa, and J. Coulomb, "Kriging: A useful tool for electromagnetic device optimization," *IEEE Trans. Magn.*, vol. 40, no. 2, pp. 1196–1199, Mar. 2004.

[57] D. G. Krige, "A statistical approach to some mine evaluations and allied problems at the Witwatersrand," Master's thesis, University of Witwatersrand, Johannesburg, South Africa, 1951.

[58] "DACE: A Matlab Kriging Toolbox," April 2011. [Online]. Available: http://www2.imm.dtu.dk/projects/dace/

[59] A. I. J. Forrester and A. J. Keane, "Recent advances in surrogate-based optimization," *Prog. Aerosp. Sci.*, vol. 45, 2009.

[60] C. E. Rasmussen and C. K. I. Williams, *Gaussian Processes for Machine Learning*. USA: MIT Press, 2006.

[61] MATLAB R2018a. The Mathworks Inc. Natick, MA. [Online]. Available: www.mathworks.com

[62] D. Gorissen, K. Crombecq, I. Couckuyt, T. Dhaene, and P. Demeester, "A surrogate modeling and adaptive sampling toolbox for computer based design," *Journal of Machine Learning Research*, vol. 11, pp. 2051–2055, July 2010.

[63] D. Gorissen, I. Couckuyt, E. Laermans, and T. Dhaene, "Multiobjective global surrogate modeling, dealing with the 5-percent problem," *Engineering with Computers*, vol. 26, no. 1, pp. 81–96, Feb. 2010.

[64] M. D. McKay, R. J. Beckman, and W. J. Conover, "A Comparison of Three Methods for Selecting Values of Input Variables in the Analysis of Output from a Computer Code," *Technometrics*, vol. 21, no. 2, pp. 239–245, May 1979.

[65] A. Forrester, A. Sobester, and A. Keane, *Engineering Design via Surrogate Modelling: A Practical Guide*. New Jersey, USA: John Wiley and Sons, Inc., 2008.

[66] A. A. Oliner and R. G. Malech, "Mutual coupling in infinite scanning arrays," in *Microwave Scanning Arrays*, R. C. Hansen, Ed. Academic, 1966, vol. II, ch. 3.

[67] C. Craeye and M. Arts, "On the receiving cross section of an antenna in infinite linear and planar arrays," *Radio Sci.*, vol. 39, no. 2, 2004.

[68] E. E. M. Woestenburg and L. Bakker, "Aperture Array Noise Temperature Measurements," ASTRON, Sep. 2011. [Online]. Available: http://www.astron.nl/dailyimage/index.html?main.php?date=20110920

[69] E. E. M. Woestenburg, L. Bakker, and M. V. Ivashina, "Experimental Results for the Sensitivity of a Low Noise Aperture Array Tile for the SKA," *IEEE Trans. Antennas Propag.*, vol. 60, no. 2, pp. 915–921, Feb. 2012.

[70] E. K. Miller, "Model-based parameter estimation in electromagnetics II: Applications to EM observables," *IEEE Antennas. Propag.*, vol. 40, no. 2, pp. 51–65, Apr. 1998.

[71] N. Mutonkole and D. I. L. de Villiers, "Adaptive frequency sampling for radiation patterns and S-parameters of antennas," in *11th European Conf. Antennas Propag. (EuCAP)*, Paris, France, Mar. 2017.

[72] S. Wang, L. Guo, X. D. Chen, C. G. Parini, and J. McCormick, "Fast calculation of wide angle ARC for broadband antenna arrays based on interpolation techniques," in *3rd Eur. Conf. Antennas Propag. (EuCAP)*, Berlin, Germany, Mar. 2009.

[73] K. Crombecq, D. Gorissen, L. de Tommasi, and T. Dhaene, "A novel sequential design strategy for global surrogate modeling," in *Proc. 2009 Winter Simulation Conference (WSC)*, Austin, USA, Dec. 2009.

[74] N. Mutonkole and D. I. L. de Villiers, "Multivariate adaptive sampling of parameterized antenna responses," *IEEE Trans. Antennas Propag.*, vol. 65, no. 3, pp. 1073–1080, Mar. 2017.

[75] S. Koziel and S. Ogurtsov, "Simulation-based design of microstrip linear antenna arrays using fast radiation response surrogates," *IEEE Antennas Wirel. Propag. Lett.*, vol. 14, pp. 759–762, Dec. 2015.

[76] N. Memarsadeghi, V. C. Raykar, R. Duraiswami, and D. M. Mount, "Efficient Kriging via fast matrix-vector products," in *IEEE Aerospace Conf.*, Big Sky, USA, Mar. 2008.

[77] T. D. Carozzi and G. Woan, "A Fundamental Figure of Merit for Radio Polarimeters," *IEEE Trans. Antennas Propag.*, vol. 59, no. 6, pp. 2058 – 2065, Jun. 2011.

[78] R. J. Allard and D. H. Werner, "The model-based parameter estimation of antenna radiation patterns using windowed interpolation and spherical harmonics," *IEEE Trans. Antennas Propag.*, vol. 51, no. 8, pp. 1891–1906, Aug. 2003.

[79] R. Burghelea, S. Avrillon, and B. Uguen, "UWB antenna compact modeling using vector spherical harmonic theory," in *IEEE Antennas Propag. Soc. Int. Symp.*, Charleston, USA, Jun. 2009.

[80] D. I. L. de Villiers, "A comparison of full pattern and response feature based modeling of antenna radiation patterns," in *Int. Conf. Electromagn. Advanced Applications (ICEAA)*, Verona, Italy, Sep. 2017.

[81] J. A. Stratton, *Electromagnetic Theory*. New York, USA: McGraw-Hill, 1941.

[82] J. E. Hansen, Ed., *Spherical Near-field Antenna Measurements*. London, UK: Institution of Engineering and Technology, 1988.

[83] GRASP version 10. TICRA, Copenhagen, Denmark. [Online]. Available: https://www.ticra.com/software/grasp/

[84] M. Abramowitz and I. A. Stegun, *Handbook of Mathematical Functions with Formulas, Graphs, and Mathematical Tables.* New York, USA: Dover, 1964.

[85] M. Arts, "Description of antenna patterns by vector spherical modes," ASTRON, Tech. Rep., 2018.

[86] R. Maaskant and M. Ivashina, "Characteristic basis function patterns - a novel expansion method for the fast and accurate prediction of antenna array beams," in *Int. Conf. Electromagn. Advanced Applications (ICEAA)*, Cape Town, South Africa, Sep. 2012.

[87] R. Maaskant, M. V. Ivashina, S. J. Wijnholds, and K. F. Warnick, "Efficient prediction of array element patterns using physics-based expansions and a single far-field measurement," *IEEE Trans. Antennas Propag.*, vol. 50, no. 8, pp. 3614–3621, Aug. 2012.

[88] A. Young, R. Maaskant, M. V. Ivashina, and D. B. Davidson, "Application of the characteristic basis function pattern method to reflector surface inaccuracies and sidelobe modeling," in *Int. Conf. Electromagn. Advanced Applications (ICEAA)*, Torino, Italy, Sep. 2013.

[89] A. Young, "Improving the Direction-Dependent Gain Calibration of Reflector Antenna Radio Telescopes," Ph.D. dissertation, Stellenbosch University, Stellenbosch, South Africa, December 2013.

[90] N. Mutonkole and D. I. L. de Villiers, "Characteristic basis function patterns method for reflector antenna calibration: An extension to multiple frequencies," in *9th European Conf. Antennas Propag. (EuCAP)*, Lisbon, Portugal, Apr. 2015.

[91] M. Ruiter, W. van Cappellen, E. van der Wal, M. Arts, R. van den Brink, and K. Visser, "Development of a Vivaldi tile for the SKA Mid Frequency Aperture Array," in *10th European Conf. Antennas Propag. (EuCAP)*, Davos, Switzerland, April 2016.

[92] E. de Lera Acedo, N. Razavi-Ghods, N. Troop, N. Drought, and A. Faulkner, "SKALA, a log-periodic array antenna for the SKA-low instrument: design, simulations, tests and system considerations," *Experimental Astronomy*, vol. 39, no. 3, pp. 567–594, Oct. 2015.

[93] N. Steenkamp, D. I. L. de Villiers, and N. Mutonkole, "Wideband pyramidal sinuous antenna for reflector antenna applications," in *11th European Conf. Antennas Propag. (EuCAP)*, Paris, France, Mar. 2017.

[94] R. Braun and W. van Capellen. (2006) Aperture Arrays for the SKA: Dense or Sparse? SKA Memo 87. [Online]. Available: www.skatelescope.org

[95] B. Fiorelli and E. de Lera Acedo, "On the simulation and validation of the Intrinsic Cross-Polarization Ratio for antenna arrays devoted to low frequency radio astronomy," in *8th Eur. Conf. Antennas Propag. (EuCAP)*, The Hague, The Netherlands, Apr. 2014.

[96] A. Arkko and J. Rahola, "On the optimization of mobile terminal antenna isolation using the genetic algorithm technique," in *2nd Eur. Conf. Antennas Propag. (EuCAP)*, Edinburgh, UK, Nov. 2007.